CHARACTERIZING THE STAR FORMING PROPERTIES OF HERSCHEL-DETECTED GRAVITATIONALLY LENSED GALAXIES

by

Gregory Lee Walth

(BY:)   (=)

A Dissertation Submitted to the Faculty of the

DEPARTMENT OF ASTRONOMY

In Partial Fulfillment of the Requirements
For the Degree of

DOCTOR OF PHILOSOPHY

In the Graduate College

THE UNIVERSITY OF ARIZONA

2015

THE UNIVERSITY OF ARIZONA
GRADUATE COLLEGE

As members of the Dissertation Committee, we certify that we have read the dissertation prepared by Gregory Lee Walth, entitled Characterizing the Star Forming Properties of Herschel-Detected Gravitationally Lensed Galaxies and recommend that it be accepted as fulfilling the dissertation requirement for the Degree of Doctor of Philosophy.

_____ Date: 23 September, 2015
Eiichi Egami

_____ Date: 23 September, 2015
George Rieke

_____ Date: 23 September, 2015
Xiaohui Fan

_____ Date: 23 September, 2015
Dennis Zaritsky

_____ Date: 23 September, 2015
Dan Marrone

Final approval and acceptance of this dissertation is contingent upon the candidate's submission of the final copies of the dissertation to the Graduate College.

I hereby certify that I have read this dissertation prepared under my direction and recommend that it be accepted as fulfilling the dissertation requirement.

_____ Date: 23 September, 2015
Dissertation Director: Eiichi Egami

_____ Date: 23 September, 2015
Dissertation Director: George Rieke

STATEMENT BY AUTHOR

This dissertation has been submitted in partial fulfillment of requirements for an advanced degree at the University of Arizona and is deposited in the University Library to be made available to borrowers under rules of the Library.

SIGNED: Gregory Lee Walth

ACKNOWLEDGEMENTS

DEDICATION

This thesis is dedicated to my family.

To my parents, Francine and Gary, who always believed in me and told me I could be whatever I wanted, if I was willing to work hard enough.

To my wife and son, Kristin and Ethan, whose love and support helped me through graduate school.

TABLE OF CONTENTS

TABLE OF CONTENTS – *Continued*

TABLE OF CONTENTS – *Continued*

LIST OF FIGURES

LIST OF FIGURES – *Continued*

LIST OF TABLES

ABSTRACT

Dusty star forming galaxies (DSFGs), characterized by their far-infrared (far-IR) emission, undergo the largest starbursts in the Universe, contributing to the majority of the cosmic star formation rate density at $z = 1 - 4$. The *Herschel* Space Observatory for the first time was able observe the full far-IR dust emission for a large population of high-redshift DSFGs, thereby accurately measuring their star formation rates. With gravitational lensing, we are able to surpass the *Herschel* confusion limit and probe intrinsically less luminous and therefore more normal star-forming galaxies. With this goal in mind, we have conducted a large *Herschel* survey, the *Herschel* Lensing Survey, of the cores of almost 600 massive galaxy clusters, where the effects of gravitational lensing are the strongest.

In this thesis, I present follow-up studies of gravitationally lensed *Herschel*-detected DSFGs by utilizing multi-wavelength data from optical to radio. Specifically, I characterize the star forming properties of gravitationally lensed DSFGs by using these three subsamples: (1) A gravitationally lensed DSFG galaxy at $z = 0.6$ in one of the most massive galaxy clusters, Abell S1063 (at $z = 0.3$), (2) One of the brightest sources in HLS, which is a system of two strongly gravitationally lensed galaxies, one at $z = 2.0$ (optically faint gravitational arc) and the other at $z = 4.7$ (triply-imaged galaxy), (3) A sample of the brightest sources in HLS at $z = 1 - 4$, in which we detect rest-frame optical nebular emission lines (e.g. Hα, Hβ, [OIII]$\lambda\lambda$4959,5007) by utilizing near-IR spectroscopy. The main results from these studies are as follows:

(1) In the cluster-lensed DSFG at $z = 0.6$, discovered in the core of Abell S1063, we identify a luminous (SFR = 10 M$_\odot$/yr) giant (D $\sim$ 1 kpc) HII region similar to those typically found at higher redshift ($z \sim 2$). We show that the HII region is embedded in a rotating disk and likely formed in isolation, rather than through

galaxy interaction, which is observed in local galaxies. We can use this source as a nearby laboratory for star forming regions at $z \sim 2$, in which more detailed follow-up of this source can help us to understand their origin/properties.

(2) We discovered that one of the brightest sources in HLS is a blend of two cluster-lensed DSFGs, one at $z = 2.0$ (an optically faint arc) and the other at $z = 4.7$ (triply-imaged galaxy), implying that a sample of bright *Herschel* sources may have such multiplicity. In the $z = 2.0$ arc, the sub-arcsecond clumps detected in the SMA image surprisingly do not correspond to the clumps in the JVLA CO(1-0) image. When investigating the CO(1-0) velocity structure, there is a substantial amount of molecular gas (likely a molecular wind/outflow) we find that we find is not associated with star formation. This suggests that the CO morphology in DSFGs could be strongly influenced by molecular outflows resulting in the over-prediction of the amount of the molecular gas available for star formation. In the $z = 2.0$ arc, we also constrain $\alpha_{CO} \sim 4$. While this value is normal for galaxies like the Milky Way, it is quite unusual for ULIRGs. This hints that the physical conditions may be much different in the arc from other ULIRGs, which usually have $\alpha_{CO} \approx 0.8$.

(3) We successfully detect rest-frame optical emission lines in 8 gravitationally lensed DSFGs at $z = 1 - 4$ using ground-based near-IR spectroscopy with Keck, LBT and Magellan. The luminosities of these lines are substantially less than what the far-IR derived star formation rates predict, suggesting that these DSFGs have large dust attenuations. The difference in the star formation rates is a factor of $30\times$ ($A_V = 4$), which is larger than previously reported for DSFGs at $z > 1$. One galaxy ($z = 1.5$) in the sample showed the largest suppression with a factor of $550\times$ ($A_V = 7$), which is similar to local ULIRGs.

Future prospects: *Herschel* provided a glimpse into the star formation of DSFGs, but only the brightest at $z > 2$ could be studied in detail without gravitational lensing. ALMA will revolutionize the study of DSFGs with its high spatial resolution submm/mm imaging of their dust continuum and molecular gas, and it will begin to unravel their physical properties. In order to detect nebular emission lines in fainter higher redshift sources, 20-30 meter class telescopes, with next generation near-IR

spectrographs, will be necessary. *JWST* will play a significant role as it will target rest-frame optical nebular emission lines in DSFGs unobtainable from the ground as well as weaker Hydrogen series lines (such as Paschen and Brackett series) to better understand their instantaneous star formation and dust attenuation.

CHAPTER 1

Introduction

1.1 Dusty, Star-Forming Galaxies

Dusty star forming galaxies contribute to the majority of star formation in the Universe, specifically at redshifts $z = 1 - 4$, in which luminous infrared galaxies (LIRGs) and ultra-luminous infrared galaxies (ULIRGs) contribute the most (Le Floc'h et al., 2005; Pérez-González et al., 2005; Caputi et al., 2007; Rodighiero et al., 2010b; Magnelli et al., 2011; Gruppioni et al., 2013). The majority of a dusty, star-forming galaxy's luminosity comes from its far-IR/submm emission. This emission comes from dust, which re-radiates the energy from young stars. Since there is so much dust in these galaxies, their rest-frame UV and optical are heavily obscured, and most of what we know about them comes from the far-IR/submm. Recent work has only been able to follow-up the most luminous and least dust obscured of these galaxies at high redshift ($z > 1$). In order to understand the conditions conducive to star formation in these galaxies, we must study their interstellar medium (ISM). We can develop a complete picture of star formation within these galaxies by investigating the following; molecular gas that fuels star formation, dust emission which are the sites of star formation, and nebular emission which is the gas that is excited by the young stars around them. By having the complete star formation picture we can better understand how these galaxies go through the largest episodes of star formation in the Universe.

1.2 Molecular Gas

In molecular clouds, molecular hydrogen gas or H_2 is thought to be the primary material for forming stars, which it forms in cold dense cores. Unfortunately, H_2 is difficult to detect, so it is necessary to use other tracers in order to determine

how much H_2 is in a given cloud. One such tracer is CO, which traces the H_2 gas and is much easier to detect. Other tracers also exist, such as HCN, HCO+, or CN, which are better tracers of the denser regions of the molecular clouds, but in turn are much more difficult to detect at high redshift. For high redshift galaxies, submm/mm facilities are more sensitive in detecting higher order CO transitions than radio facilities of the fainter CO(1-0) emission. With the newly upgraded JVLA, it is now feasible to detect CO(1-0) in high-redshift galaxies. Even CO(1-0) has some difficulties as it requires a conversion factor between the line luminosity and the gas mass, α_{CO}. It appears that α_{CO} is dependent on galaxy type: galaxies similar to the Milky Way have α_{CO} values similar to 4.0, and in galaxies with starbursts, mergers or ULIRGs, α_{CO} have a value of 0.8. In order to have more accurate measurement of gas mass, larger samples of galaxies at high redshift are needed to better constrain α_{CO}. When accounting for the redshift evolution of the star-forming main sequence (Noeske et al., 2007; Rodighiero et al., 2011; Whitaker et al., 2012), galaxies that might be considered starbursts in the local Universe may fall on the main sequence at higher redshift. Genzel et al. (2015) showed that galaxies on the star-forming main sequence have α_{CO} values of ~ 4. Galaxies with specfic star formation rates $4\times$ the star-forming main sequence are considered starbursts and typically have α_{CO} values ~ 0.8.

1.3 Nebular Emission

The rest-frame optical is least known in dusty, star-forming galaxies. With only the brightest sources detected, these observations may not represent typical dusty, star-forming galaxies. The rest-frame optical provides an abundance of information regarding a galaxy's metallicity (R23, N2, O3HB), ionization state ([OIII]/[OII]), instantaneous star formation rate (Hα, Hβ, and [OII]) and whether it contains an AGN. This is useful for comparing dusty, star-forming galaxies to more typical star forming galaxies, which could perhaps suggest evolutionary differences.

Targeting complete sets of nebular emission lines above redshift $z > 0.5$ is challenging. In the near-IR the sky background is much larger and OH emission lines are

much more abundant, increasing the difficulty in detecting nebular emission lines. In addition, there are a limited number of atmospheric windows available, limiting the redshifts of sources that are possible to target. With upgrades in detector technology and the ability to better multiplex spectra, near-IR multi-object spectroscopy is now obtainable for more "normal" star forming galaxies. However, dusty, star-forming galaxies still pose a challenge as their rest-frame optical emission is still heavily attenuated by dust, only making the least dusty galaxies accessible.

1.4 Dust and the *Herschel* Space Observatory

The *Herschel* Space Observatory opened up a new window for studying high redshift ($z > 1$) dusty, star-forming galaxies by sampling their far-IR/submm peak emission. *Herschel* for the first time was able to observe at wavelengths unobtainable from the ground and at sensitivities to detect large populations of dusty, star-forming galaxies at redshifts $z > 1$. By fully sampling the far-IR/submm peak, *Herschel* is able to accurately measure the star formation rates of dusty galaxies. However, *Herschel* reaches the confusion limit quickly, and no amount of integration will break through it. This means that *Herschel* can only detect the most luminous sources ($L_{IR} > 10^{12} \ L_{\odot}$) at redshifts $z > 2$. By utilizing massive galaxy clusters as powerful lenses, it is possible to surpass the confusion limit. With magnifications typically between 5-10$\times$, and even as high as 100$\times$, it is possible to probe dusty, star-forming galaxies at redshift $z > 2$ and down to lower luminosities. The *Herschel* Lensing Survey is a survey of 581 massive galaxy clusters with the goal of detecting gravitationally lensed dusty, star-forming galaxies, which we draw our sample from.

1.5 The Goal of this Thesis

The goal of this thesis is to investigate the star forming properties of gravitationally lensed dusty, star-forming galaxies. In achieving this we investigate the nebular emission, dust emission and the molecular gas, in order to develop a complete picture of star formation. In this thesis we explore the following questions:

In Chapter 2 we investigate the most massive cluster, Abell S1063, and characterize the properties of the brightest infrared sources detected in its core. Will we find highly magnified dusty, star-forming galaxies? With the high spatial resolution gained from gravitational lensing, can we connect the rest-frame UV and optical emission (from *HST* imaging) of star forming regions within dusty, star-forming galaxies to the their far-IR/submm emission?

In Chapter 3 we study the one of the brightest sources in HLS and investigate its far-IR/submm emission and it molecular gas reservoirs. What does high resolution submm imaging tell us about one of the brightest gravitationally lensed sources in HLS? By observing CO(1-0), can we accurately determine the gas mass and α_{CO}? Is α_{CO} consistent with other studies? By studying sub-kpc scales afforded by gravitational lensing, what does the resolved star formation tell us about the Kennicutt-Schmidt law?

In Chapter 4 we study the rest-frame optical emission properties of a sample of gravitationally lensed *Herschel* sources from HLS. Do the Hα derived star formation rates match the far-IR derived star formation rates for sample of *Herschel* selected galaxies? Do LIRGs at redshifts $z > 1$ have the same dust attenuations as ULIRGs? Or are they less dusty, as they are in the local Universe? What is the metallicity distribution of a sample of *Herschel* selected galaxies?

In Chapter 5 we present the conclusions of the thesis and future prospects of the field.

CHAPTER 2

Infrared Galaxies in the Field of the Massive Cluster Abell S1063: Discovery of a
Luminous Kiloparsec-Sized Giant HII Region
in a Gravitationally Lensed IR-Luminous Galaxy at $z = 0.6$ [†]

Using the *Spitzer* and *Herschel* Space Telescope/Observatory, we have conducted
a survey of infrared galaxies in the field of the massive galaxy cluster Abell S1063
(AS1063) at $z = 0.347$, one of the most massive clusters known and a target of
the *HST* CLASH and Frontier-Field surveys. The *Spitzer*/MIPS 24 μm and *Herschel*/PACS & SPIRE images revealed that the core of AS1063 is surprisingly devoid
of infrared sources, showing only a few detectable sources within the central r$\sim$1′
region. There is, however, one particularly bright source (2.3 mJy at 24 μm; 106
mJy at 160 μm), which corresponds to a background galaxy at $z = 0.61$ (AS1063a).
The modest magnification factor (3.7×) implies that this galaxy is intrinsically IR-
luminous and of the LIRG type ($L_{IR} = 3.3 \times 10^{11} L_{\odot}$). What is particularly interest-
ing about this galaxy is that its *HST* optical images show a remarkably bright and
large ($\sim$1 kpc) clump at one edge of the disk. Our follow-up optical/near-infrared
spectroscopy shows strong Balmer (Hα-H8) and forbidden emission lines from this
clump ([OII] λ3727, [OIII] $\lambda\lambda$4959,5007, [NII] $\lambda\lambda$6548,6583), indicating that it is

a giant HII region. The kinematics measured with our optical spectrum indicate that this giant HII region is part of the rotating disk. With an extinction correction of $A_\mathrm{v} = 1.2$ mag, the star formation rate (SFR) of this giant HII region is derived to be $\sim$10 M$_\odot$/yr, which is large but significantly less than the IR-derived SFR of $\sim 60 M_\odot$/yr for AS1063a. This suggests that the bulk of star formation in this galaxy is obscured by dust, which is consistent with the fact that the peak of the 24 μm emission is spatially displaced from this giant HII region. Such a large ($\sim$1 kpc) and luminous (SFR$\sim 10 M_\odot$/yr) HII region is often seen at $z \sim 2$ but quite rare in the nearby Universe, making this galaxy a good analog to star-forming galaxies at higher redshift.

2.1   Introduction

Star forming galaxies at $z \sim 2$ have clumpy morphologies (Cowie et al., 1995; Elmegreen et al., 2004b,a; Förster Schreiber et al., 2011a,b) and form stars more vigorously than seen in the local Universe. This vigorous mode of star formation is found in the form of "clumpy" giant kiloparsec sized H II regions. Star formation for galaxies at these redshifts occurs throughout their disks at higher rates than their local analogs. There is evidence in the local Universe that these clumps form from the interaction of galaxies. A canonical picture of this interaction can be seen in the Antennae galaxies, where star clusters form where the material (gas and dust) from both galaxies collide. However, at high redshift ($z > 2$), clumps like these form in isolation. These regions are found to be gravitationally unstable and are expected to collapse quickly.

Observations by Livermore et al. (2012) and Wisnioski et al. (2012) have explored clumps at slightly lower redshift at $z = 1 - 2$, and their work suggests an evolution of clump size, luminosity and surface brightness with redshift. As the global star formation rate of the Universe has decreased since the peak at $z \sim 2$ (Madau et al., 1998), it might be expected that the physical properties of the clumps evolve with redshift. This is also supported by the fact that in the local Universe we do not see as many large luminous star forming regions. Galaxies in the early Universe were more

gas rich, leading to greater star formation; as cool dense gas becomes less available, it might be expected that the star formation would decrease along with the size of these regions. Guo et al. (2015) looked at galaxies at redshift $z = 0.5-2$ and found that the clump fraction decreases over time for higher stellar mass galaxies, while lower stellar mass galaxies' clump fraction remains almost constant. In addition, it is suggested that clumps are short lived; either clumps migrate toward the bulge of a galaxy or diffuse within 0.1–1 Gyr (Dekel et al., 2009; Genzel et al., 2011; Guo et al., 2012). Conditions at higher redshift, such as higher gas fractions and cold flow accretion, enabled the regular formation of these clumps.

Field surveys of galaxies at redshift $z \sim 2$ with spatially resolved H ii regions only probe the largest star forming regions, typically kiloparsecs in size (Förster Schreiber et al., 2011a,b). However, this may not necessarily be a reflection of "normal" star forming regions. There may be many more star forming regions unresolved to field surveys, which may better reflect the distribution of normal star forming regions. In addition, with the evolution of clump size and luminosity decreasing through time, it makes it more difficult to detect and characterize lower redshift clumps, even with *HST* resolution. In the cases where large clumps are detected, it is unclear whether they truly are a large clump or some combination of smaller unresolved clumps.

With gravitational lensing it is possible to probe sub-kpc scales, taking advantage of the image of the galaxy being magnified and stretched, resolving many more star forming regions (Jones et al., 2010b; Wisnioski et al., 2012; Livermore et al., 2012; Frye et al., 2012; Wuyts et al., 2014). Gravitational lensing also enables the detection of lower luminosity clumps, where the flux from relatively faint galaxies is amplified by the lens. With these two characteristics, it is possible to detect fainter clumps at sub-kpc scales, even deblending larger clumps into several smaller clumps.

We have seen in the local Universe that star clusters found in star forming galaxies are bright in the ultra-violet (UV) and far-Infrared (far-IR). The far-IR emission is the re-radiation of UV light from young stars that is scattered and absorbed by dust. Star forming regions at high redshift have been primarily studied in the rest-frame

UV due to the availability of high resolution instrumentation in the optical and near-Infrared (near-IR). Far-IR observations are challenging due to the sensitivity, resolution and access to currently available instrumentation and facilities. Only a limited number of galaxies with clumps at high redshift have been studied in the far-IR. In Wisnioski et al. (2013) they investigated the dust properties of 13 UV selected galaxies at $z = 1.3$, from the WiggleZ sample, and found that only 3 were detected with *Herschel*. The remaining 10 were non-detections, below the sensitivity of *Herschel*.

In order to overcome the difficulty of detecting individual star-forming clumps at high redshift in the far-IR/submillimeter we use a gravitationally lensed sample selected with *Herschel*. The *Herschel* Lensing Survey (HLS; Egami et al., 2010) is a survey of massive galaxy clusters in the far-IR/submillimeter using *Herschel* to detect gravitationally lensed galaxies in the submillimeter. HLS consists of two surveys, a deep survey (HLS-deep; 290 hrs) of 54 clusters utilizing PACS (100, 160 μm) and SPIRE (250, 350, 500 μm) and a snapshot survey (HLS-snapshot; 52 hrs) of 527 clusters with SPIRE-only bands. One of the main goals of HLS is to identify and follow-up bright gravitationally-lensed galaxies near the centers of clusters. It is expected that there are very few star-forming and post-starburst galaxies that are cluster members near the projected center of the cluster. Cluster cores at low redshift are dominated by passive galaxies. The main assumption is that the majority of sources emitting in the far-IR near the cluster center are being gravitationally lensed. It would be rare to find cluster galaxies emitting in the far-IR near the cluster core with a notable exception of brightest cluster galaxies (BCGs) in cool-core clusters (Rawle et al., 2012).

Abell S1063 (AS1063, RXJ2248-4431) is a particularly interesting cluster in our sample because it is one of the brightest and most massive galaxy clusters known with an X-ray luminosity of $L_x = 43.2 \pm 0.6 \times 10^{44}$ erg/s (Maughan et al., 2008) and mass $M_{200} = 33.1^{+9.6}_{-6.8} \times 10^{14} M_\odot$ (Gruen et al., 2013; Gómez et al., 2012; Williamson et al., 2011). The X-ray emission (Maughan et al., 2008) and Sunyaev-Zel'dovich signal (Williamson et al., 2011) imply that AS1063 is a relaxed cluster, or virialized. How-

ever, dynamical cluster modelling (Gómez et al., 2012) has shown that it has undergone a recent merger, which is further supported by the weak lensing analysis by Gruen et al. (2013). AS1063's mass and recent merger history make it an exciting candidate for discovering strongly lensed high redshift galaxies. This is because massive clusters, with ongoing merging, often exhibit large expanded critical lines, increasing the area in which lensed galaxies can be discovered. Gruen et al. (2013) has also shown evidence for a possible background cluster at $z \sim 0.6$, which has the potential to be an optimal lensing configuration for finding highly magnified galaxies due to the chance alignment of two mass concentrations along the line of sight (Wong et al., 2012). One of the highest redshift galaxies known to date in AS1063 is a quadruply imaged galaxy at redshift $z = 6.1$, (Boone et al., 2013; Balestra et al., 2013; Monna et al., 2014) which was discovered with multiband *HST* ACS/WFC3 imaging. Recently AS1063 was selected as one of six Hubble Frontier Field clusters, in which deep *HST* ACS and WFC3 imaging will be conducted with the goal of finding the highest redshift galaxies and characterizing the populations of galaxies at redshifts $z = 5 - 10$.

In this paper, we report the discovery of three infrared-bright sources in the core of AS1063. Particularly interesting is the discovery of a luminous kpc-sized star-forming region in one of these sources, which is a cluster-lensed infrared luminous galaxy at z=0.6 (AS1063a). This star forming region, showing up prominently in the HST optical/near-IR images, is similar in size and luminosity to clumpy star forming regions found at higher redshift (z∼2), making this galaxy an excellent lower-redshift laboratory for studying giant star forming regions at z∼2. In addition, the high spatial resolution resulting from lensing magnification allows us to study in detail the nebular emission properties of this galaxy and how they relate to the dust and gas.

The paper outline is as follows. In section 2 we present the sample, observations, and data reduction methods. In section 3 we present the results and measurements of the data. In section 4 we discuss the lens model, the physical properties of the galaxy and the giant luminous star forming region and in section 5 we summarize

our results.

The cosmology used throughout this paper is $H_0 = 70$ km s^{-1} Mpc^{-1}, $\Omega_M = 0.3$, and $\Omega_\Lambda = 0.7$. All magnitudes are in AB magnitudes and all flux densities are in mJy.

2.2   Observations and Data Reduction

2.2.1   Sample

The lensed galaxy in this paper comes from HLS-deep (Egami et al., 2010), which observes a sample of 54 massive galaxy clusters and takes advantage of the lensing power of clusters to detect faint high redshift galaxies (Rex et al., 2010; Combes et al., 2012). The massive clusters are selected by X-ray luminosity and imaged with the *Herschel* Space Observatory (Pilbratt et al., 2010) using PACS (100, 160 μm) and SPIRE (250, 350 and 500 μm).

2.2.2   *Spitzer* Imaging and Spectroscopy

Imaging for AS1063 was obtained (PI: Rieke) at 3.6, 4.5, 5.8, 8.0 μm using the Infrared Array Camera (IRAC; Fazio et al., 2004) on the *Spitzer Space Telescope* (Werner et al., 2004). Each channel on IRAC has a field of view (FOV) of $5.2'\times5.2'$ and pixel size of $\sim1.2''$/pixel. The images had a small dither pattern and were mosaicked together to have a final pixel scale of $0.6''$/pixel. The integration time was 2400 seconds. Additional imaging for AS1063 was also obtained during the warm mission, which is part of the IRAC Lensing Survey (PI: Egami) adding to the depth of channels 1 and 2 (3.6 and 4.5 μm) with an integration time of 18000 seconds. The total integration time for channels 1 and 2 with the warm and cold missions combined are 20400 seconds.

AS1063 is observed with Multiband Imaging Photometer for *Spitzer* (MIPS; Rieke et al., 2004) at 24 μm. MIPS has a FOV of $5'\times5'$ and a pixel scale of $2.45''$/pixel. The observations were part of a program to image the fields of clusters in the Mid-IR (PI: Rieke), the greatest depth covering $6'\times6'$ of the cluster

center with a total integration time of 3600 seconds. Three bright sources were identified immediately near the cluster core (Figure 2.1, top right panel) and were targeted for follow-up. Photometry for both IRAC and MIPS were measured using SExtractor (Bertin and Arnouts, 1996) using the parameters FLUX_AUTO and FLUXERR_AUTO.

An InfraRed Spectrograph (IRS; Houck et al., 2004) spectrum was taken for the brightest *Spitzer*/MIPS 24 μm source, AS1063a (2.5 mJy), in the cluster core in Long-Low mode (14 μm - 40 μm) with an integration of 2400 seconds. IRS in Long-Low mode has a resolution of R=57–126 and pixel scale of 5.1″/pixel along the slit. The 1st and 2nd orders of Long-Low mode have slit widths of 10.7″ and 10.5″ respectively. Line fluxes in the IRS spectrum were measured using PAHFIT (Smith et al., 2007) and are presented in table 2.7.

2.2.3 *HST* Imaging

We used the publicly available *HST* imaging of AS1063 from the Cluster Lensing And Supernova survey with Hubble (CLASH; Postman et al., 2012)). CLASH is a survey to image massive galaxy clusters in 16 bands using the Advanced Camera for Surveys (ACS) and Wide Field Camera 3 (WFC3) with FOVs of $4'\times4'$ and $2'\times2'$, on the *Hubble Space Telescope* (*HST*). The CLASH images were released in two resolutions; 30 mas and 65 mas. We used the 65mas resolution, for the increased S/N, especially in the WFC3 where the 30mas images slightly oversample the PSF. Photometry was measured using SExtractor using the parameters FLUX_AUTO. Deblending parameters had to be carefully considered since initial photometry would be able to separate the clump from the galaxy, but deblending was necessary to remove the nearby foreground galaxy. This was also apparent from the publicly released CLASH catalogs of AS1063. We used the following SExtractor parameters; DEBLEND_NTHRESH = 4 and DEBLEND_MINCONT = 0.005.

2.2.4   Optical Spectroscopy

Optical spectroscopy of AS1063 was obtained with the Low Dispersion Survey Spectrograph (LDSS-3) on the Magellan-Clay telescope on April 16, 2007 and July 15-16, 2007. LDSS-3 is an optical imager/spectrograph with a 4064×4064 STA0500A CCD. LDSS-3 was observed in multi-object mode using the VPH-all grating, covering a wavelength range of 3750-9500$\mathring{A}$, with a resolution of R=860, an 8.3$'$ diameter FOV and a pixel scale of 0.189 $''$/pixel along each slit. 24 μm sources in AS1063 were selected for spectroscopy, including the three bright 24 μm sources near the cluster center. Three masks were observed for the cluster using 1$''$ width slits. For the mask containing AS1063a, the slit was aligned with the major axis of the galaxy based on the archival *HST*/WFPC2 imaging before the CLASH dataset. Each mask was integrated for 45 minutes with conditions of 0.76$''$, 1.09$''$, 0.94$''$ seeing (FWHM).

The LDSS-3 observations were reduced using the COSMOS data reduction package (Dressler et al., 2011). COSMOS performs flat-fielding, wavelength calibration and sky-subtraction which produces a 2D spectrum for each object. The COSMOS data reduction package is based on an optical model of the instrument. COSMOS determines the offsets from the data to the optical model in order to construct a wavelength solution, y-distortion, line curvature, and tilt for each slit. The sky-subtraction algorithm is based on the Kelson (2003) optimal sky-subtraction, in which the sky-subtraction is performed before rectifying the spectra. This method enables better removal of the sky lines and reduces the noise in the final spectra. Stacking of the final spectra is based on the positions of the alignment stars used in the mask. This ensures the maximal amount of flux per object, accounting for any possible movement in the instrument. The dome flats did not have adequate flux in the blue for correcting the slit-to-slit variation of the sensitivity function introduced by the VPH grating. It was necessary to use twilight sky flats to correct for the slit-to-slit variation.

2.2.5 Near-IR Spectroscopy

Near-IR spectroscopy of AS1063a was obtained with the MMT and Magellan Infrared Spectrograph (MMIRS; McLeod et al., 2012) on the Magellan-Clay telescope in longslit mode on April 14, 2012, under poor seeing ($>1.93''$) and non-photometric conditions. MMIRS is a near-IR imager/spectrograph with 2048×2048 HgCdTe Hawaii-2 detector. The spectra were taken with a $1.2''$ width slit using the J grating with the zJ filter, covering a wavelength range of 0.94-1.51 μm, with a resolution of R=800, a $6.9'\times6.9'$ FOV and pixel scale of 0.202 $''$/pixel along the slit. The spectra were taken in 5 minute exposures using a 4 position dither pattern for 4 exposures providing a total integration of 20 minutes on source. The longslit alignment was with the major axis of AS1063a. The spectra were flat-fielded with dome flats, and wavelength calibrated by OH skylines. Frames were subtracted from each other (A-B, B-A) in order to remove the sky emission from the source as well as the dark current. All the frames were median combined into one image using `imcombine` in IRAF with sigma clipping turned on.

2.2.6 *Herschel* Far-IR/Submillimeter Imaging

PACS (Poglitsch et al., 2010) images at 100 and 160 μm were obtained for the core of AS1063 with a FOV of $9'\times9'$ (Egami et al., 2010). The PACS instrument, operating in the dual band photometry mode, consists of two bolometer arrays; a blue channel (32x64 pixels) and a red channel (16x32 pixels). The blue channel has two filters, 60-85 μm and 85-125 μm whereas the red channel has one, 125 - 210 μm, with each channel having a FOV of $1.75'\times3.5'$. Additional 70 μm images were later obtained (PI: T. Rawle) in May 26, 2013, to better constrain the dust temperatures of warm cluster galaxies. Since PACS operates in a dual photometer mode, deeper 160 μm images were also obtained with this program. The PACS maps were generated with UniMap with a pixel scale of $1.0''$, $1.0''$ and $2.0''$.

SPIRE (Griffin et al., 2010) images at 250, 350 and 500 μm were obtained for the field of AS1063 with a FOV of $23'\times26'$. SPIRE in photometry mode has three

bands, 250, 350 and 500 μm, with the bands consisting of 139, 88 and 43 bolometers respectively. Each band has a FOV of $4'\times8'$. The FWHM of the beam size at each band is 17.6$''$, 23.9$''$ and 35.2$''$. SPIRE maps were generated using HIPE v10.0. The pixel scales of each of the maps are 6$''$, 9$''$ and 12$''$, respectively. SPIRE photometry was measured using IRAF task `daophot`.

2.3 Results

2.3.1 Three Bright 24 μm Sources

Figure 2.1 shows the *Spitzer*/IRAC (3.6 and 4.5 μm), *Spitzer*/MIPS (24 μm), *Herschel*/PACS (70, 100, 160 μm), and *Herschel*/SPIRE (250, 350, and 500 μm) images covering the central $1.6'\times1.6'$ area of the massive cluster AS1063. As the figure shows, the cluster core is surprisingly devoid of infrared/submillimeter sources, but three bright sources are clearly detected 24$''$ southwest of the brightest cluster galaxy (BCG). Their IRAC counterparts were unambiguously identified (marked with the green and white circles in Figure 2.1), and the brightest 24 μm source in the north is seen to dominate the observed fluxes in the *Herschel*/PACS and SPIRE bands. The measured flux densities of these three bright 24 μm sources are listed in Table 3.1.

Our follow-up optical spectroscopy showed that the brightest 24 μm source (AS1063a) corresponds to a background galaxy at $z = 0.61$ while the other two fainter 24 μm sources (AS1063b and AS1063c) correspond to cluster galaxies at $z = 0.347$ (Figure 2.2). These redshifts are consistent with those published by Gómez et al. (2012). The near-infrared spectrum of the $z = 0.61$ galaxy shows a strong Hα line at the corresponding wavelength (Figure 2.3). The measured optical/near-infrared line fluxes are shown in Table 2.6.

AS1063a is detected in all three PACS bands (Figure 2.1). At 70 and 100 μm it is distinctly identifiable whereas at 160 μm it becomes blended with AS1063b. The third bright source (AS1063c) is detected at 70 μm and marginally detected at 100 and 160 μm. The sources were not severely crowded and it was possible to get similar photometric values doing both aperture and point spread function (PSF)

photometry. Aperture photometry was used at 70 and 100 μm and PSF photometry was used at 160 μm

At 250 μm AS1063a was blended with the nearby cluster galaxy AS1063b, and crowded field photometry (PSF fitting) was necessary to properly deblend the sources. Within the cluster field it was difficult to find bright well-isolated sources to measure the PSF of the image, so we used an empirical PSF provided by the *Herschel* Science Center. The empirical PSF was binned and rotated to the PA of *Herschel* when it observed AS1063 and after subtracting the sources from the map had a resulting RMS of ~5.9 mJy. At longer wavelengths (350 and 500 μm) the two cluster members are almost completely undetected.

In order to determine the optical/near-IR counterpart of a submillimeter source it is necessary to have several bands spanning a wide wavelength range between the optical and the submillimeter. Sources are traced from the submillimeter to the optical, stepping down in wavelength while ensuring that each source is being followed near the centroid of the original submillimeter source. Sometimes submillimeter sources may be blends of multiple IRAC and MIPS sources. If the sources are not too close (less than a pixel away), then they can be deblended using the IRAF task `daophot` with the IRAC and MIPS position priors. The redshift of the sources can also alleviate source confusion, where dust emission from lower redshift sources may fall below the detection limit for longer wavelength SPIRE bands.

A complete list of 24 μm sources with spectroscopic redshifts is presented in Appendix A. A full analysis will be presented in a future paper.

2.3.2 IR-Luminous Lensed Galaxy at $z = 0.61$

In the infrared/submillimeter range, the most conspicuous source in the core of AS1063 is the infrared-bright galaxy at $z = 0.61$ (Figure 2.1). Its SED was fit using Chary and Elbaz (2001) and Rieke et al. (2009) templates (Figure 2.4). Both template sets are based on SEDs of local galaxies. The best χ^2 model produces a total infrared luminosity, integrated from 8-1000 μm (Kennicutt, 1998), of $1 \times 10^{12} L_\odot$ μ^{-1}, where μ is the magnification factor. The dust temperature was determined to

Table 2.1.   Spectroscopic Redshifts of Three Bright 24 μm Sources

Source	R.A.	Decl.	z	$z_{quality}$	Ref.	ID
AS1063a	22:48:41.760	-44:31:56.53	0.611	4	a	29
AS1063b	22:48:42.113	-44:32:07.39	0.337	4	a	7
AS1063c	22:48:42.480	-44:32:12.99	0.337	4	a	8

Note. — [a] Spectroscopic redshift originally determined in Gómez et al. (2012)

be 35 K by fitting a modified blackbody to the peak of the dust bump with β fixed at 1.5, using Eq. 2.1.

$$S_\nu = N(\nu/\nu_0)^\beta B_\nu(T) \tag{2.1}$$

B_ν is a Planck function, N is the amplitude, and ν_0 is fixed at c/250 μm.

The *Spitzer*/IRS spectrum of this galaxy is shown in Figure 2.5, and the measured line fluxes are listed in Table 2.7. The rest-frame mid-infrared spectrum looks like that of a star-forming galaxy, with a strong PAH feature (11.3 μm). The measured [NeIII](15.5 μm)/[NeII](12.8 μm) line ratio is less than 1 (0.33±0.06), a value typical of a solar-metallicity starburst galaxy (Thornley et al., 2000; Rigby and Rieke, 2004). It is therefore clear that the predominant source of the infrared-luminosity is star-formation and not an AGN. This is consistent with the fact that the measured optical line ratios put this galaxy on the edge of the star forming sequence in the BPT diagram (Figure 2.6)

The *HST* images show that this galaxy has a spiral-like morphology with clearly defined bulge and disk components (Figure 2.7). Our long-slit optical spectrum obtained along the long axis of the galaxy shows a systematic velocity offset from one side to the other (Figure 2.8), likely caused by the rotation of the disk component. The proximity of the $z = 0.61$ galaxy to the cluster center suggests that its gravita-

tional magnification is likely significant although its normal-looking morphology of a spiral galaxy indicates that the magnification effect is not large enough to destroy the intrinsic galaxy morphology, essentially stretching the galaxy in the direction tangential to the cluster center.

Figure 2.1 clearly shows that the brightest infrared/submillimeter emission comes from this lensed galaxy at $z = 0.61$. It is, however, not clear which part of the galaxy is exactly responsible for this strong infrared emission. Figure 2.7 shows that the peak of the brightest 24 μm emission is located 1.27″ SSE from the galaxy nucleus, falling in the middle of the disk. No bright optical/near-IR counterpart is seen at the peak of the 24 μm emission although three smaller star forming clumps are seen nearby in the *HST* images. The 24 μm emission appears resolved in one axis, elongated along the longer axis of the galaxy, suggesting the possibility that the 24 μm emission may originate from multiple components in the galaxy.

Bright Optical Clump with Strong Line Emission

What is most striking about the $z = 0.61$ lensed galaxy, which corresponds to the brightest MIPS 24 μm and PACS/SPIRE source, is its exceptionally bright optical clump seen at one edge of the disk, 2.48″ southeast from the center of the galaxy. The CLASH *HST* data show that this clump is the brightest feature in all of the *HST*/ACS optical bands. In the *HST*/WFC3 near-infrared bands, however, the central bulge becomes the dominant feature.

This bright optical clump appears to have a quite significant size intrinsically. By fitting an elliptical Gaussian to the *HST* F105W (which corresponds to rest-frame Hα) image and subtracting in quadrature a Gaussian point spread function (PSF) measured in the same image, we have derived the spatial size of this clump as 0.547±0.025″× 0.099±0.034″. This corresponds to 3686±171 pc × 670±230 pc at $z = 0.61$ if we do not take into account the lensing effect.

The 2D optical spectrum of the $z = 0.61$ galaxy presented in Figure 2.8 shows that this bright clump emits strongly in line emission (e.g., Balmer lines Hβ - H8, forbidden lines [OII] λ3727, [OIII] $\lambda\lambda$4959,5007, and [NeIII]). Although we do detect

the line emission throughout the galaxy disk, it quickly becomes fainter away from the clump while the Ca II H and K absorption features become more prominent, reflecting an increasing light contribution from an older stellar population in the bulge and spiral arm area on the other side of the galaxy (Figure 2.8).

2.4   Discussion

2.4.1   Lens Model Reconstruction

In order to determine the intrinsic properties of AS1063a it was necessary to remove the effects of gravitational lensing. Modelling of the gravitational lens, in the strong regime, was done with LENSTOOL (Kneib et al., 1996; Jullo et al., 2007; Jullo and Kneib, 2009). LENSTOOL models the cluster lenses by utilizing a non-parametric method, using multiple images and redshifts of lensed background galaxies in order to constrain the model. In the newest CLASH data, we identified 5 multiply imaged systems, one of which was confirmed with a spectroscopic redshift, that were used as input constraints for the lens model (Richard et al., 2014). With the lens model it was possible to determine critical lines and spatial and flux magnifications of the lensed galaxy.

From the lens model we are able to reconstruct AS1063a in the source plane (Figure 3.11 right). Most of the magnification is linear, with very little distortion. There is a slight gradient in the spatial distortion of the galaxy, from the southern edge to the northern edge, $3.7\times$ - $2.5\times$ in linear magnification. In ACS/WFC3 this resolves objects larger than 91 - 134 pc. The LDSS-3 spectrum, at $0.76''$ seeing, spatially resolves 1.38 - 2.05 kpc. The amplification from the southern edge to the northern edge is $4.6\times$ - $3.2\times$, and the amplification at the center is 3.69 ± 0.07. The error in the magnification is the statistical error and does not include systematics such as choice in parameterization/modelling or use of bad constraints/assumptions in the model. AS1063a is $\sim5''$ from the critical line which suggests that is too far for differential magnification to be a significant factor. The bright star forming clump corresponds to the region of the larger amplification at the southern edge of the

galaxy.

The bulge of AS1063a is prominent in the F775W filter and longward wavelengths. When comparing the observed image to the reconstructed image, the galaxy only appears stretched in the observed image (Figure 3.11, left). From the reconstructed image a few noticeable features pop out; there are two spiral arms, a bulge and multiple bright clumps (star forming knots) with one very prominent bright clump (the giant H II region).

We discovered that there is also disagreement with the lens model constructed by Gómez et al. (2012). A redshift was obtained for "Lens B" and "Lens C" as designated by Gómez et al. (2012), which is one of the main constraints for the non parametric lens model. According to our lens model, based on the location of the bright arc, AS1063a or "Lens A", it is well outside the z=0.61 critical line and no additional images are expected for this arc. The suggested counter image to "Lens A", "Counterpart A" is another lensed arc. With the additional resolution provided by the CLASH data, it is clear that the colors do not match the colors of the bright arc, and the bright clump seen in the "Counterpart A" is not the bright clump identified in the bright arc, but highly suggestive of a cluster galaxy.

2.4.2   Physical Properties of the $z = 0.61$ Lensed IR-Luminous Galaxy

Star Formation Rates

When corrected for a magnification factor of 3.69, the intrinsic infrared luminosity of the $z = 0.61$ galaxy becomes $3 \times 10^{11} L_\odot$ with a corresponding star formation rate of 59 $M_\odot$ yr^{-1}. This means that this galaxy is intrinsically infrared-luminous and of the LIRG type (LIRG = Luminous Infrared Galaxy with $L_{IR} = 10^{11} - 10^{12} L_\odot$.)

On the other hand, the SFR derived from Hα is significantly smaller. The observed Hα line luminosity gives a star formation rate of 30 $M_\odot$ yr^{-1}. Corrected for magnification, the value decreases to 8 $M_\odot$ yr^{-1}. When corrected for a visual extinction of $A_{\rm v} = 1.23$ mag derived from the Balmer decrement, the value increases to 25 $M_\odot$ yr^{-1}, but this is still much smaller than the infrared-derived value of 59

$M_\odot$ yr^{-1}. With 42% of the star formation unobscured, the bulk of star formation in this galaxy is obscured by dust.

Using Hβ and Hδ lines seen in the 2D optical spectrum (Figure 2.8), we can derive visual extinctions and extinction-corrected star formation rates for spatially distinct components in the galaxy. Assuming the case B recombination and a Calzetti dust law, the observed Hβ/Hδ ratio gives a visual extinction A_v of 1.23±0.03 mag for the bright clump and 2.32±0.03 mag for the bulge. No such determination was possible for the spiral arm because the Hγ line is too faint. The extinction-corrected Hβ line flux gives an Hα luminosity of (1.25±0.02)×10^{42} erg/s (Case B) for the bright clump. Using a Kennicutt (1998) relation we compute a SFR for the bright clump of 9.86±0.17 M$_\odot$/yr. The HII region contributes ∼40% of the nebular star formation.

Since we see several Balmer emission lines (Hα-H8) in the star forming region, this indicates that the region is undergoing a recent starburst. Such higher order Balmer lines are short lived and suggest a short timescale.

Precise Location of the Infrared Source

As we mentioned in §3.2 the MIPS 24 μm emission is offset from the bulge of the $z = 0.61$ galaxy by 1.27″and elongated, suggesting it is resolved in one axis. One concern is whether the offset is real or if it is a result of astrometric error due to the large MIPS 24 μm PSF. The native pixel scale of the MIPS 24 μm is 2.45″/pixel. However, the image we use is sampled at 1.245″/pixel. In order to compare the bulge position to the MIPS position we need a set of unresolved sources that can be used for astrometry. For the $z = 0.61$ lensed galaxy, the bulge can be identified in the F814W filter, which is also convenient due to the larger FOV of ACS. We used two methods to identify stars in the *HST* F814W images; 1) plotting the difference in the magnitude of two different sized apertures and 2) plotting magnitude versus half-light radius at a fixed aperture. Stars will resemble the PSF of the instrument for a wide range of radii, whereas if just using a FWHM measure, some galaxies may have similar FWHM as a star and lead to a false positive detection. As an additional check, we visually inspected stars to ensure sources were not misidentified and were

not blended with other sources. For sources we believe to be stars, we checked to see whether they are detected in IRAC and also to ensure they are not blended. From our clean list of point sources, we compute the separation angle between the sources detected in ACS and IRAC. We then measure the standard deviation of all the separations, computing the 1σ error in the astrometric position of 0.12″.

At 24 μm many of the sources are unresolved, very few of which are actually stars. In order to determine the astrometric error between IRAC and MIPS we rely on compact sources that are unresolved in IRAC. We use a similar strategy to the one described above to select point sources in IRAC. We compute the standard deviation of the separation angle between the positions in IRAC to the positions in MIPS and find an error of 0.23″. The combined 1σ error in the astrometric positions in ACS, IRAC and MIPS is 0.26″. At 3σ (0.78″) we can confidently say that the offset of the MIPS peak emission is real.

In order to explain the elongation of the source in MIPS 24 μm, we simulate the source by convolving a Gaussian with the MIPS PSF. We then assume the position is at the center of the peak MIPS emission and vary the amplitude while minimizing χ^2. We find that a single source at the peak of the 24 μm emission is not sufficient to account for all the flux in the source, which has significant residual wings. To account for all the flux it appears that more than one Gaussian is needed. We next assume that the far-IR emission could be coming from two locations, offset from the peak emission. Two reasonable locations are the bulge of the galaxy and the star forming region. We find that fitting two Gaussians at those locations works well. The residuals are much smaller with the majority of the flux being accounted for. The solution that works the best is two Gaussians with roughly the same amplitude. However, these solutions are highly degenerate and additional Gaussians could potentially be added for better fits. We can confidently say that a single source being responsible for all of the far-IR emission at the position of the 24 μm emission peak is unlikely. There must be more than one source contributing to the far-IR flux; higher spatial resolution is needed to resolve the situation.

Looking at the IRAC bands, there is a slight bump at 5.8 μm. Based on the red-

Table 2.2.   Stellar Mass of AS1063a

Metallicity	A_v	Age	Stellar mass
$[Z_\odot]$		[Gyr]	$[M_\odot]$
		Entire galaxy	
1.000	1.25	0.651	$2.57^{+1.50}_{-0.95} \times 10^{10}$
0.005	1.61	0.644	$2.95^{+1.73}_{-1.09} \times 10^{10}$
		H II region	
1.000	0.74	0.384	$10.5^{+6.12}_{-3.86} \times 10^8$
0.200	1.15	0.097	$7.1^{+4.14}_{-2.61} \times 10^8$

shift of this galaxy, it is expected that the 3.3 μm PAH feature would be completely in the band. However, the 3.3 μm PAH feature is much weaker than the other PAH features found in star forming galaxies and the bump we see in the SED may not be caused by this feature. It is expected that the majority of light contributing to the flux in the IRAC bands is from stars. If there is flux coming from the 3.3 μm PAH feature, we would need to subtract off the stellar light. To account for the stellar light, we scale the flux in IRAC 3.6 to the IRAC 5.8 μm image and subtract them from each other. We also do the same with the IRAC 4.5 μm image. In each case there appears to be no evidence for residual flux coming from the 3.3 μm PAH feature. If the bump seen in the SED is real, it is possible that the PAH emission could be throughout the galaxy at a low enough level that it might not be seen in the residuals. It appears unlikely that the flux would be originating from an individual region in the galaxy, otherwise it should have been seen in the residuals.

Stellar Mass

We fit the *HST* 16-band photometry to Bruzual and Charlot (2003) models following Pérez-González et al. (2013) in order to determine stellar mass, dust attenuation, and stellar age and population. We assume a Chabrier IMF, Calzetti extinction

and exponentially decreasing star formation history. The models were run fixing the metallicity to solar metallicity and also allowing it to be a free parameter. The SED fitting was conducted on the photometry of AS1063a and just the H II region. The images used for the photometry of the H II region were PSF matched to ensure that we are comparing the same physical region in each band. We used TinyTim to generate the PSF for each of the 16 bands, convolved with the charge diffusion PSF and rebinned to the CLASH pixel scale of 65 mas. The IRAF task `psfmatch` was used to convolve all of the *HST* images to the WFC3/F160W PSF.

The results of the SED fitting can be found in table 2.2. The stellar masses derived from the SED fitting are good to within 0.2 dex, including uncertainties in the IMF and other systematics. AS1063a's stellar mass appears to be unaffected by metallicity as its mass varies by $1.1\times$ for the metallicities considered. In §4.2.5 we describe the metallicity derived from the nebular emission lines in which we find the value is about solar metallicity. For AS1063a we adopt the stellar mass (2.57×10^{10} $M_\odot$) at solar metallicity. The HII region on the other hand is seems to vary by a factor of $1.5\times$ depending on the metallicity. We also adopt the solar metallicity value (1.05×10^9 $M_\odot$), in which it appears to be close to solar metallicity, as we go over in §4.2.5.

When comparing the H II region in AS1063a to ones at higher redshift we find that is about average stellar mass, the high redshift H II regions span $10^7 - 10^{10}$ $M_\odot$. Looking at the samples individually; the HII regions in RCSGA0327 (Wuyts et al., 2014), a galaxy a $z = 1.7$, fall on the lower mass side from $10^7 - 10^8$ $M_\odot$ whereas the Wisnioski et al. (2012) and (Förster Schreiber et al., 2011b) samples are on the higher mass range $10^9 - 10^{10}$ $M_\odot$ and $10^8 - 10^{10}$ $M_\odot$. This can be mostly explained by Wisnioski et al. (2012) and Förster Schreiber et al. (2011b) samples being unlensed, so only the largest most massive H II regions are probed, whereas the Wuyts et al. (2014) sample is a single lensed galaxy probing small H II regions at high spatial resolution.

Using the stellar mass at solar metallicity for AS1063a and the SFR derived from the far-IR, we compute the logarithm of the specific star formation rate (sSFR), which

is 0.36 Gyr^{-1}. We use the analytic fitting function from Whitaker et al. (2012) to determine the log(sSFR) of the star-forming main sequence, which is -0.46 Gyr^{-1} for a galaxy with the same stellar mass and redshift as AS1063a. Galaxies with sS-FRs 4× the star-forming main sequence are considered starbursts (Rodighiero et al., 2011; Noeske et al., 2007). The starburst region for a galaxy similar to AS1063a is log(sSFR) = 0.14 Gyr^{-1}, which means that AS1063a is a starburst.

Kinematics

Spectroscopically, this bright clump appears like an HII region embedded in a rotating disk, with a rotational velocity V_{max} of 134±17 km s^{-1} at $R = 6.2$ kpc, which is also found by Gómez et al. (2012) and Karman et al. (2015). The clump itself shows strong Balmer emission (Hα - H8), forbidden line emission ([O II]λ3727, [O III]$\lambda\lambda$4959,5007, [Ne III]) emission, and its systemic velocity falls on the rotation curve. AS1063a has a smooth rotation curve that flattens out outside of 2 kpc (Figure 2.10). In the reconstructed image (Figure 3.11), AS1063a appears face-on with a slight inclination.

A system in the local Universe with a similar appearance to AS1063a is NGC 5194 (M51), which is a spiral galaxy interacting with another galaxy (NGC 5195). Sofue et al. (1999) looked at the rotation curves of local galaxies and found that NGC 5194 had a peculiar rotation curve (non-Keplerian). NGC3034 (M82), a starburst galaxy interacting with M81, also shows a peculiar rotation curve, in which it has a steep Keplerian decline. In the local Universe it is expected that an isolated spiral galaxy should have a flat rotation curve at large radii (5-30 kpc). Significant bumps or deviations from Keplerian rotation in the rotation curve could indicate an interaction with another galaxy or underlying substructure (subhalos). Kinematically it is difficult to completely rule out AS1063a as a merger, however it appears unlikely.

From the rotation curve we can also measure a dynamical mass. In order to compute an accurate dynamical mass we need to determine the inclination of the galaxy. Using the source plane reconstruction of the galaxy, we measure the axis ratio (b/a) using GALFIT. We find an axis ratio of b/a = 0.4623±0.0023. Assuming

the galaxy is an oblate spheroid (Holmberg 1958), we use equation 2.2 to compute the inclination,

$$cos^2i = \frac{(b/a)^2 - q^2}{1 - q^2} \tag{2.2}$$

where q is the axis ratio for an edge on galaxy. Typically q is 0.13 in spiral galaxies. We compute an inclination $i = 63.6° \pm 0.5°$. The dynamical mass is defined by Eq. 3.2,

$$M_{dyn} = \frac{RV^2}{G} \tag{2.3}$$

where $V = V_r \ sin(i)$, V_r is the radial velocity, and i is the inclination. In order to compare to other samples (Förster Schreiber et al., 2009) we need to determine the velocity at 10 kpc, which should have a comparable amount of dark matter. The maximum velocity flattens out after 4-5 kpc and it is not unreasonable to extrapolate the velocity at 10 kpc. Courteau (1997) demonstrates that the arctangent function is a good fit to galaxy rotation curves in the local Universe in order to determine the circular velocity at a given radius, shown in Eq. 3.1. We fit the velocity curve AS1063a with the arctangent function.

$$V(R) = V_o + \frac{2}{\pi}V_c \ arctan\frac{R}{R_t} \tag{2.4}$$

Fig. 2.10 (right panel) shows the fit to the intrinsic radius. The large error bars and scatter seen in the points that are furthest from the center are due to the low S/N of the fit to the [OII] line. If you allow the [OII] line to be fit at larger radius, the error bar increases significantly, which once again reflects the S/N decreasing.

With the inclination and the circular velocity at 10 kpc, we compute a dynamical mass of 5.1×10^{10} M$_\odot$. This dynamical mass is comparable to the average SINS (Förster Schreiber et al., 2009) galaxy, which spans $\sim$1–20 $\times 10^{10}$ M$_\odot$ for redshifts $z = 1.3 - 2.6$.

Table 2.3.   Metallicity of AS1063a

	$12 + log([O/H])$ R23	$12 + log([O/H])$ N2
Entire galaxy	8.95±0.02	8.67
HII region	8.96±0.02	$\cdots$
Bulge	8.99±0.02	$\cdots$
Spiral arm	8.74±0.10	$\cdots$

Metallicity

As mentioned in §3.2 we detect key emission lines with LDSS-3 and MMIRS for determining metallicity. We use both R23 ([O II]$\lambda3727$, Hβ, and [O III]$\lambda5007$) and [O III]/[O II], and N2 (Hα and [N II]$\lambda6585$) diagnostics to determine the metallicity of the lensed galaxy at $z = 0.61$ and its individual regions. We were unable to detect the [O III]$\lambda4363$ line, a low metallicity indicator, which implies that we should choose the upper branch for R23.

For the N2 measurement we follow the prescription of Pettini and Pagel (2004) using their cubic relation. For the R23 measurement, we follow the prescription of Kewley and Ellison (2008), specifically following the KK04 method. The results for the metallicities can be found in table 4.4. All the values are roughly consistent with solar metallicity. There is some evidence of a metallicity gradient from the spiral arm to the bulge. The metallicity is constant from the bulge to the H II region.

Metallicity gradients are seen in the Milky Way, where the gas-phase metallicity is lower at larger radii than at the bulge. At higher redshift, in $z \sim 2$ galaxies (Jones et al., 2010a, 2013), there is evidence for steeper metallicity gradients. It is suggested that there is inside-out growth in these galaxies that may be responsible for creating the steep metallicity gradients. In local galaxies, the metallicity gradients are flatter, which suggests that the metallicity throughout the disk of a galaxy evolves

over time. In AS1063a, the metallicity gradient is not as steep as seen in $z \sim 2$ galaxies, and appears more like galaxies in the local Universe.

There are known aperture effects when measuring metallicity, where low metallicity regions may be hidden by higher metallicity regions. While it appears that the metallicity is constant between the H II region and the bulge of AS1063a, we may not be sensitive to the lower metallicity regions. This is primarily due to the spatial resolution of the spectra, determined by the seeing, and S/N of the fainter emission lines, such as the [O III]$\lambda 4959$.

The SINGS sample of H II regions (Moustakas et al., 2010) in the local Universe spans metallicities $7.7 - 9.3$ (KK04). The majority of H II regions (88%) have metallicities between $8.6 - 9.2$. The metallicity of the H II region in AS1063a does not seem unusual when compared to the SINGS galaxies in the local Universe as 48% of their H II regions have metallicities between $8.9 - 9.1$. Higher redshift H II regions seem to have lower metallicities when compared to the H II region in AS1063a. Wisnioski et al. (2012) metallicities span $8.4 - 8.8$, Jones et al. (2010a, 2013) span $8.2 - 9.0$. and Wuyts et al. (2014) metallicities spans $8.0 - 8.3$ for several H II regions in RCSGA0327.

Gas Depletion Timescale

In order to estimate the molecular gas mass without a CO measurement there are two methods; (1) using the dust mass from the galaxy's far-IR emission and (2) using the dynamical mass from the galaxy's kinematics.

For the first method in determining gas mass, we need to measure the dust mass. To determine the dust mass from the far-IR emission, we use Eq. 2.5 (Draine 2003)

$$M_{dust} = 4\pi D_L^2 S_{500}/\kappa_{abs} 4\pi B_\nu(T_{dust}) \qquad (2.5)$$

where S_{500} is the rest-frame 500 μm flux, B_ν is the Planck function at the peak T_{dust} and $\kappa = 0.95 \ cm^2/g$ is the absorption coefficient at 500 μm. Using a $T_{dust} = 35.9 \pm 0.4 \ K$ and extrapolating the rest-frame 500 μm flux from the modified blackbody fit to the Herschel photometry we compute $M_{dust} = 7.53 \times 10^7 M_\odot$.

In order to compute the gas mass from the dust mass it is important to know the dust-to-gas ratio (DGR). Sandstrom et al. (2013) shows that there is a correlation between metallicity and the DGR for local star forming galaxies and parameterized it using Eq. 2.6 for metallicities computed using KK04:

$$log(DGR) = a + b(12 + log(O/H) - c) \tag{2.6}$$

where a = -1.86, b = 0.85 and c = 8.39. Using the metallicity found for the entire galaxy from the R23 line ratio we find a DGR = 0.0113.

The relationship between molecular gas, HI and dust is shown in Eq. 2.7 (Sandstrom et al., 2013)

$$\Sigma_D/DGR = \Sigma_{HI} + \Sigma_{H_2} \tag{2.7}$$

Without HI we can only determine the upper limit of molecular gas mass. $M_{gas} = 6.62 \times 10^9 \ M_\odot$.

With the gas mass and far-IR SFR (59 $M_\odot/yr$) we compute the gas depletion timescale of 110 Myr. If instead we assume a more conservative SFR, from the instantaneous SFR derived from Hα (30 $M_\odot/yr$), it would suggest a depletion timescale of 220 Myr. The gas depletion timescale in this calculation is an upper limit, representing the maximum amount of molecular gas that could be in the galaxy, as the HI gas could contribute more and as a result would decrease the gas depletion timescale of the molecular gas.

Comparing the gas mass to the stellar mass gives the gas fraction $f_{gas} = 0.258$. Comparing to other galaxies at this redshift (Daddi et al., 2010; Geach et al., 2011; Magdis et al., 2012), the gas fraction for this galaxy is high but not unusual. The range of gas fractions at z∼0.6 is about 0.05–0.3.

For the second method of determining the gas mass, we use the dynamical mass of the galaxy from §4.2.4. The gas mass is defined as $M_{gas} = M_{dyn} - M_* - M_{dark}$, where the M_{dark} is the dark matter mass. If we assume a dark matter fraction of 0.2 - 0.3 within a radius of 10 kpc (Förster Schreiber et al., 2009) for galaxies $z = 1-3$ we get a gas mass of $M_{gas} = 14.7 - 9.7 \times 10^9 M_\odot$. The gas fraction using the dynamical

mass is defined as $f_{gas} = (M_{dyn} - M_* - M_{dark})/M_*$ which is 0.58 – 0.38. This gas fraction is larger than what we compute using the dust mass. If we use both pieces of information; the gas mass from the first method and the dynamical mass, this would imply that the dark matter fraction is $f_{dark} \sim 0.36$.

In §4.2.2 we find that as much as half of the far-IR flux could be associated with the H II region. Extending this to the molecular gas, if we assume that the molecular gas traces the dust, then roughly half of the molecular gas could be associated with the H II region. This also suggests a similar depletion timescale of 110 Myr. Using the instantaneous SFR derived from Hβ (10 $M_\odot/yr$) for the H II region would suggest a depletion timescale of 340 Myr. Once again, these are the upper limits of the depletion time scale as the initial assumption was that all the gas was molecular, which is not the case. Adding the depletion timescale to the stellar age (0.384 Gyr) of the HII region in AS1063a makes its lifetime 0.5–0.8 Gyr. HII regions at $z \sim 2$ are expected to live between 0.1–1 Gyr (Dekel et al., 2009; Genzel et al., 2011; Guo et al., 2012).

2.4.3   Giant ($\sim$kpc) HII Region Embedded in a Rotating Disk at $z = 0.61$

Taking into account the magnification effect, we divide by the linear magnification, determined by the lens model of the cluster, and find the FWHM of the clump in the source plane is 996±46 pc. In order to compute the error bar for the size of the H II region we ran a Monte Carlo simulation, varying the noise and refitting the elliptical Gaussian for 1000 realizations, then measuring the standard deviation of the width measurements.

*As a Low-Redshift Analog to Giant H*II *Regions at* $z \geq 1$

Figure 2.11 shows the luminosity of individual clumps versus their diameter for nearby galaxies and galaxies with redshifts $z > 1$. When plotted on this relation, the H II region of the $z = 0.61$ lensed galaxy found in AS1063, is more luminous than typical local clumps (by $\sim$2 orders of magnitude) and as large as the largest clumps found locally. This H II region is almost a factor of 10 larger in diameter than the

Table 2.4.   Physical Properties of AS1063a

Parameter	Value	Unit
T	35.9±0.4	K
LIR	3.27×10^{11} (BB)	$L_\odot$
SFR	59 (BB)	$M_\odot$/yr
M_{dust}	7.53×10^7	$M_\odot$
M_*	$2.57^{+1.50}_{-0.95} \times 10^{10}$	$M_\odot$
M_{dyn}	5.1×10^{10}	$M_\odot$
M_{gas}	6.62×10^9	$M_\odot$
Av	1.25 (SED)	mag
f_{gas}	0.258 (M_{gas})	
i	63.6±0.5	deg

mean diameter of local clumps. When comparing to high redshift ($z > 1$) clumps, the H II region is similar in size and luminosity.

Local clumps, on average, are much smaller ($\sim$100-200 pc in diameter) than high redshift ($z > 1$) clumps and less luminous (SFR$\sim$0.0001-0.01 $M_\odot$/yr). However, there are exceptional cases of local galaxies with large star forming regions almost spanning the size range for higher redshift clumps, but at lower luminosity. For comparison one of the largest local H II regions is overplotted in Figure 2.11, NGC 604 in M33.

Local star forming galaxies (from the SINGS sample) appear to fall on a volume dependent empirical relation, where as a clump becomes brighter, it also gets larger. It has been suggested that this relation evolves with redshift in galaxies along the "main sequence", where higher redshift clumps are more luminous than lower redshift clumps for a given size (Livermore et al., 2012). This evolution may be driven by a galaxy's gas fraction where the higher redshift galaxies are found to have higher gas fractions than the local galaxies.

Another key feature is that the clump in AS1063a appears to have formed in

isolation. As we show in §4.2.4 the clump appears to be embedded in a rotating disk with no evidence of interaction. This is typical of the clumps found at high redshift ($z > 2$) but uncommon for local galaxies. For galaxies at low redshift it is found that massive luminous star forming regions are induced by the interacting galaxies. It is suggested that the conditions at higher redshift, higher gas fractions and cold flow accretion, may be responsible for clumps forming in isolation, perhaps due to gravitational instability. They could also be short lived features, as work from Dekel et al. (2009), Genzel et al. (2011) and Guo et al. (2012) has suggested that clumps can migrate or diffuse within 0.1–1 Gyr. We also know that Hα emission traces recent star formation (Kennicutt and Evans, 2012) within the last 3-10 Myr.

It would be expected that such a clump at this redshift would be quite rare. However, two of the largest and brightest clumps in the Livermore et al. (2012) sample ($z = 1 - 1.5$) are at redshift $z = 1.01$ (A773). These clumps are more comparable to the size and luminosity of clumps in the Jones et al. (2010b) sample at redshift $z \sim 2$ and the Wisnioski et al. (2012) sample (WiggleZ). Recent work by Guo et al. (2015) has shown that a galaxies' stellar mass determines the frequency of clumps found from redshifts $z = 0.5 - 2$. The clump fraction remains constant for galaxies with a smaller stellar mass, whereas the clump fraction decreases with time over the redshift range for higher stellar mass galaxies.

2.5 Conclusions

In this paper we present three bright 24 μm detected sources near the cluster core of AS1063. Two of the sources are cluster members (AS1063b and AS1063c) with recent star formation. The third source is a lensed galaxy at $z = 0.61$ (AS1063a). We also present evidence that AS1063a contains a giant H ii region that is about a kiloparsec in diameter and 2 orders of magnitude more luminous than typical local H ii regions, with strong Balmer line emission (Hα-H8) and forbidden line emission ([OII] λ3727, [OIII] $\lambda\lambda$4959,5007, and [NeIII]).

For AS1063a we detected a significant offset in the MIPS 24 μm emission from the bulge region in the galaxy, hinting at a highly obscured region of star formation.

After attempting to determine the source responsible, it seems unlikely that there is a single source at the position of the peak emission. It seems more plausible that there are 2 or more sources contributing to the Mid-IR flux, and the flux could spatially be coming from the bulge and H II region. Furthermore, it was highly suggestive from the SED of AS1063a that there was a slight bump at 5.8 μm. Based on the redshift of AS1063a, it appeared that the 3.3 μm PAH emission feature could be contributing flux to IRAC 5.8 μm band. However, subtracting the stellar flux from the IRAC images there was no significant flux in the residuals.

By measuring the centroid of the [O II]λ3727 doublet, we were able to determine the rotation curve of AS1063a and it appears that the H II region is embedded in a rotating disk. Comparing to a sample of local galaxies by Sofue et al. (1999), we find the rotation curve appears normal (flattening out at large radii) and non-peculiar, which is highly suggestive of a non-interacting galaxy. Even though we are unable to completely rule out a merger, the possibility seems unlikely.

From the far-IR dust emission we can estimate the gas mass using a dust-to-gas ratio and ultimately determine the gas fraction, $f_{gas} = 0.258$. From the kinematics we can also estimate the gas fraction by assuming a dark matter fraction of roughly 20-30%; we get a similar gas fraction as the dust-to-gas ratio suggesting that our gas fraction calculation is reliable. It appears that AS1063a has a gas fraction that is elevated compared to other IR galaxies at that redshift (Daddi et al., 2010; Geach et al., 2011; Magdis et al., 2012) By assuming half of the star formation rate is coming from the H II region, we find that the gas depletion scale is roughly between 130–340 Myr determine from both the far-IR SFR and nebular emission. This suggests that the H II region is short lived.

The H II region in AS1063a is more luminous than local analogs and is unexpectedly luminous for its redshift, resembling an H II region at $z \sim 2$. This could potentially be a rare occurrence, however in the Livermore et al. (2012) sample, two star forming clumps found in a lensed galaxy in A773, have similar luminosity and size at $z = 1.01$. In addition, the giant H II region in AS1063a appears to have formed in isolation, and to have been not induced by a merger. Unlike giant star forming

regions in the local Universe, the giant H II region in AS1063a appears more like the ones found in redshift $z \sim 2$ galaxies. Even though recent studies (Guo et al., 2015) have determined the fraction of clumps in field galaxies at redshifts $z = 0.5 - 2$, they are typically unresolved. Larger samples of gravitationally lensed galaxies will be necessary to determine the distribution of sizes and luminosities of resolved star forming regions.

Table 2.5.   Photometry of Three Bright 24 μm Sources

	AS1063a	AS1063b	AS1063c
Band	Magnitude	Magnitude	Magnitude
	[AB]	[AB]	[AB]
F225W	$\cdots$	$\cdots$	$\cdots$
F275W	$\cdots$	$\cdots$	$\cdots$
F336W	$\cdots$	$\cdots$	$\cdots$
F390W	21.00±0.15	$\cdots$	21.70±0.20
F435W	20.72±0.20	21.72±0.21	21.37±0.13
F475W	20.55±0.08	21.47±0.12	20.85±0.07
F606W	19.81±0.04	20.50±0.04	19.86±0.03
F625W	19.58±0.06	20.28±0.06	19.62±0.04
F775W	19.10±0.04	19.86±0.05	19.22±0.03
F814W	19.01±0.05	19.68±0.06	19.13±0.04
F850LP	18.85±0.08	19.52±0.09	18.95±0.06
F105W	18.54±0.01	19.30±0.02	18.77±0.01
F110W	18.47±0.01	19.16±0.02	18.67±0.01
F125W	18.42±0.02	19.02±0.03	18.54±0.02
F140W	18.25±0.01	18.89±0.01	18.42±0.01
F160W	18.07±0.02	18.75±0.02	18.31±0.02
Band	Flux	Flux	Flux
	[mJy]	[mJy]	[mJy]
3.6 μm	0.35±0.03	0.13±0.01	0.18±0.02
4.5 μm	0.29±0.03	0.12±0.01	0.17±0.02
5.8 μm	0.37±0.04	0.09±0.01	0.10±0.01
8.0 μm	0.30±0.04	0.22±0.02	0.12±0.01
24 μm	2.22±0.02	0.77±0.01	0.27±0.03
70 μm	32.2±2.3	9.0±0.5	$\cdots$
100 μm	69.3±4.9	14.5±1.0	3.7±0.8
160 μm	105.8±7.5	24.8±1.3	$\cdots$
250 μm	69.3±6.8	11.9±5.4	$\cdots$

Table 2.5 (cont'd)

Band	AS1063a Magnitude [AB]	AS1063b Magnitude [AB]	AS1063c Magnitude [AB]
350 μm	36.1±6.2	$\cdots$	$\cdots$
500 μm	21.9±6.1	$\cdots$	$\cdots$

Note. — Herschel errors listed are computed from the RMS of the maps plus the calibration error, which is 5% in PACS and 4% in SPIRE

Table 2.6. Optical and Near-Infrared Emission Line Fluxes of AS1063a

Line	Flux $(10^{-17}erg/s/cm^2)$	$\text{Flux}_{corr}{}^a$ $(10^{-17}erg/s/cm^2)$
Entire galaxy		
[OII]λ3727	123.8±1.5	141.0±1.7
Hδ	10.3±0.8	11.7±0.9
Hγ	25.9±1.1	29.5±1.3
Hβ	74.4±2.0	84.7±2.3
[OIII]λ4959	33.0±2.8	37.6±3.2
[OIII]λ5007	67.4±1.7	76.8±1.9
Hα	130.7±26.1	244.3±48.9
[NII]λ6583	45.2±9.0	84.5±16.9
H II region		
[OII]λ3727	61.6±0.8	70.2±0.9
[NeIII]λ3869	2.9±0.6	3.3±0.7
H8	4.2±0.5	4.8±0.6
Hϵ	2.8±0.4	3.2±0.5
Hδ	7.0±0.4	8.0±0.5
Hγ	17.1±0.5	19.5±0.6
Hβ	42.3±0.7	48.2±0.8
[OIII]λ4959	15.5±0.7	17.7±0.8
[OIII]λ5007	48.3±0.6	55.0±0.7
Bulge		
[OII]λ3727	40.2±0.9	45.8±1.0
Hδ	2.9±0.4	3.3±0.5
Hγ	8.4±0.7	9.6±0.8
Hβ	25.5±1.1	29.0±1.3
[OIII]λ4959	7.4±1.4	8.4±1.6
[OIII]λ5007	14.1±0.8	16.1±0.9
Spiral arm		
[OII]λ3727	9.1±0.5	10.4±0.6

Table 2.6 (cont'd)

Line	Flux	Flux$_{corr}$[a]
	$(10^{-17}erg/s/cm^2)$	$(10^{-17}erg/s/cm^2)$
Hγ	1.3±0.3	1.5±0.3
Hβ	2.4±0.6	2.7±0.7
[OIII]λ5007	2.4±0.3	2.7±0.3

Note. — [a] Flux corrected for slitloss assuming Gaussian profile for seeing.

Table 2.7. Mid-IR Line Fluxes of AS1063a

Line	Wavelength	Flux
	(μm)	$(10^{-17}erg/s/cm^2)$
[ArIII]	9.0	7±15
H$_2$ S(3)	9.7	47±11
[SIV]	10.5	62±13
H$_2$ S(2)	12.2	38±15
[NeII]	12.8	238±16
[NeIII]	15.5	78±13
H$_2$ S(1)	17.0	32±13
[SIII] 18	18.7	167± 8
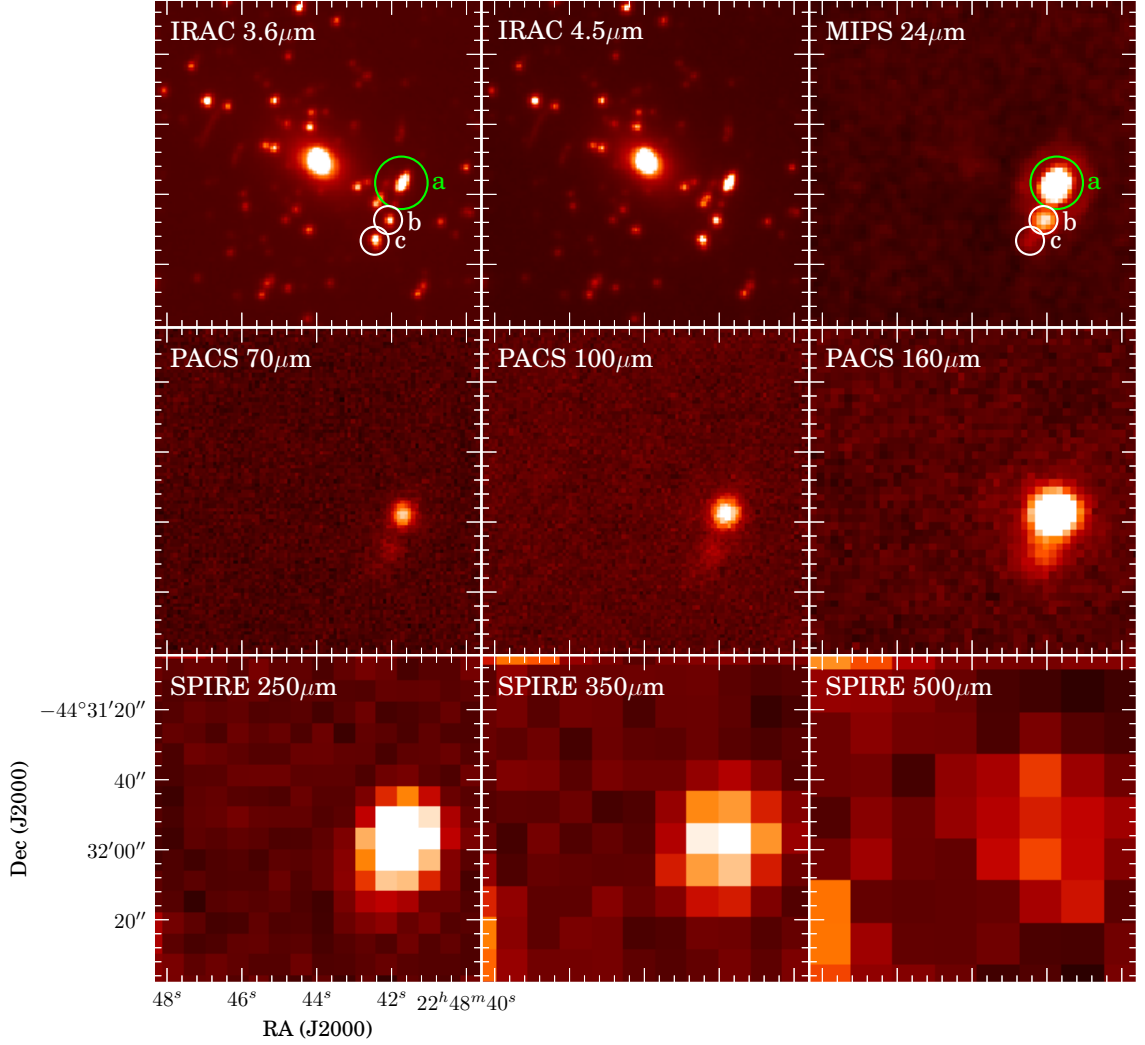
Figure 2.1: Image of the cluster core in *Spitzer* MIPS 24 μm, *Herschel* PACS (100 and 160 μm) and SPIRE (250, 350 and 500 μm). The green circle marks the position of the lensed galaxy AS1063a. The lensed galaxy's FIR SED is fully sampled by MIPS 24 μm, PACS and SPIRE. The white circles mark the positions of the two cluster galaxies ($z_{spec} = 0.336$) which can be seen in MIPS and PACS, but drop out of the SPIRE bands.
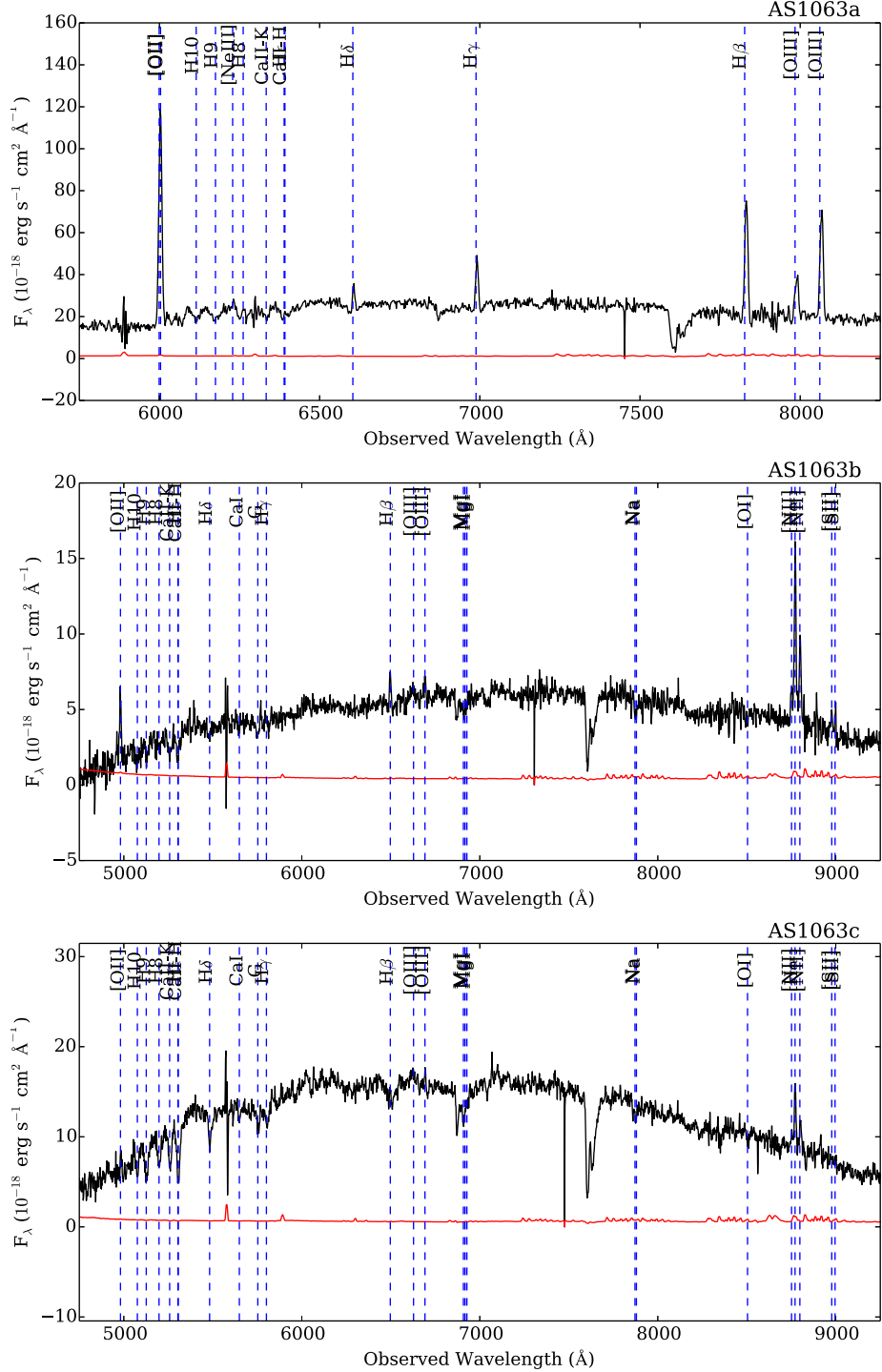
Figure 2.2: Magellan/LDSS-3 optical spectra of the three bright 24 μm sources in AS1063. (Top) Multiple Balmer lines (Hα – H8) are detected in AS1063a suggesting it has undergone a recent burst of of star formation. (Middle and Bottom) We detect Hα in the cluster members (AS1063b and AS1063c) suggesting that they may be falling into the cluster for the first time.
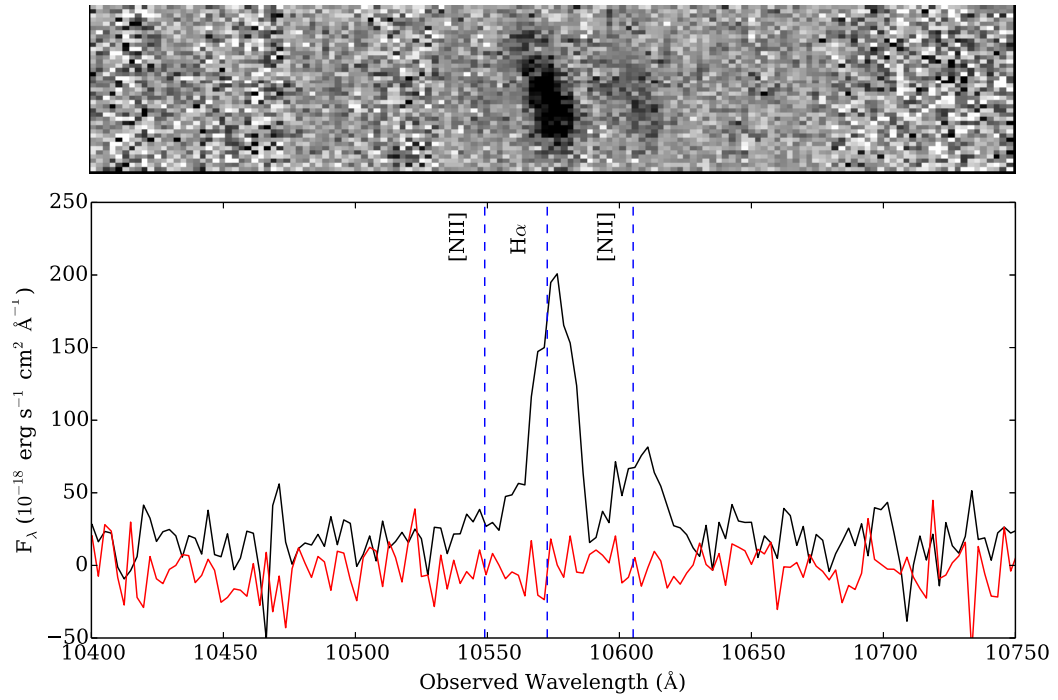
Figure 2.3: Magellan/MMIRS spectrum of AS1063a, Hα and [NII]λ6585 are clearly detected within 20 minutes of integration. The asymmetry of the line is the result of the differential magnification along the source spatially.
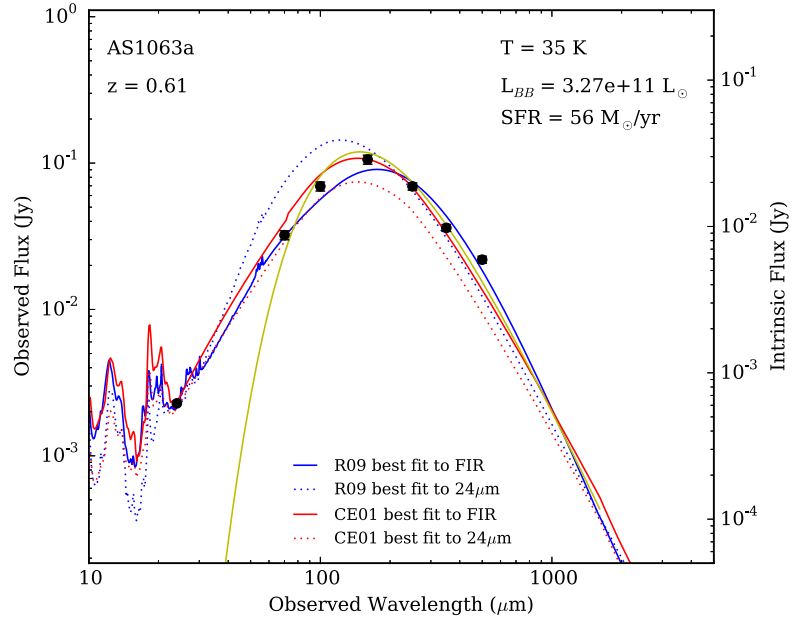
Figure 2.4: SED of the lensed galaxy AS1063a in the core of AS1063. Fits were made to the PACS 70, 100, 160 μm and SPIRE 250, 350 and 500 μm. The 24 μm point was ignored in the fitting of the SED. The solid lines show the best fit to the Rieke 09 and Chary & Elbaz 01 templates to the FIR. The dashed line shows the best fit to the 24 μm point. On the right axis, the observed flux was corrected based on the magnification (3.69±0.07) determined by the lens modelling by LENSTOOL (Jullo et al. 2007).
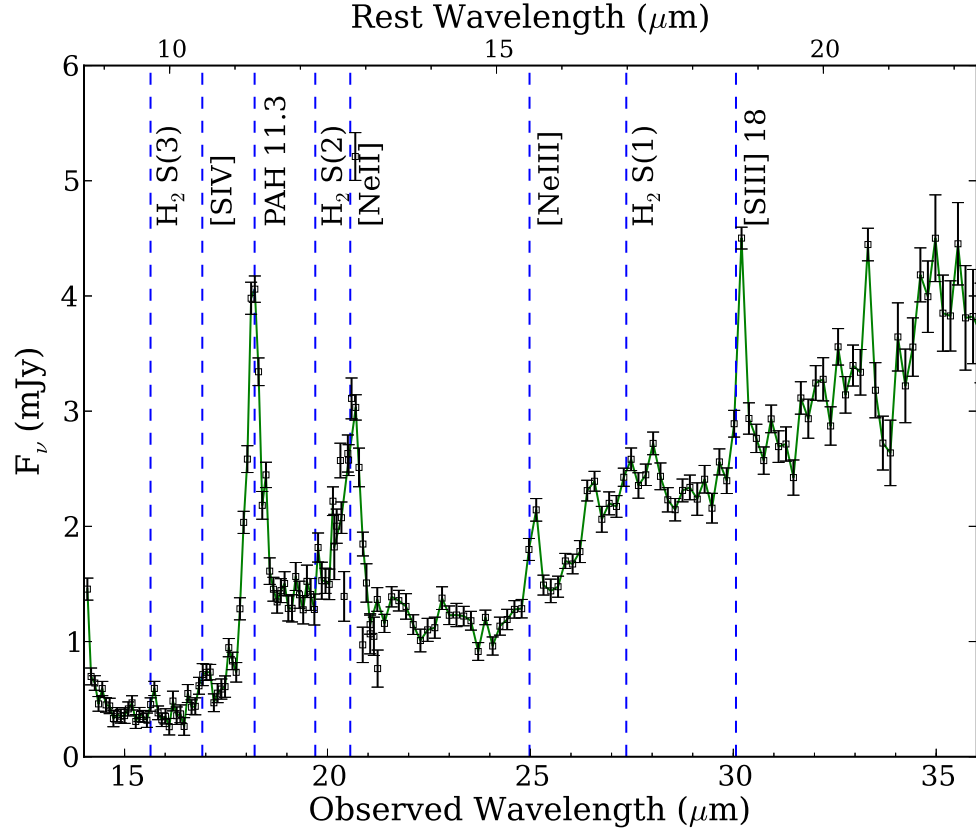
Figure 2.5: The *Spitzer*/IRS spectrum of the lensed galaxy AS1063a. We observe the [Ne III] and [Ne II] lines which we use to determine if our galaxy is undergoing AGN.
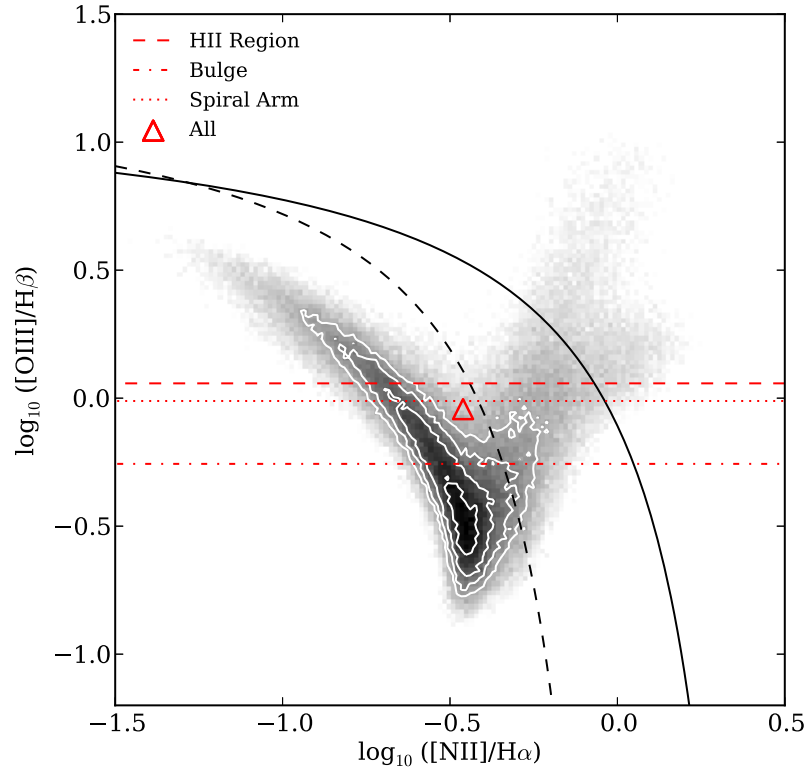
Figure 2.6: The BPT diagram of the three regions within the lensed galaxy AS1063a. The grayscale points are a 2D histogram of SDSS measured line ratios of redshifts between z = 0.005 - 0.25. The red lines mark the [O III]/Hβ ratios of three regions of the galaxy constrained by the optical data. Follow-up NIR observations in poor seeing conditions roughly constrain the [N II]/Hα ratio of the entire galaxy. The black lines mark the Kewley et al. (2001) and Kaufmann et al. (2003) predictions for active galaxy type.
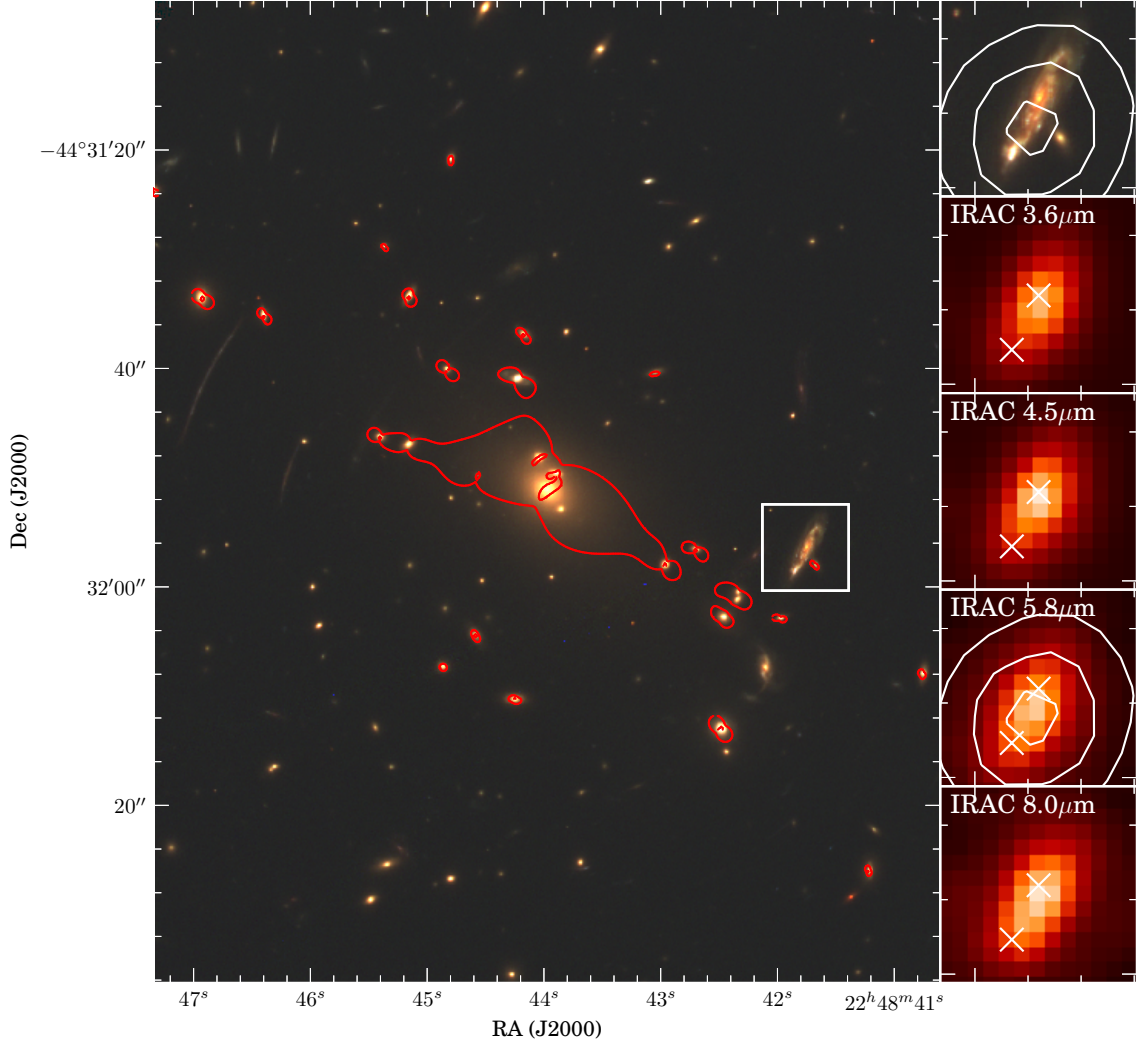
Figure 2.7: (left panel) Three color image of the cluster core AS1063 using *HST* ACS F606W, and *HST* WFC3 F110W and F160W filters. The red line marks the critical line at z = 0.61. (top right panel) Zoomed in three color image of the lensed galaxy AS1063a. The green box marks the position of the slit used for optical spectroscopy of lensed galaxy AS1063a. The white contour marks the position of the MIPS 24 μm contour. White x's mark the positions of the bright star forming region and bulge.
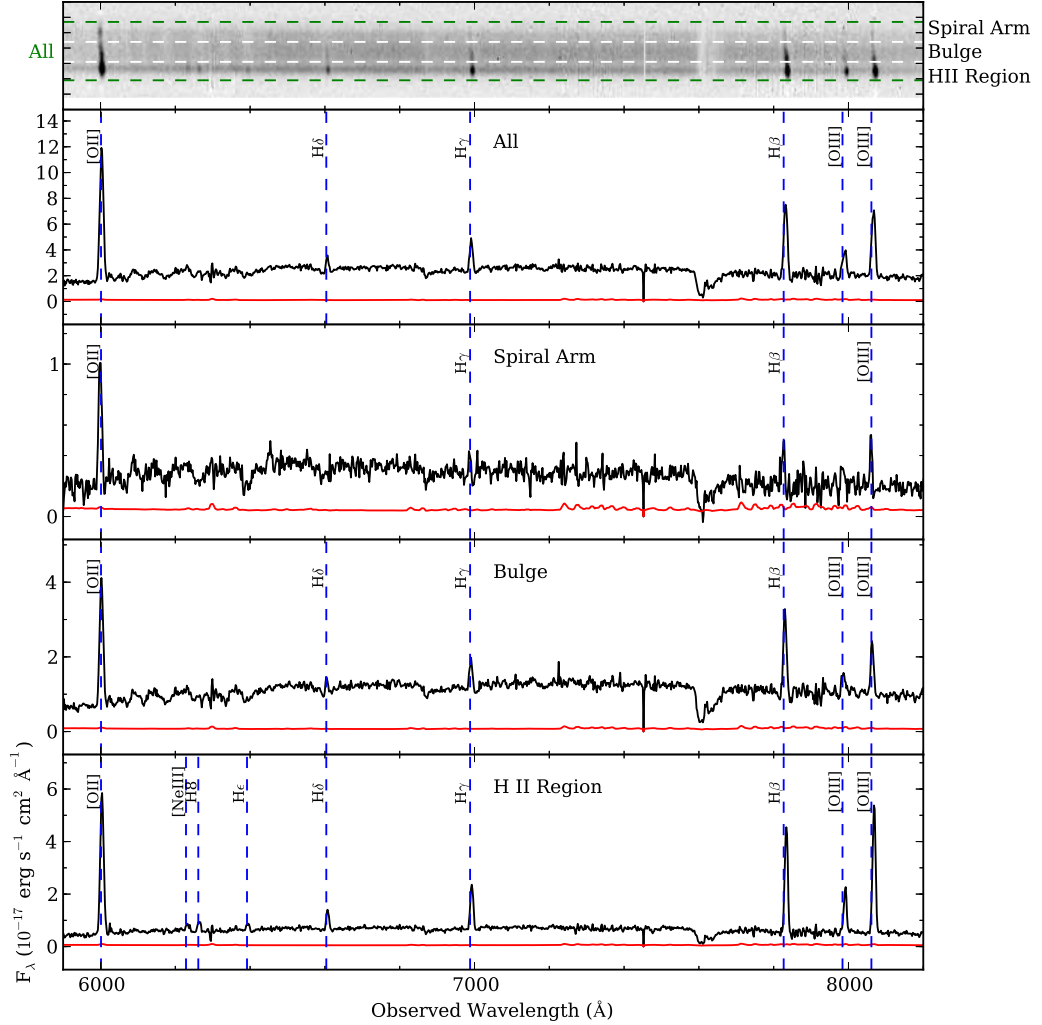
Figure 2.8: (first panel) The 2D spectrum of the lensed galaxy AS1063a taken with Magellan's LDSS-3. (second panel) The 1D spectrum of the entire galaxy. (third panel) The 1D spectrum of the spiral arm. There appears to be an older stellar population, the Balmer lines are the weakest in this part of the galaxy. (fourth panel) The 1D spectrum of the bulge . This region corresponds to the central region of the 2D spectrum and the central region of the lensed galaxy. This region appears to have a significant older stellar population. (fifth panel) The 1D spectrum of the H II region. This region corresponds to the lower bright part of the 2D spectrum. This is the bright star forming clump that is dominated by strong Balmer and forbidden emission lines.
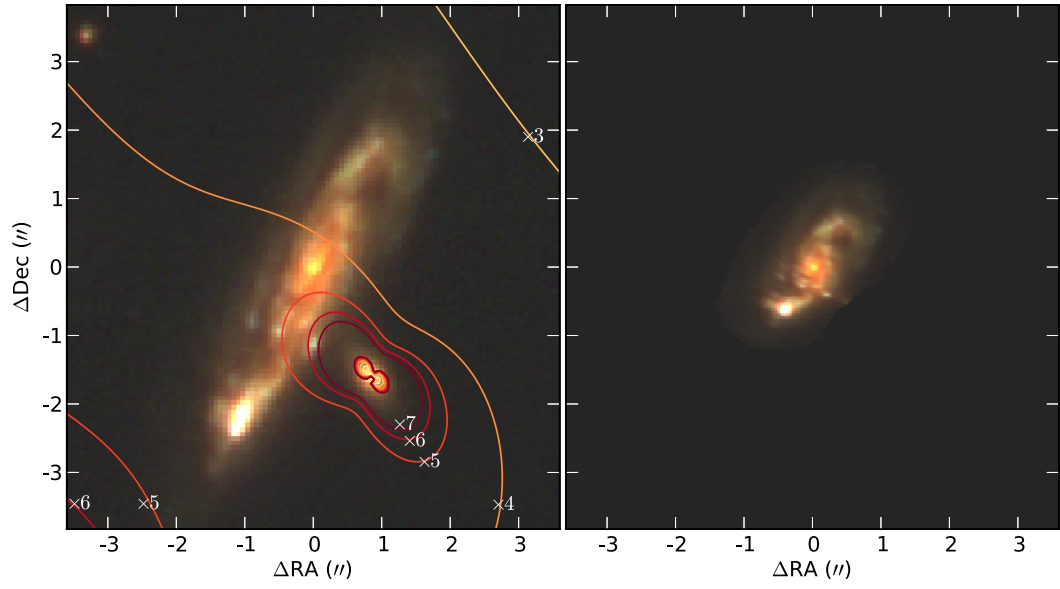
Figure 2.9: (left) *HST* three color image (ACS F606W and F814W, and WFC3 F110W filters) of the lensed galaxy AS1063a. The contours represent the amplification map of the AS1063 lens. (right) The source plane reconstruction performed by LENSTOOL. Most of the magnification is linear along the major axis of the galaxy. The morphology of the lensed galaxy clearly is a spiral galaxy with two prominent spiral arms. The bright star forming clump is the dominant feature in all ACS/WFC3 bands.
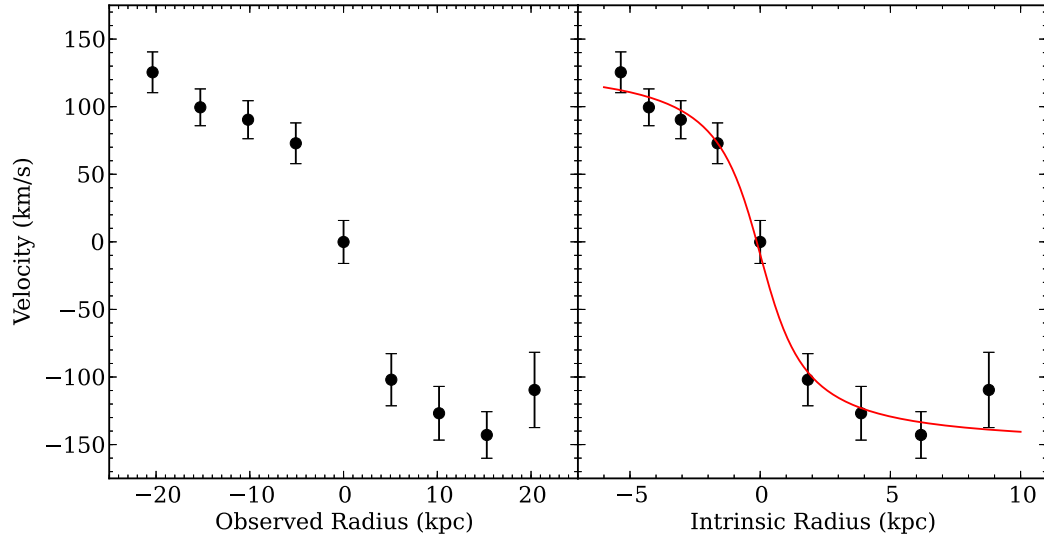
Figure 2.10: (left) The kinematics of the observed [OII] emission line measured from the 2D spectrum. We measured the centroid of the blended [OII]$\lambda\lambda$3726,3729 doublet, which corresponds to [OII] λ3727. [OII] is the brightest feature spatially with the highest signal-to-noise ratio. In order to reduce the noise in the measurement, we binned the data into bins of 4 pixels each (0.76″), which is comparable to the seeing. (right) The intrinsic kinematics of the lensed galaxy AS1063a. The red line is the best fit velocity profile. The galaxy appears to have a slight inclination which is seen by a velocity gradient, suggesting that the galaxy is rotating as one system. The rotation curve appears to be flattening out outside 2 kpc.
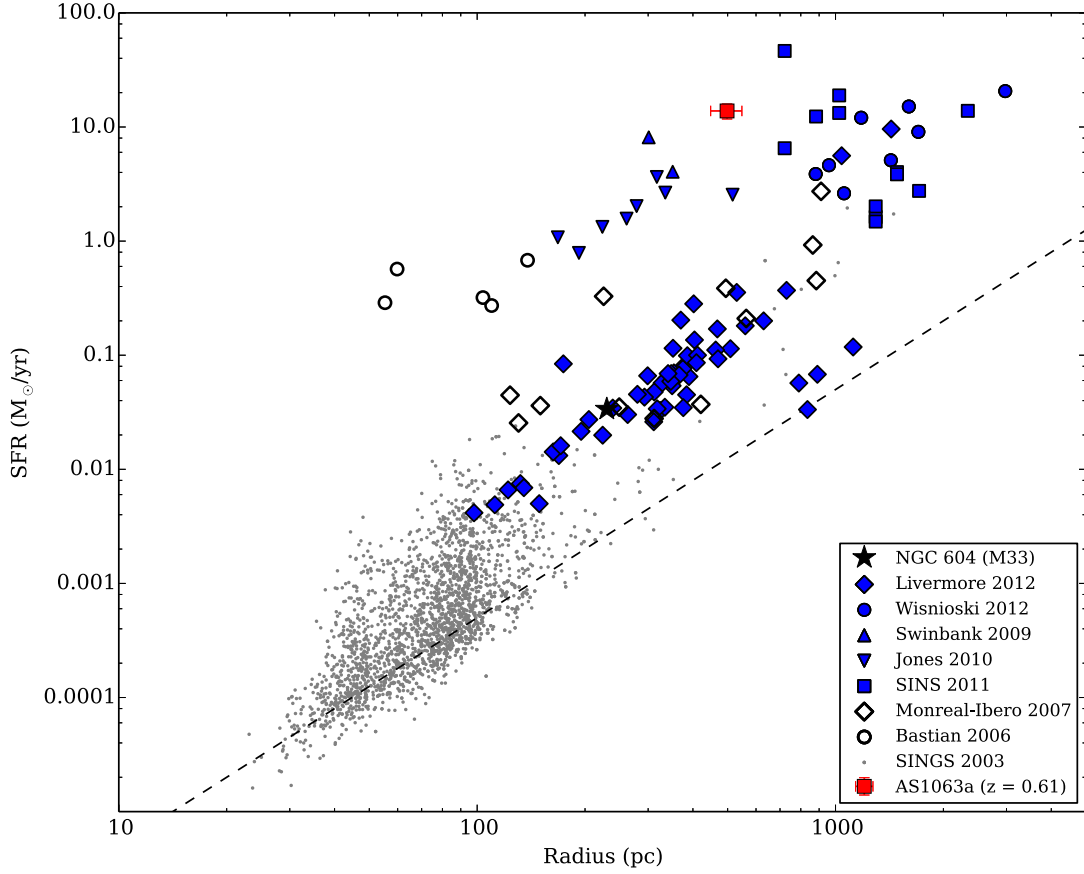
Figure 2.11: Relation between SFR and the radius of H ɪɪ regions (adapted from Wisnioski et al. 2012 and Livermore et al. 2012). The red point is the H ɪɪ region from AS1063a at z = 0.61. The blue points are all galaxies above z > 0.9 combining samples of lensed (Swinbank et al. 2009; Jones et al. 2010; Livermore et al. 2012) and unlensed (Förster-Schreiber et al. 2011; Wisnioski et al. 2012) galaxies. The grey points are from SINGS galaxies (Kennicutt 2003). The open black points are giant H ɪɪ regions found at z∼0 in Antennae galaxies (Bastian et al. 2006) and ULIRGs (Monreal-Ibero et al. 2007). The black star is the giant H ɪɪ region NGC 604 found in M33 (Relano & Kennicutt 2009). The dashed line represents a line of constant Hα surface brightness, which is proportional to R^2.
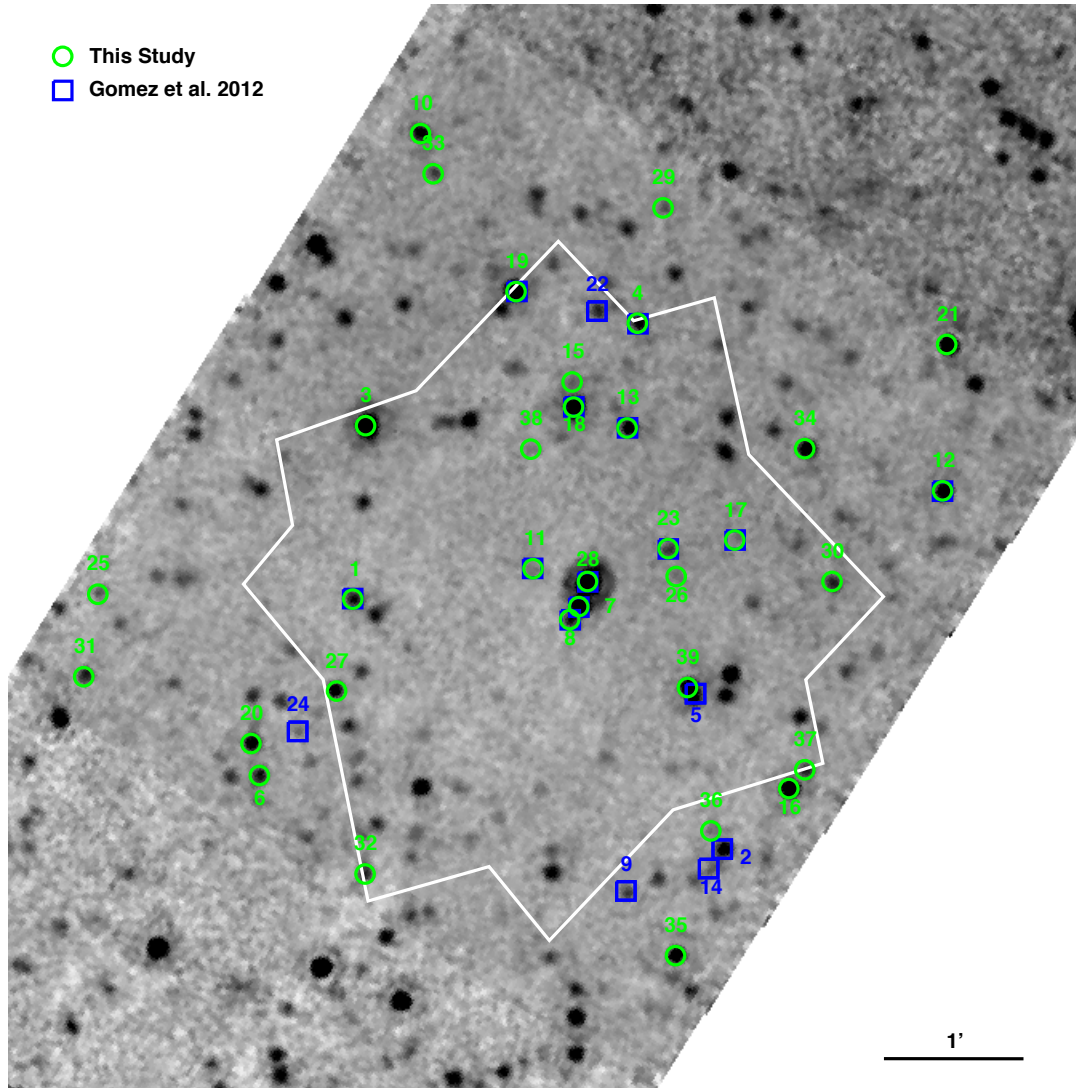
Figure 2.12: *Spitzer*/MIPS 24μm image showing the central $5' \times 5'$ FOV of AS1063. The green circles mark the positions of 24 μm selected galaxies targeted by this study and redshifts determined. The blue squares mark the positions of the galaxies with redshifts from Gómez et al. (2012) which are now known to have 24 μm emission. The white polygon represents the CLASH ACS FOV.

Table 2.8. Spectroscopic Redshifts of 24 μm Selected Galaxies

ID	R.A.	Decl.	$F_{24\mu m}$(mJy)	z	z_q	Ref.	Emission Lines
1	22:48:51.250	-44:32:04.14	0.222±0.010	0.082	4	a	[OII]$_{\lambda 3727}$, Hβ, [OIII]$_{\lambda 4959,5007}$, HeI$_{\lambda 5876}$, [OI]$_{\lambda 6300}$, Hα, [NII]$_{\lambda 6548,6583}$, [SII]$_{\lambda 6717,6731}$ [ArIII]$_{\lambda 7135}$
2	22:48:36.308	-44:33:52.23	0.356±0.013	0.1976		a,b	$\cdots$
3	22:48:50.728	-44:30:49.15	1.234±0.017	0.211	4		[OII]$_{\lambda 3727}$, [NeIII]$_{\lambda 3869}$, Hγ, Hβ, [OIII]$_{\lambda 4959,5007}$, Hα, [NII]$_{\lambda 6548,6583}$, [SII]$_{\lambda 6717,6731}$
4	22:48:39.744	-44:30:04.87	0.220±0.013	0.275	4	a	[OII]$_{\lambda 3727}$, Hβ, [OIII]$_{\lambda 4959,5007}$, Hα, [NII]$_{\lambda 6548,6583}$, [SII]$_{\lambda 6717,6731}$
5	22:48:37.389	-44:32:45.05	0.725±0.016	0.3312		a,b	$\cdots$
6	22:48:55.030	-44:33:20.36	0.250±0.016	0.332	4		[OII]$_{\lambda 3727}$, Hδ, Hγ, Hβ, [OIII]$_{\lambda 5007}$, HeI$_{\lambda 5876}$, Hα, [NII]$_{\lambda 6548,6583}$, [SII]$_{\lambda 6717,6731}$
7	22:48:42.113	-44:32:07.39	0.769±0.012	0.337	4	a	[OII]$_{\lambda 3727}$, Hβ, [OIII]$_{\lambda 4363,4959,5007}$, H$\alpha$, [NII]$_{\lambda 6548,6583}$, [SII]$_{\lambda 6717,6731}$
8	22:48:42.480	-44:32:12.99	0.270±0.034	0.337	4	a	[OII]$_{\lambda 3727}$, Hβ, [OIII]$_{\lambda 5007}$, Hα, [NII]$_{\lambda 6548,6583}$
9	22:48:40.205	-44:34:10.30	0.111±0.010	0.3375		a,b	$\cdots$
10	22:48:48.503	-44:28:42.90	0.257±0.012	0.3409	4		[OII]$_{\lambda 3727}$, Hα, [NII]$_{\lambda 6548,6583}$, [SII]$_{\lambda 6717,6731}$
11	22:48:43.960	-44:31:51.02	$\cdots$	0.347	4	a,c	$\cdots$
12	22:48:27.407	-44:31:17.28	0.342±0.012	0.348	4	a	[OII]$_{\lambda 3727}$, Hβ, Hα, [NII]$_{\lambda 6548,6583}$, [SII]$_{\lambda 6717,6731}$
13	22:48:40.158	-44:30:50.17	0.256±0.014	0.3507	4	a	[OII]$_{\lambda 3727}$, Hβ, [OIII]$_{\lambda 5007}$, Hα, [NII]$_{\lambda 6548,6583}$, [SII]$_{\lambda 6717,6731}$
14	22:48:36.857	-44:34:00.61	$\cdots$	0.3528		a,b	$\cdots$
15	22:48:42.379	-44:30:30.28	$\cdots$	0.354	4	c	$\cdots$
16	22:48:33.617	-44:33:26.01	0.511±0.012	0.335	4		Hβ, Hα, [NII]$_{\lambda 6548,6583}$, [SII]$_{\lambda 6717,6731}$
17	22:48:35.806	-44:31:38.61	$\cdots$	0.335	4	a	[OIII]$_{\lambda 5007}$, Hα,[NII]$_{\lambda 6583}$ [SII]$_{\lambda 6717,6731}$
18	22:48:42.325	-44:30:41.12	0.801±0.017	0.355	4	a	[OII]$_{\lambda 3727}$, [NeIII]$_{\lambda 3869}$,[OIII]$_{\lambda 4959,5007}$, Hα, [NII]$_{\lambda 6548,6583}$, [SII]$_{\lambda 6717,6731}$
19	22:48:44.647	-44:29:51.22	0.728±0.014	0.355	4	a	[OII]$_{\lambda 3727}$, Hα, [NII]$_{\lambda 6548,6583}$, [SII]$_{\lambda 6717,6731}$
20	22:48:55.368	-44:33:06.54	0.304±0.015	0.4026	4		[OII]$_{\lambda 3727}$, Hβ, [OIII]$_{\lambda 4959,5007}$, Hα, [NII]$_{\lambda 6548,6583}$
21	22:48:27.245	-44:30:13.99	0.406±0.011	0.4526	4		[OII]$_{\lambda 3727}$, Hβ, Hα, [NII]$_{\lambda 6548,6583}$, [SII]$_{\lambda 6717,6731}$
22	22:48:41.380	-44:29:59.64	0.122±0.010	0.4535		a,b	$\cdots$
23	22:48:38.502	-44:31:42.29	0.128±0.012	0.457	4	a	[OII]$_{\lambda 3727}$, Hβ, [OIII]$_{\lambda 4959,5007}$, Hα, [NII]$_{\lambda 6548,6583}$, [SII]$_{\lambda 6717,6731}$
24	22:48:53.479	-44:33:01.29	$\cdots$	0.4570		a,b	$\cdots$
25	22:48:43.200	-44:34:01.11	0.280±0.014	0.474	4		[OII]$_{\lambda 3727}$, Hβ, [OIII]$_{\lambda 5007}$, Hα
			0.280±0.014	0.609	3		Hβ

Table 2.8 (cont'd)

ID	R.A.	Decl.	$F_{24\mu m}$(mJy)	z	z_q	Ref.	Emission Lines
26	22:49:01.556	-44:32:01.95	0.049±0.005	0.570	4		[OII]$_{\lambda3727}$, [OIII]$_{\lambda5007}$
27	22:48:38.171	-44:31:54.38	$\cdots$	0.610	3		[OII]$_{\lambda3727}$
28	22:48:51.905	-44:32:43.89	0.244±0.012	0.610	4	c	$\cdots$
29	22:48:41.760	-44:31:56.53	2.223±0.015	0.611	4	a	[OII]$_{\lambda3727}$, [NeIII]$_{\lambda3869}$, H8, Hϵ, Hδ, Hγ, Hβ, [OIII]$_{\lambda4959,5007}$
30	22:48:38.707	-44:29:15.03	0.051±0.007	0.6219	4		[OII]$_{\lambda3727}$, [NeIII]$_{\lambda3869}$, H8, Hϵ, Hδ, Hγ, Hβ, [OIII]$_{\lambda4959,5007}$
31	22:48:32.400	-44:32:59.69	0.065±0.007	0.745	3		[OII]$_{\lambda3727}$, [NeIII]$_{\lambda3869}$, Hβ
32	22:48:31.871	-44:31:56.48	0.167±0.013	0.746	4		[OII]$_{\lambda3727}$, [NeIII]$_{\lambda3869}$, Hδ, Hγ, Hβ, [OIII]$_{\lambda4959,5007}$
33	22:49:02.129	-44:32:37.61	0.206±0.013	0.746	3		[OII]$_{\lambda3727}$, Hβ
34	22:48:58.482	-44:32:41.14	0.083±0.010	0.960	2		[OII]$_{\lambda3727}$
35	22:48:50.756	-44:34:02.97	0.128±0.008	0.969	2		[OII]$_{\lambda3727}$
36	22:48:47.995	-44:29:00.28	0.070±0.007	0.974	2		[OII]$_{\lambda3727}$, Hγ
37	22:48:46.472	-44:33:47.95	0.044±0.007	1.033	2		[OII]$_{\lambda3727}$
38	22:48:36.162	-44:31:01.35	0.264±0.015	1.034	2		[OII]$_{\lambda3727}$
39	22:48:32.980	-44:30:59.08	0.316±0.013	1.035	2		[OII]$_{\lambda3727}$
40	22:48:38.196	-44:34:38.27	0.399±0.014	1.074	4		[OII]$_{\lambda3727}$
41	22:48:36.767	-44:33:44.35	$\cdots$	1.116	3		[OII]$_{\lambda3727}$, [NeIII]$_{\lambda3869}$
42	22:48:32.972	-44:33:17.89	0.138±0.011	1.241	4		[OII]$_{\lambda3727}$, [NeIII]$_{\lambda3869}$
43	22:48:44.053	-44:30:59.34	$\cdots$	1.241	2		[OII]$_{\lambda3727}$
44	22:48:45.450	-44:32:45.75	$\cdots$	1.285	3		[OII]$_{\lambda3727}$, Hδ
45	22:48:37.717	-44:32:42.35	0.725±0.016	1.440	4		CII]$_{\lambda2327}$, [NeIV]$_{\lambda2425}$, MgII$_{\lambda2796,2804}$, [NeV]$_{\lambda3326,3346}$, [OII]$_{\lambda3727}$, [NeIII]$_{\lambda3869}$

Note. — [a] Spectroscopic redshift from Gómez et al. (2012) [b] Source not targeted with LDSS-3 [c] No emission lines detected

Table 2.9.   24 μm Selected Galaxies Targeted without a Redshift

ID	R.A.	Decl.	$F_{24\mu m}$(mJy)
46	22:48:38.351	-44:29:43.46	0.146±0.011
47	22:48:33.829	-44:30:30.27	0.083±0.009
48	22:48:38.390	-44:33:17.88	$\cdots$
49	22:48:51.484	-44:32:59.22	0.153±0.012
50	22:48:35.514	-44:27:54.21	0.232±0.014
51	22:48:52.765	-44:29:30.57	0.650±0.011
52	22:48:36.662	-44:34:19.83	0.072±0.009
53	22:48:38.959	-44:34:05.20	0.121±0.010
54	22:48:37.595	-44:34:54.06	0.234±0.013
55	22:48:26.323	-44:30:46.24	$\cdots$
56	22:48:33.278	-44:30:05.67	0.082±0.008
57	22:48:31.255	-44:30:19.07	0.085±0.007
58	22:48:29.689	-44:30:35.04	$\cdots$
59	22:48:36.515	-44:30:14.18	0.073±0.009
60	22:48:34.301	-44:30:51.34	0.127±0.012
61	22:48:40.691	-44:30:41.67	$\cdots$
62	22:48:46.584	-44:30:46.90	0.249±0.009
63	22:48:36.050	-44:32:36.58	0.432±0.012
64	22:48:50.861	-44:31:22.54	0.130±0.007
65	22:48:53.780	-44:32:26.19	0.087±0.009

Table 2.9   (cont'd)

ID	R.A.	Decl.	$F_{24\mu m}$(mJy)
66	22:49:03.205	-44:32:54.00	0.439±0.011
67	22:48:23.267	-44:30:38.31	0.078±0.006

CHAPTER 3

Two Bright Gravitationally Lensed Dusty Star Forming Galaxies in the Field of
RXCJ2043.2-2144 at Redshifts $z = 2.041$ and $z = 4.68$[†]

We report on the detection of a bright gravitationally lensed *Herschel* source in
the cluster of RXCJ2043.2-2144. This source is one of the brightest sources detected
in the *Herschel* Lensing Survey with a peak flux of $S_{peak} \sim 300$ mJy. We discover
that the source's far-IR/submm emission is a blend of two luminous IR galaxies at
redshifts $z = 2.041$ and $z = 4.68$. High resolution SMA imaging reveals that the
$z = 2.041$ galaxy is an arc ($\sim 8''$ in length), with two bright star forming clumps, and
the $z = 4.68$ galaxy is triply imaged. After deblending the far-IR/submm fluxes and
correcting for the magnification factors, $7.9\times$ in the arc and $17.6\times$ in triplet, the
intrinsic luminosities of the $z = 2.04$ and $z = 4.68$ galaxies are $L_{FIR}=2.4\times10^{12}$ $L_{\odot}$
and $L_{FIR}=6.6\times10^{12}$ $L_{\odot}$ (both ULIRG type). JVLA CO(1-0) observations of the
$z = 2.041$ galaxy show that it has a smooth disk-like rotation. When comparing
the integrated JVLA CO(1-0) maps to the SMA 870 μm maps, we find that a large
fraction of the molecular gas is not contained within the star forming clumps. Further
investigation of the individual velocity channels from the CO(1-0) map reveals that
the two brightest molecular clumps match the locations of the SMA clumps. The

molecular gas unassociated with star formation appears to be part of an outflow seen in the IRAM-30m CO(4-3) observations ($V \sim$-300 km/s, $\Delta V \sim 550$ km/s). This suggests that when comparing the integrated molecular gas mass on a Kennicutt-Schmidt relation, it may under represent the star formation going on in the individual clumps, as some of the gas may be associated with a wind. Finally, we are able to put a constraint on the conversion factor α_{CO} by combining the information from; 1) the dynamical mass, 2) the CO(1-0) line luminosity and 3) the dust emission. We find that $\alpha_{CO} = 4.6\pm1.0$ in the $z = 2.041$ galaxy. The value of α_{CO} is similar to molecular clouds in the Milky Way but much different than in local ULIRGs. However, if we account for the redshift evolution of the star-forming main sequence, the specific star formation rate of the arc places it on the main sequence which typically have α_{CO} values ~ 4.

3.1 Introduction

Dusty, star-forming galaxies are characterized by their far-IR/submm emission, where their dust re-radiates the energy from young stars. These galaxies undergo large episodes of star formation. Locally they contribute very little to the cosmic star formation rate density. However, at higher redshifts, $z = 1 - 3$, luminous Infrared galaxies (LIRGs, 10^{11} – 10^{12} L$_\odot$) and ultra-luminous Infrared galaxies (ULIRGs, 10^{12} – 10^{13} L$_\odot$) contribute a large fraction of the star formation (Le Floc'h et al., 2005; Pérez-González et al., 2005; Caputi et al., 2007; Rodighiero et al., 2010b; Magnelli et al., 2011; Gruppioni et al., 2013). In order to understand how these galaxies go through such large starbursts at these redshifts, we must investigate the conditions of their ISM through their gas and dust. Specifically, by studying the molecular gas of a galaxy, we will understand what is fueling star formation.

Using CO line emission is one of the primary ways for determining the molecular gas mass in a galaxy, as it probes the molecular hydrogen gas or H$_2$. Higher level CO transitions probe warmer gas, influenced by the number of collisions in their environment (Carilli and Walter, 2013), which could be affected by nearby energetic sources, such as AGN. CO(1-0) is more ideal to use as it probes cooler gas. Even as rou-

tine as using CO(1-0) is, it is still necessary to determine the α_{CO} conversion factor, which converts the CO(1-0) line luminosity to a molecular gas mass (Bolatto et al., 2013). In the local Universe it is found that galaxies similar to the Milky Way have α_{CO} conversion factors ranging from 3–6 M$_\odot$ pc^{-2} (K km s^{-1})$^{-1}$ (Leroy et al., 2011; Sandstrom et al., 2013). Locally, more luminous (ULIRGs), star bursting, or merger galaxies have conversion factors similar to 0.8 M$_\odot$ pc^{-2} (K km s^{-1})$^{-1}$ (Casey et al., 2014).

The evolution of the star-forming main sequence (Noeske et al., 2007; Rodighiero et al., 2010a, 2011; Whitaker et al., 2012) plays a major role in value of α_{CO} (Genzel et al., 2015). Recent work by Genzel et al. (2015) shows that for a large sample of galaxies at $z = 0 - 4$, on the star-forming main sequence, have α_{CO} values ∼4. Galaxies with specific star formation rates (sSFR) 4× above the star-forming main sequence are in a different mode of star formation (starbursts), in which α_{CO} is closer to the value of 0.8.

Using the dust mass derived from the submillimeter, or dynamical mass from kinematics (with stellar mass) can help provide better constraints on which α_{CO} to use. Determining dust masses and dynamical mass at high redshift is challenging. The galaxies at higher redshift are smaller from evolution and appear small from Cosmological distance, requiring higher spatial resolution. In addition, the dynamics are less certain, as fewer galaxies exhibit a smooth disk-like rotation and most have a less-ordered rotation (Förster Schreiber et al., 2009). The galaxies at higher redshift have clumpy morphologies (Cowie et al., 1995; Elmegreen et al., 2004b,a; Förster Schreiber et al., 2011a,b) , without clear structures (like disks), making estimates on inclination also difficult. It is even more challenging to determine the stellar mass for the dusty, star-forming population, as many galaxies exhibit regions of large dust obscuration and very little rest-frame optical/near-IR emission escapes. Even when the emission does escape, it is only a small portion of what is detected in the far-IR/submm. Finally, single dish observations of dusty, star-forming galaxies may not accurately determine their dust masses as the submm emission may be a blend of galaxies at different redshifts.

Recent studies of the most luminous high redshift ($z > 2$) dusty, star-forming galaxies in deep fields have shown that 35-50% of LABOCA 870 μm sources resolve into multiple galaxies when using higher resolution ALMA continuum imaging (Hodge et al., 2013). This is problematic as the far-IR luminosities of these sources are being over-predicted as single sources are a result of being blends of multiple sources at lower luminosities. This also suggests that the multiplicity of sources could possibly infer mergers (Tacconi et al., 2008) or columns of galaxies at different redshifts (Hayward et al., 2013). With this multiplicity there is question of whether the correct counterparts are being selected. In Hodge et al. (2013) they found that the correct counterpart in other wavelengths was selected only 55% of the time from the original LABOCA 870 μm sample when comparing to the higher resolution ALMA imaging. This emphasizes the need for high resolution dust continuum imaging in order to determine the multiplicity and the correct counterpart for the far-IR/submm emission.

While multiplicity causes problems estimating the dust mass, stellar winds may cause problems in determining the amount of molecular gas associated with star formation. It is predicted that the star formation in high redshift dusty, star-forming galaxies drives outflows or strong winds. It has been seen locally that 75% of ULIRGs have a wind (Rupke et al., 2002, 2005; Martin, 2005). However, it is less clear whether cold molecular gas can be driven out to suppress star formation. One such case was found in a massive starburst galaxy at redshift $z = 0.7$ (Geach et al., 2014), in which a 1000 km/s wind drove the molecular gas to a distance of 10 kpc outside the galaxy. For lower luminosity galaxies, it may be more difficult to detect a faint wing of outflowing gas, especially since the wind is roughly proportional to star formation. In addition, galaxies with lower star formation rates (SFR) may not drive such a high velocity wind, which means that the gas may not be driven out as far. Such galaxies would require higher spatial resolution in order to detect their outflowing gas. Analytically and numerically we can solve for the amount of energy needed to drive such a wind. However, there are still uncertainties in the mechanisms that drive winds and we do not have any observational constraints on how much star

formation is needed.

While these are all problems that we hope to solve in the next few years with new highly sensitive facilities, such as ALMA, the follow-up with additional facilities will be observationally expensive. In order to get complete wavelength coverage, it makes sense to target bright gravitationally lensed dusty, star-forming galaxies. This will enable follow-up of more typical luminosity galaxies at higher spatial resolutions. Even with the higher sensitivity provided by JVLA, follow-up of gravitationally lensed galaxies (with a magnification factor of $10\times$), for a significant detection of CO(1-0), takes about 2-8 hours of integration; field samples would require much more time. The rest-frame optical and near-IR of dusty, star-forming galaxies are more severely attenuated by dust which would make detecting the stellar continuum more challenging for field samples. In addition, the higher spatial resolution provided by the lensing will probe sub-kpc scales for multiple wavelengths, providing a complete picture of star formation within a galaxy.

Several high resolution studies of dusty, star-forming galaxies that benefit from gravitational lensing such as the SMM J2135-0102 ("Cosmic Eyelash"; Swinbank et al., 2010) at $z = 2.3$ by probing star-forming clumps on the scales $\sim$100 pc. Rawle et al. (2014) shows that a at $z = 5.2$ contains multiple distinct velocity components in several CO transitions as well as in [CII] within 4 kpc in the source plane. More recently Spilker et al. (2015) shows that for two of the brightest sources discovered in SPT at redshifts $z = 2.78$ and $z = 5.66$ the size of the CO emission decreases with the increase in J transition.

Large samples of gravitationally lensed dusty, star-forming galaxies have been found with the surveys H-ATLAS (Negrello et al., 2010), HerMES (Wardlow et al., 2013) and SPT (Weiß et al., 2013). These surveys targeted the brightest sources in the submm/mm which implies that they are all gravitationally lensed. The majority of the sources found in these surveys are galaxy-galaxy lensed systems. However, there are some complications in using galaxy-galaxy lensed systems, such as differential magnification, which complicates the interpretation of the sources intrinsic properties. Cluster lensing may alleviate this problem for sources that are further

away from the critical line, in which magnification varies more smoothly.

The *Herschel* Lensing Survey (HLS; Egami et al., 2010) is a survey of 581 massive X-ray selected galaxy clusters using the *Herschel* Space Observatory with the goal of detecting bright gravitationally lensed dusty, star-forming galaxies. The survey is comprised of two surveys; a deep survey (HLS-deep; 366 hrs) of 54 clusters using *Herschel*/PACS and SPIRE covering 100, 160, 250, 350 and 500 μm and a snapshot survey (HLS-snapshot; 52 hrs) of 527 clusters using *Herschel*/SPIRE covering 250, 350 and 500 μm. The sources are selected with a peak flux cut of $S_{peak} > 100$ mJy and $S_{500}/S_{250} > 0.4$. The implication of sources selected with this criteria, is that they are all gravitationally lensed and at high redshift ($z > 1$). The bright source (HLSJ2043) discovered in the cluster RXC J2043.2-2144 (RXCJ2043) has a peak flux density of $S_{peak} \sim 300$ mJy at 350 μm and *Herschel*/SPIRE flux ratio of $S_{500}/S_{250} \sim 1.5$. RXCJ2043 is a galaxy cluster at redshift $z = 0.2041$, which is part of the REFLEX Galaxy Cluster Survey (Böhringer et al., 2004). Very little is known about the cluster, with only three spectroscopically confirmed cluster members (Guzzo et al., 2009).

In this paper, we present high resolution observations of one of the brightest sources detected in HLS (HLSJ2043) using the SMA and JVLA. The paper outline is as follows. In section 2 we present the sample, observations, and data reduction methods. In section 3 we present the results and measurements of the $z = 2.041$ and $z = 4.68$ galaxies. In section 4 we discuss the lens model of RXCJ2043. In section 5 is the discussion of the $z = 2.041$ galaxy's physical properties, including molecular gas mass, Kennicutt-Schmidt law, and the interpretation of the CO structures, as well as the $z = 4.68$ galaxy's far-IR SED, and finally the $L_{[CII]}$-L_{FIR} relation for both galaxies. In section 6 we summarize our results.

The following cosmology is used throughout this paper; $H_0 = 70$ km s^{-1} Mpc^{-1}, $\Omega_M = 0.3$, and $\Omega_\Lambda = 0.7$. The magnitudes are reported in AB and all flux densities are in mJy.

3.2 Data

3.2.1 Imaging

Herschel

RXCJ2043 was observed with *Herschel*/SPIRE (Griffin et al., 2010) with the bands 250, 350 and 500 μm. The observations of RXCJ2043 have a FOV 14.5′×17.4′ with the greatest depth covering the central 10′. The SPIRE observations were part of the *Herschel* Lensing Survey snapshot program, which took 60 second exposures in each band for each cluster for about 527 clusters. The SPIRE beam size (FWHM) at 250, 350 and 500 μm is 17.6″, 23.9″, 35.2″ respectively. The final reduced SPIRE maps have pixel scales of 6, 9, and 12 ″/pixel.

After the discovery of the bright source, RXCJ2043 was observed with *Herschel*/PACS (Poglitsch et al., 2010) 100 and 160 μm on April 9, 2013 which was part of the proposal OT2_TRAWLE_4. This consisted of 2×840s scan maps (OBSID 1342269731 and 1342269732 for the two cross-scans, 100/160 observed simultaneously), which each have 3′ length scan legs, 3 repetitions and ∼280s true observing (∼560s total). The images were produced from the calibrated time-stream data in the Herschel Science Archive, with map-making via the Generalised Least Squares method of Unimap (Piazzo, 2013). The final reduced maps of RXCJ2043 at 100 μm have a FOV of 4.0′×8.5′ and a pixel scale of 1″/pixel. At 160 μm a FOV of 4.0′×6.6′ and pixel scale of 2″/pixel.

Submillimeter Array

We obtained Submillimeter Array (SMA) 870 μm images of the RXCJ2043 covering 0.85′×0.85′. AIPS was used to reduce the SMA data with a final pixel scale of 0.1″/pixel. The beam size (FWHM) of the map is 1.00″×0.88″ with a PA of -44.32°. The RMS of SMA map is 0.75 mJy/beam.

Spitzer

Spitzer/IRAC (Fazio et al., 2004) imaging of RXCJ2043 was taken on July 15, 2013, during the warm mission with channel 1 and 2 (3.6 and 4.5 μm) as part of HLS IRAC bright lensing survey (PI: E. Egami), where 50 of the brightest sources discovered in HLS were imaged with *Spitzer*/IRAC. IRAC has pixel scale of $\sim$1.2$''$/pixel and each channel has a FOV of 5.2$'\times$5.2$'$. The observations were dithered and mosaicked to cover 6.1$'\times$6.3$'$ with a resampled pixel scale of 0.6$''$/pixel. The total integration time for each channel was 500 seconds.

Spitzer/MIPS (Rieke et al., 2004) imaging was taken in October 29, 2007 during the cold mission, prior to all other observations, as part of MIPS 24 μm Snapshot Survey of Massive Galaxy Clusters (PI: E. Egami). MIPS has a FOV of 5$'\times$5$'$ and a pixel scale of 2.45$''$/pixel. The MIPS observations of RXCJ2043 were dithered and mosaicked to cover 7.5$'\times$8.3$'$, with its greatest depth covering 3.2$'\times$2.9$'$ and resampled pixel scale of 1.245$''$/pixel. The total exposure time at its largest coverage is 480 seconds.

LBT/LUCI

LBT/LUCI K-band imaging of RXCJ2043 was taken May 28, 2011 using the N3.75 camera. LUCI is an imager/spectrograph containing a HAWAII-II 2048$\times$2048 pixel detector with a FOV of 4$'\times$4$'$. The N3.75 camera has a pixel scale 0.12$''$/pixel. The seeing was 1.0$''$. The total exposure time in the K-band is 1120 seconds.

UKIRT/WFCAM

UKIRT/WFCAM J and Ks band imaging of RXCJ2043 was taken June 19, 2014 and June 22, 2014. WFCAM has a field of view 0.21 square degrees and pixel scale of 0.4$''$/pixel. WFCAM consists of 4 HAWAII-II 2048$\times$2048 pixel detectors separated by 94% of the width of a single detector. The data were processed by Cambridge Astronomy Survey Unit (CASU). The average seeing on June 19, 2014 was 0.95$''$ and June 22, 2014 was 0.88$''$. The total exposure in the J-band 1440 seconds and K-band

is 6000 seconds.

Magellan/IMACS

Magellan/IMACS i-band images were taken using the f/4 mode with a total exposure time of 15 minutes: 3 exposures of 5 minutes dithered using a 5-point dither pattern with 0.7′ dithers. The conditions were photometric with 0.51″ seeing. IMACS is an optical spectrograph/imager, the f/4 camera has a FOV of 15.4′×15.4′ with a pixel scale of 0.111″/pixel. The IMACS f/4 camera consists of eight 2K×4K e2v detectors, which make up a 8192×8192 mosaic CCD. The cluster center of RXCJ2043 was placed on chip 5, avoiding the chip gaps. The IMACS images were bias subtracted and flat-fielded. SCAMP and SWARP (Bertin and Arnouts, 1996) were used for determining the astrometry and combining the images.

Millimeter Observations

CSO/Bolocam: We obtained CSO/Bolocam 1.1 mm observations of the cluster RXCJ2043.

   IRAM/GISMO: We obtained IRAM/GISMO 2mm observations of the cluster RXCJ2043 with a FOV of ∼5.2′×∼3.1′. CRUSH was used to reduce the GISMO data with a final pixel scale of 3″/pixel. The beam size (FWHM) of the map is 21″×21″ with a PA of 0.0°.

3.2.2   Spectroscopy

IRAM 30m/EMIR: The 3mm band was observed with IRAM 30m/EMIR to search for CO in order to determine redshift for HLSJ2043.

   JVLA: CO(1-0) was observed for the source HLSJ2043 with the JVLA, covering a FOV of 1′×1′. CASA was used to reduce the JVLA data, with a final pixel size of 0.06″/pixel. The beam size (FWHM) of the map is 1.68″×1.14″ with a PA of -86.10°. We created multiple datacubes where the channel width was 50, 100 and 200 km/s. The S/N was too low for the 50 km/s channel width. Instead, we used the 100 km/s

channel width for analysis as it provided sufficient S/N and velocity resolution. The integrated JVLA CO(1-0) map RMS is 0.039 Jy km s^{-1}/beam. The RMS in each velocity channel is $\sim$0.00014 Jy/beam.

Herschel/**SPIRE Fourier-Transform Spectrometer:** We obtained *Herschel*/SPIRE Fourier-Transform Spectrometer (FTS) observations of the *Herschel* bright source HLSJ2043.

3.3 Results

3.3.1 Counterpart Identification and Morphologies

HLSJ2043 was identified in *Herschel*/SPIRE images with a peak flux density of S$_{peak}$ $\sim$300 mJy near the center of the cluster RXCJ2043 (Table 3.1). The *Spitzer*/MIPS 24 μm image shows a single elongated source with a flux density of 2.54$\pm$0.05 mJy at the position of the *Herschel*/SPIRE 250 μm peak.

At higher spatial resolution (beam FWHM 1.00″×0.88″) the SMA 870 μm continuum image reveals an arc at the position of the MIPS 24 μm source and three additional sources (Figure 3.1, right panel), which we will denote A, B and C.

The arc has two prominent clumps, one near the SE part and one near the NW part, separated by 4.2". The S/N (peak flux) of the SE clump and NW clump are 15.4 and 9.5 respectively (in Table 3.2). The length of the arc using a 3σ threshold is 7.7″ (4σ threshold is 6.7″). We fitted an elliptical Gaussian to each of the clumps and subtracted in quadrature the SMA PSF, allowing the rotation of the Gaussian to be a free parameter. The spatial size of the SE clump is 1.86″×0.94″ (FWHM) at redshift $z = 2.041$ which corresponds to a physical size of 15.5 kpc×7.8 kpc, not accounting for the effect of lensing. The NW clump is 1.21″×1.12″ (FWHM) corresponding to a physical size of 10.1 kpc×9.4 kpc.

Source A is 7.4″ NW of source B, and source C is 8.5″ SE of source B. Compared to the beam size, the sources appear unresolved. Their fluxes are reported in Table 3.3. The sources are all significantly detected with S/N (peak flux) of 8.3, 5.3 and 7.1, for sources A, B and C respectively.

Figure 3.2 shows the multi-band image (Magellan/IMACS i-band, LUCI K-band, UKIRT/WFCAM K-band, *Spitzer*/IRAC [3.6] and [4.5], *Herschel*/PACS 100 μm, and JVLA CO(1-0)) of the cluster core of RXCJ2043, centered on the submm source, with a $\sim$1′ field of view (FOV). The arc identified in the SMA image is also detected in LBT/LUCI K-band, UKIRT/WFCAM J and K band images, *Spitzer*/IRAC [3.6] and [4.5], and *Herschel*/PACS. The sources A, B and C identified in the SMA image are only additionally detected in *Herschel*/PACS.

As we saw in Figure 3.1, the arc and sources A, B and C are blended together in the *Herschel*/SPIRE images. In the LBT/LUCI K-band and the UKIRT/WFCAM K-band image, the arc is 7.7″ in length and 7.8″ SW of the BCG, located near the center of the image of Figure 3.2). On the SE side of the arc in the K-band, there is a bright spot which corresponds to the bright spot seen the SMA and IRAC images. The K-band image of the arc is low S/N and no other prominent features appear. In the Magellan/IMACS i-band imaging there is an extremely faint small clump and thin arcs at the position of the LUCI K-band image and the UKIRT/WFCAM K-band image.

3.3.2   CO Redshifts

We conducted a blind CO search using the IRAM 30m/EMIR to determine the redshift of the bright *Herschel* source HLSJ2043. We detected lines at 101.459, 113.711 and 151.608 GHz. The lines at 113.711 and 151.608 GHz correspond to the CO(3-2) and CO(4-3) lines for a galaxy at redshift $z = 2.041$ (HLSJ2043-S1), shown in Figure 3.3. Zavala et al. (2015) using the LMT/Redshift Search Receiver (RSR) detected lines at 75.827, 81.178, 101.459 and 108.428 GHz. The 101.459 GHz line was detected by both IRAM 30m/EMIR and LMT/RSR. The 75.827 GHz line corresponds to the CO(2-1) line for the $z = 2.041$ galaxy. The 81.178 and 101.459 GHz lines correspond to the CO(5-4) and CO(4-3) lines for a galaxy at redshift $z = 4.680$ (HLSJ2043-S3). The 108.428 GHz line comes from another galaxy as we will show below.

VLT/SINFONI observations of HLSJ2043 (Nakajima et al. in prep) detect Hα in

the SMA arc confirming that the arc is at redshift $z = 2.041$ (hereafter we refer to it as the arc). In addition, Nakajima et al. in prep also serendipitously discover Hβ and [OIII] in the VLT/SINFONI data for a galaxy at redshift $z = 3.25$ (HLSJ2043-S2). The redshift of the $z = 3.25$ galaxy fits the solution of the CO(4-3) line corresponding to 108.428 GHz line detected in Zavala et al. (2015).

Figure 3.3 (top panel) shows the CO(4-3) spectrum. The profile of the CO line is asymmetric and is composed of two components; a bright narrow component ("main component"; FWHM~200 km/s, peak flux ~30 mJy) and a broad faint component ("blue component"; FWHM~550 km/s, peak flux ~10 mJy). The main component also is asymmetric. We fit the CO(4-3) spectral line with 2 and 3 component Gaussians and find that the 3 component model works the best. The asymmetry of the main component requires the extra Gaussian to account for the residual flux. Using the 3 component model the redshift of the main component is $z = 2.041$. The redshift of the main component also corresponds to the redshift of the Hα line detected with VLT/SINFONI. We use this redshift as the systemic redshift of the system.

Zavala et al. (2015) investigated the SMA velocity datacube and discovered a line at 896 μm which corresponds to the [CII] 158 μm line at redshift $z = 4.680$. This confirms that the redshift for each of sources A, B and C is at $z = 4.680$ and that galaxy is triply imaged (hereafter we refer to it as the triplet).

3.3.3 Far-IR SEDs

As Figures 3.1 and 3.2 show, the $z = 2.041$ arc and $z = 4.68$ triplet are heavily blended in *Herschel* PACS and SPIRE images. Therefore, we performed PSF fitting photometry to measure the flux densities of the individual sources accurately, using the source positions measured in the SMA map. The triple images of the $z = 4.68$ galaxy are produced by gravitational lensing, and consequently their flux ratios remain constant regardless of the observed wavelengths. We therefore fixed the flux ratios of the triple sources A, B and C to 7.8:4.4:7.3 as measured in the SMA map. With this additional constraint, only the relative brightness between the $z = 2.041$ arc and $z = 4.68$ was varied to fit all four sources simultaneously with a Markov

Chain Monte Carlo (MCMC) based procedure. Even though the MCMC is good at error estimation, we feel that we are underestimating our errors as we do not allow the source positions to move around or allow the flux ratios to vary based on their errors.

Figure 3.4 shows the SED of the arc using the photometry computed from the MCMC. Modified blackbody fits to the *Herschel*/PACS and SPIRE photometry of the arc suggest that the best solution is a two component temperature fit, with the main component at 26±3 K and a weaker component at 48±6 K. We find that the observed luminosity by fitting Rieke et al. (2009) templates to the photometry and integrating from 8-1000 μm is 1.9×10^{13} $L_\odot/\mu$, a similar value was found using the Chary and Elbaz (2001) templates (2.1×10^{13} $L_\odot/\mu$).

When comparing the dust temperature in the arc (26±3) to other HLS sources in the Hubble Frontier Fields (Rawle et al. 2015), we find that it is lower than the population trend, at the 20% percentile. A similar result is seen when comparing with the samples of Blain et al. (2003) and Hwang et al. (2010).

Figure 3.5 shows the SED of the triplet. We fit local galaxy templates from Rieke et al. (2009) and Chary and Elbaz (2001) to the triplet and find that because of the unusual SED shape, that the local galaxy templates have a hard time fitting it. There appears to be a much warmer component of dust in the triplet than seen in the local templates, which could be a contribution from an AGN. Modified blackbody fits to the photometry suggest a single temperature fit of 71±2 K. We use the modified blackbody to estimate the luminosity of the source. The integrated observed luminosity is $(4.7\pm0.3)\times10^{13}$ $L_\odot/\mu$.

In Zavala et al. (2015), for the triplet, they assumed a dust temperature of T=38±8 K and that a third of the total flux from the blended SED contributed to the far-IR SED. We find that about half of the flux comes from the triplet at $z = 4.68$ and the other half from the arc at $z = 2.041$.

While the modified blackbody fit seems to be consistent with the photometry, it is a bit unphysical, as even AGNs have a cool dust component in them. Fitting the photometry with a fixed temperature modified blackbody at 30 and 40 K produces

poor fits. Much of tension is between the 500 μm and 870 μm photometry. This is suggestive that we may be underestimating the errors in the *Herschel*/SPIRE fluxes.

Another possibility is that there could be another source contributing to the far-IR/submm flux. While the $z = 3.25$ galaxy (Nakajima et al. in prep) is in the *Herschel* beam, it is undetected in the SMA image. Assuming that it is detected in the SMA map at 5σ and it has a 30 K temperature modified blackbody, it would contribute <8 mJy in SPIRE 500 μm. There is evidence that the $z = 3.25$ galaxy is doubly imaged (Nakajima et al. in prep), therefore it would contribute <16 mJy. This is not nearly enough to make up the discrepancy between 500 μm and 870 μm photometry and it seems like this scenario is unlikely.

3.3.4   The $z = 2.04$ Arc

CO(1-0)

- *CO(1-0) Integrated Image*

Figure 3.6 shows a zoom-in of the arc at $z = 2.041$ (LUCI K-band, WFCAM K-band, IRAC [3.6] [4.5], SMA 870 μm and the integrated JVLA CO(1-0) image). Over-plotted are contours from the SMA 870 μm continuum emission. CO(1-0) emission is detected along the length of the arc, corresponding to the emission seen in the K-band, IRAC [3.6] and [4.5], and SMA 870 μm. The bright spot identified in the K-band, IRAC [3.6] and [4.5], and SMA 870 μm image is also seen in the CO(1-0) integrated image. The length of the arc in CO emission using a 3σ threshold is 6.5″ (4σ threshold is 5.8″). In the integrated CO(1-0) emission we identify 4 clumps (listed in Table 3.4). Clumps C1-C3 all are significantly detected with a S/N > 5 (peak flux of each clump). Clump C4 is a tentative detection with a S/N of 4.4.

Comparing the clumps that we identify in the JVLA CO(1-0) image to the clumps in the SMA 870 μm image, we find that they do not correspond to each other. Not only are there more clumps in the integrated JVLA CO(1-0) image (3-4 clumps) but they do not correspond to the peak positions of the clumps in the SMA 870 μm image. Clump C2 in the JVLA image is offset by $\sim$1″ from clump SE in the SMA

image, and clump C3 in the JVLA image is also offset by $\sim1''$ from clump NW in the SMA image (shown in Figure 3.6).

- *CO(1-0) Velocity Slices*

Figure 3.7 shows the individual velocity bins for the JVLA CO(1-0) emission, with the SMA 870 μm contours over-plotted. We identify several clumps for all of the velocity bins (listed in Table 3.5). The clumps are labeled with a prefix of "V" to signify that they were identified in the individual velocity slices. The number corresponds to the velocity channel where the clump is identified, labeled in the bottom right corner of each velocity slice. Multiple clumps in a velocity channel are labeled a suffix a or b, with the brightest clump identified as a and the next brightest with b. All of the clumps, except for V6b, have a S/N > 5. Clump V6b is a tentative detection with a S/N of 4.8.

CO(1-0) emission is detected spanning the velocity range -400 to 200 km/s, with a gap in emission at -300 to -200 km/s. From the CO(1-0) we find that the NW corner of the arc is redshifted from the systemic velocity and the SE corner is blueshifted. Starting from the NW corner, moving along the arc towards the SE corner, the CO emission spatially follows the position of the arc with the velocity moving blueward.

The CO(1-0) emission has two distinct spatial structures, the bright clumps (V1, V3, V4a, V5a, V6a) and the faint clumps (V4b, V5b, V6b). The bright clumps (main structure) appear to move along the arc in each velocity channel, whereas the faint clumps (secondary structure) roughly seem to be located in the same spatial position for a large range of velocities ($\Delta \sim$300 km/s). The two structures merge in -200 to -100 velocity bin (or clump V3).

Figure 3.8 shows three projections of the CO(1-0) in velocity, x-axis (RA), and y-axis (Dec). The projections show the maximum value through the datacube at a given position. Comparing the projection of CO(1-0) (Figure 3.8, top left panel) to the integrated CO(1-0) (Figure 3.6, bottom right panel), the brightest clump is now in the NW. When looking at Figure 3.7 (panel 5), the brightest clump in the projection is actually clump V5a. The brightest clump in the integrated CO(1-0) (clump C2), which is no longer the brightest clump in the projection, is actually

the combination of multiple fainter clumps in velocity space, shown in Figure 3.8 both right and bottom panels. These panels show more clearly what we mentioned previously, that there are two structures; the bright main structure of the galaxy which is rotating smoothly, and fainter secondary structure which is cospatial and spans a velocity range of 300 km/s.

- *CO Line Profiles*

Comparing the spectral line profiles of the CO(1-0) (Figure 3.9) and CO(3-2) (Figure 3.3, bottom panel) to the CO(4-3) (Figure 3.3, top panel), we find that they look similar. The velocity channel width is coarser in the CO(1-0) and CO(3-2) than in the CO(4-3). Re-reducing the CO(1-0) spectral line to a finer velocity channel width reduces the S/N too much to do analysis on the line. For the coarser velocity channel widths of the CO(1-0) and CO(3-2) spectral lines, it is only possible to do a two component fit; three component fits over-parameterize the data. Therefore, we adopt a two component fit for the CO(4-3) emission, which allows us to do a direct comparison of each of the components, in particular the main and blue components. The line measurements are listed in Table 4.3.

[CII] Emission

Herschel/SPIRE FTS observations detect an emission line at 480 μm which corresponds to [CII] 158 μm line at the redshift of the arc $z = 2.041$ (shown in Figure 3.10). In order to measure the line flux we use a sinc function to fit the line, following the Herschel Data Analysis Guide. The CO line widths are ∼250 km/s, which means the [CII] line could be partially resolved. For partially resolved lines one would use a sinc function convolved with a Gaussian function (sincGauss) to fit the line profile. Comparing the flux ratios between the sinc function and the sincGauss function at 625 GHz for a 250 km/s line would only require a correction in the flux by a factor of about 1.04. Based on this information we conclude that the sinc function is the appropriate function to use to measure the line flux, which is reported in Table 4.3.

3.4 Lens Model

We use LENSTOOL (Jullo et al., 2007) to model the gravitational lens of the cluster RXCJ2043. LENSTOOL uses the size and redshifts of cluster galaxies as well as the background galaxies to model the mass distribution of the cluster. The triplet identified in the SMA data at redshift $z = 4.68$ (Zavala et al. 2015) and the doublet identified in the VLT/SINFONI data at redshift $z = 3.25$ (Nakajima et al. in prep) are used to constrain the lens model. The model is parametrized by a single cluster-scale potential centered on the BCG as well as a few galaxy-scale potentials on cluster members. The lens model enables us to determine the intrinsic properties of the background galaxies, specifically the arc and the triplet.

In the arc, the lensing configuration suggests that it is a single image and outside the critical line at redshift $z = 2.041$. Evidence that the arc is singly imaged is supported by the fact that the triplet, at higher redshift, is interior to the arc. Figure 3.6 shows the lensing configuration of the system, with the red line showing the critical line at $z = 2.041$. The arc $\sim 2''$ from the critical line which suggests that differential magnification not a factor in this case. Differential magnification occurs when a source is extremely close to or crosses the critical line in which a variation in magnifications occurs for distinct regions within the galaxy (Blain, 1999; Hezaveh et al., 2012). The flux weighted magnification based on the SMA map is 7.9±1.6. The error in the magnification is the statistical error and does not include systematics such as choice in parameterization/modelling or use of bad constraints/assumptions in the model. The linear magnification along the arc ranges from $5.3\times - 8.1\times$, with the SE and NW edges of the arc experiencing the least amount of linear magnification and the region between the SMA and CO clumps experiencing the most. This means that the bright spot seen in the SE part of the arc in IRAC [3.6] and [4.5] is not an effect of larger amplification, but more near-IR emission coming from that region than the rest of the arc. Interestingly, the highest magnification occurs at the center of the arc, which would imply that a higher S/N near-IR image might show a darker spot between the SE side and NW side of the arc. The linear magnification perpendicular

to the arc is $1.2\times - 1.3\times$.

From the lens model we reconstruct the source plane image of the JVLA CO(1-0) integrated image and the SMA 870 μm image (shown in Figure 3.11). At $z = 2.041$, $1'' = 8.4$ kpc. The SMA beam size (FWHM $= 1.00'' \times 0.88''$) resolves spatial scales of $1.5 - 1.0$ kpc along the arc and 6.4–7.0 kpc tangential to the arc. Similarly, the JVLA beam size (FWHM $= 1.68'' \times 1.14''$) along the arc resolves spatial scales of 2.6 – 1.7 kpc and tangential to the arc 11.7–10.8 kpc.

As mentioned before, the triplet is a triply imaged galaxy (shown in Figure 3.2). Confirmation of the redshift of each of the images came from the detection of [CII] 158 μm emission line in the SMA velocity cube, reported in Zavala et al. (2015). Images A and C are positioned outside of the $z = 4.68$ critical line, while image B is inside the critical line as expected in this type of lensing configuration. Images A, B and C have the following magnifications; 7.1 ± 1.4, 4.6 ± 0.9, and 5.9 ± 1.2 for a total magnification of 17.55 ± 2.1.

3.5 Discussion

3.5.1 The Intrinsic Far-IR SEDs

For the arc, when taking into account the magnification factor of $7.87\times$, the intrinsic luminosity is 2.4×10^{12} L$_\odot$, which makes it a ULIRG. From the Kennicutt (1998) relation we compute a star formation rate of 417 M$_\odot$ yr^{-1}.

For image A in the triplet, when taking into account the magnification ($7.10\times$), the intrinsic luminosity of galaxy is $(6.6\pm0.4)\times10^{12}$ L$_\odot$, which makes it a ULIRG. From the Kennicutt (1998) relation we compute a SFR$_{FIR}$ of 1145 ± 72 M$_\odot$ yr^{-1}.

3.5.2 The $z = 2.04$ arc

Stellar Mass

LEPHARE (Arnouts et al., 1999; Ilbert et al., 2006) was used to determine the stellar mass, dust extinction and stellar age from the *Spitzer*/IRAC and UKIRT/WFCAM photometry of the arc. Specifically we used Bruzual and Charlot

(2003) stellar population synthesis models with a Chabrier IMF and an exponentially decreasing star formation rate. Nakajima et al. in prep found a $0.2''$ spatial offset in the source plane between the submm data and optical/near-IR data which requires us to use a different magnification to compute the intrinsic physical properties from the SED. The optical/near-IR images are located closer to the critical line, resulting in a magnification of $10.04\times$. The offset between the optical/near-IR images and submm images will be discussed further in Nakajima et al. in prep. The best fit SED predicts a stellar mass of $5.62^{+3.71}_{-1.25} \times 10^{10}$ M$_\odot$, $E(B-V) = 0.80$ ($A_V = 3.24$) and age of 53^{+83}_{-19} Myr.

The Förster Schreiber et al. (2009) SINS sample, which is a sample of star forming galaxies at redshifts $z = 1.3 - 2.6$, spans a stellar mass range of 0.2–30×10^{10} $M_\odot$. Twenty-three percent of the galaxies within this sample have a stellar mass range of 3–10×10^{10} $M_\odot$, similar to the arc. Only 17% of the galaxies in the lowest age bins have a similar stellar age (50-150 Myr) as the arc. It should be noted that the photometry from the SINS sample was modelled using Maraston (2005) stellar population synthesis models, in which the ages are typically $2\times$ younger than Bruzual and Charlot (2003). Finally, the dust attenuation in the SINS sample ranges from $A_V = 0.2 - 3.0$ and as expected the arc is at the extreme end of this range at $A_V = 3.24$. While the arc has a similar stellar mass to the Förster Schreiber et al. (2009) SINS sample, its stellar age appears younger and it is more heavily extincted.

Using the stellar mass and SFR derived for the arc we compute the log(sSFR), which is 0.87 Gyr^{-1}. We use the analytic fitting function from from Whitaker et al. (2012) to determine the log(sSFR) of the star-forming main sequence, which is 0.27 Gyr^{-1} for a galaxy with the same stellar mass and redshift as the arc. In Rodighiero et al. (2011), in the sample of galaxies at redshifts $1.5 < z < 2.5$, the starbursts have sSFRs that are $4\times$ the star-forming main sequence. The starburst threshold for a galaxy similar to the arc is log(sSFR) $= 0.88$ Gyr^{-1}, which means that the arc is on the star-forming main sequence.

Dynamical Mass

Figure 3.12 shows that rotation curve of the arc using the CO(1-0) emission. We use the systemic redshift from the CO(4-3) main component as the rotation center. The CO(1-0) emission from the blue component is cospatial from velocities -600 to 200 km/s, with a gap in velocity space from -300 to -200 km/s. If we ignore the blue component and only look at velocities spanning from -200 to 200 km/s we can fit an arctangent velocity function (Courteau, 1997), with Eq. 3.1, to the CO(1-0) emission.

$$V(R) = V_o + \frac{2}{\pi} V_c \, arctan \frac{R}{R_t} \tag{3.1}$$

We find that using the faint clump V4b instead of the bright clump V4a provides a better fit to the arctangent function. It also hints that the V4a clump may not be associated with the rotation of the galaxy. All the derived values hereafter are using the faint clump V4b instead of V4a.

At 3-3.5 kpc, the maximum velocity is about 140 – 150 km/s. The best fit circular velocity, using Eq. 3.1, is 202±62 km/s. In order to compare with (Förster Schreiber et al., 2009) we need to compute the dynamical mass at 10 kpc. Since the velocity curve flattens out after 3 kpc, it is safe to extrapolate the mass out 10 kpc using Eq. 3.1. At 10 kpc, the extrapolated velocity is 191±55 km s^{-1}/sin i.

The rotation curve can be used to measure the dynamical mass. The dynamical mass of a rotating disk-like galaxy is defined by Eq. 3.2,

$$M_{dyn} = \frac{RV^2}{G} \tag{3.2}$$

where $V = V_r \, sin(i)$, V_r is the rotational velocity, and i is the inclination. The inclination from the data we have is difficult to determine, so we assume $< i > = 57.3°$(Law et al., 2009). We note that the dynamical mass is inversely proportional to the inclination.

Assuming about a 10° error in the inclination, we find that the dynamical mass

is $1.2\pm0.2\times10^{11}$ $M_\odot$. Comparing the arc's dynamical mass to the SINS sample (Förster Schreiber et al., 2009) it falls in the upper mass range. About 32% of the SINS sample is in the upper dynamical mass range of $1\text{-}2\times10^{11}$ $M_\odot$.

Molecular Gas Mass and α_{CO}

In order to determine the molecular gas mass of the arc, we can use the CO(1-0) line luminosity. CO(1-0) is the standard way for determining the molecular gas mass of a galaxy. However, in order to convert from line luminosity to gas mass it is necessary to know the value of α_{CO}. α_{CO} is the conversion factor between line luminosity and molecular gas mass. It has been found locally for star form-ing galaxies, like the Milky Way, that $\alpha_{CO} \approx 4$, whereas in ULIRGs $\alpha_{CO} \approx 0.8$ (Solomon and Vanden Bout, 2005; Casey et al., 2014). There is also evidence at high redshift that galaxies undergoing large episodes of star formation may also have a α_{CO} value of 0.8 (Rawle et al., 2014; Casey et al., 2014). Without additional in-formation, one would need to assume a value of α_{CO}. Fortunately, there are two additional ways to determine a galaxies molecular gas mass (most recently shown in Spilker et al. 2015); (1) using the dust mass from the galaxy's submm emission, and (2) using the dynamical mass from the galaxy's rotation curve. By combining the methods we can constrain α_{CO} and more accurately estimate the molecular gas mass.

First we compute the molecular gas mass from the CO(1-0) luminosity using Eq. 3.3

$$M_{gas} = \alpha_{CO}L'_{CO(1-0)} \tag{3.3}$$

where α_{CO} is the conversion factor and $L'_{CO(1-0)}$ is the brightness temperature. The observed brightness temperature for the CO(1-0) line is 1.3×10^{11}(K km s^{-1} pc^2). In order to move forward we need to assume a value for α_{CO}. We use both values of α_{CO} in order to compare to other methods of finding the molecular gas mass. For α_{CO} of 0.8 and 4.0 we get a gas mass of 1.3×10^{10} $M_\odot$ and 6.5×10^{10} $M_\odot$ respectively.

In the first alternative method, which uses the dust mass, we calculate the molecular gas mass, assuming a dust-to-gas (DGR) ratio. This method uses the submm flux on the Rayleigh-Jeans side of the dust SED to estimate the dust mass. At 870 μm, the flux may be missing the warmest dust. The dust mass is defined in Eq. 3.4 (Greve et al., 2012).

$$M_{dust} = \frac{D_L^2 S_{\nu_o}}{(1+z)\kappa_{\nu_r}} [B_{\nu_r}(T_{dust}) - B_{\nu_r}(T_{CMB}(z))]^{-1} \tag{3.4}$$

where S_{ν_o} is the observed flux, B_{ν_r} is the rest-frame Planck function at the dust temperature T_{dust}. κ_{ν_r} is the rest-frame absorption coefficient defined as $\kappa_{\nu_r} = 0.45(\nu_r/250\,GHz)^{\beta}$ (Hildebrand, 1983; Kruegel and Siebenmorgen, 1994), where $\beta = 2.0$. According to Papadopoulos et al. (2000) the temperature of the CMB affects the dust mass by $\sim$2%. da Cunha et al. (2013) also found that at redshifts $z < 4$ the CMB temperature negligibly affects the dust mass and because of this we do not include it in our calculation. We find a dust mass of 1.0×10^9 $M_{\odot}$. In order to determine the gas mass, we use the relation Eq. 3.5 (Sandstrom et al., 2013)

$$\Sigma_D/DGR = \Sigma_{HI} + \Sigma_{H_2} \tag{3.5}$$

The HI gas mass is unknown, so we assume it contributes a small amount. The only other unknown is the DGR. There is evidence in local star-forming galaxies that the DGR is dependent on metallicity (Sandstrom et al., 2013). Without a metallicity measurement, we assume that the DGR is the average value of 0.0138 (Sandstrom et al., 2013), which is roughly solar metallicity. The average value has a standard deviation of 0.22 dex (Sandstrom et al., 2013). The choice in the DGR is not unreasonable as recent work by Spilker et al. (2015), a sample of dusty, star-forming galaxies from SPT with no constraint on metallicities, used the same DGR. In addition, there is evidence of dusty, star-forming galaxies at higher redshift ($z = 1.4 - 2.7$) having metallicities (8.2–8.9) similar to local star-forming galaxies Swinbank et al. (2004). We note that the DGR varies linearly with metallicity, which implies that α_{CO} is proportional to the metallicity (Leroy et al., 2011;

Sandstrom et al., 2013). With the average DGR from (Sandstrom et al., 2013), we compute a molecular gas mass of $7.4\pm1.2\times10^{10}$ $M_\odot$.

Using the second alternate method, with the dynamical mass, we can compute the molecular gas mass with Eq. 3.6

$$M_{gas} = M_{dyn} - M_* - M_{dark} \tag{3.6}$$

where the M_{dark} is the mass of the dark matter. We measure the dynamical mass in §5.2.2 and the stellar mass in §5.2.1. We note that the α_{CO} is proportional to the dynamical mass, which is inversely proportional to the inclination. We do not have enough information to determine the dark matter mass. Förster Schreiber et al. (2009) found that their sample of galaxies, at redshifts $z = 1 - 3$, had dark matter fractions of 0.2–0.3, within the radius of 10 kpc. Using this range of dark matter fractions we find a gas mass of $(1.4$–$5.6)\times10^{10}$ $M_\odot$.

Comparing the molecular gas masses, we find that the dust mass predicts a larger value than the dynamical mass. This could possibly hint that our assumption in the inclination angle could be incorrect. We find that the dust mass and dynamical mass predict a value of α_{CO}=4.6±0.7 and 2.1±1.3, respectively. This suggests that both methods are consistent with an α_{CO} value of 3–4. Since there are such large uncertainties in the dynamical mass calculation, due to the unknown inclination angle, we adopt the dust mass α_{CO} value. The α_{CO} value of the arc is similar to molecular clouds in the Milky Way, which is also $\sim$4. Genzel et al. (2015) showed that galaxies on the star-forming main sequence typically had α_{CO} values of $\sim$4. Since the arc is on the star-forming main sequence, as defined by its sSFR that we determine in §5.2.1, its α_{CO} value is not unexpected. Even though the arc has the luminosity of a ULIRG, the star-forming main sequence evolves with redshift such that more luminous IR galaxies at higher redshift on the star-forming main sequence would be considered starbursts locally (Noeske et al., 2007; Rodighiero et al., 2010a, 2011; Whitaker et al., 2012).

Computing the gas fraction, defined as $f_{gas} = M_{gas}/(M_{gas}+M_*)$, we find that f$_{gas}$ is 0.57. We can investigate the star formation efficiency, $SFE = L_{FIR}/M_{gas}$, which

is 32 $L_{\odot}$ $M_{\odot}^{-1}$. Finally we can calculate the depletion timescale $\tau_{dep} = M_{gas}/SFR$, which is ~178 Myr, similar to the other studies at $z \sim 2$ (Dekel et al., 2009; Genzel et al., 2011; Guo et al., 2012), which range from 0.1-1 Gyr.

CO Spectral Line Energy Diagram

Figure 3.13 shows the CO spectral line energy diagram (SLED) for the arc as well as several well studied dusty, star-forming galaxies and quasars. The Milky Way, Antennae galaxies and M82 are over-plotted for reference. The dusty, star-forming galaxy samples included are from Bothwell et al. (2013), SPT (Spilker et al., 2014) and the galaxies SMM J2135-0102 ("Cosmic Eyelash"; Swinbank et al., 2010; Danielson et al., 2013), and HLSJ0918+5142 (Rawle et al., 2014). The quasar samples included are the galaxies APM 0827+5255 (Egami et al., 2000) and H1413+117 ("Cloverleaf"; Bradford et al., 2009). Overall, the arc is consistent with the dusty, star-forming galaxy population, although in the lower J levels, it is also consistent with the two quasars. The dusty, star-forming population shows similar excitation as the local starburst galaxy M82. However, looking at the shape of the SLED of the arc, it resembles the Antenna galaxies, which is an interacting LIRG in the local Universe. The individual components of the arc appear different as the blue component starts to deviate for the J transitions 3 and 4. When considering the large error in the J=3 transition for the blue component, it is not significantly deviant from the total CO ratio. The J=4 transition for the blue component however appears more quasar like. The main component has a similar shape as the total, consistent with the dusty, star-forming galaxy population yet similar in shape as the Antenna galaxies. As Spilker et al. (2014) point out the quasar population deviates significantly from the dusty, star-forming galaxy population after the J=5 transition. Observations of higher order transitions are necessary to see how similar the arc is to the dusty, star-forming galaxy population and if the blue component shows excitation like a quasar.

Kennicutt-Schmidt Relation

To do a clump by clump comparison for a Kennicutt-Schmidt law, we need to determine 1-1 correspondence of the JVLA CO(1-0) emission and the SMA 870 μm dust continuum. The initial comparison of the CO(1-0) integrated image to the SMA map found that the CO clumps did not seem to correspond well with the SMA clumps. As we discussed in §3.3.2, the CO velocity projections show that multiple faint clumps are combining to appear like bright clumps in the integrated CO(1-0) image. Instead of using the integrated CO image, we use the individual velocity channels to make the comparison to the SMA 870 μm image. We find that the two brightest clumps in the individual velocity channels correspond well with the clumps in SMA 870 μm image. Clump V3 (-200 to -100 km/s velocity channel) corresponds to the SE clump, and clump V5a (0 to 100 km/s velocity channel) corresponds to the NW clump. The faint clumps from the secondary CO structure are unassociated with the major sites of star formation, seen in the SMA 870 μm image. Investigating the star forming clumps in greater detail, we find that Clump V5a is well isolated and is spatially separated from the secondary CO structure (Figure 3.7). However, clump V3 may have contamination from the secondary structure, identified in §3.3.2. Clump V3 is where the bright clumps (main structure), which are part of the rotating disk, appear to merge with the faint clumps (secondary structure). To add more complication, the SMA continuum from the SE clump seems to also match with clump V1 (-400 to -300 km/s velocity channel). This is indicative that both clumps V1 and V3 are contributing to the dust continuum emission in SE SMA clump. We suspect that higher resolution continuum imaging from ALMA will be able to put a stronger constraint on how much star formation each clump is undergoing. For the time being, we assume that all the star formation is in clump V3.

Figure 3.14 shows the mismatch between the clumps in the SMA 870 μm image (left panel) and the integrated CO(1-0) image (middle panel). If we only combine the CO(1-0) channels that appear to match the SMA map, which would be channels 1, 3, and 5 (Figure 3.7), we would construct the image in the right panel of Figure 3.14. Over-plotted in all the panels are the SMA 870 μm contours for comparison.

When combining the CO from channels 1, 3 and 5, the morphology and intensity look almost identical to the SMA 870 μm image. This strongly suggests that CO detected in the other channels is unassociated with the star formation in the arc.

Now that we have identified the clumps associated with star formation we can calculate the star formation surface density and molecular gas surface density. In order to compute the star formation surface density and molecular gas surface density, we need to know the area for each of the clumps. The lens configuration of the system only provides high spatial resolution in one direction, in which the arc and clumps are resolved. However, the tangential direction to the arc is unresolved, which makes it difficult to know precisely the size of all the features. To proceed, we assume that the sizes of the unresolved dimension are the same as the resolved dimension.

Figure 3.15 shows the Kennicutt-Schmidt relation. Galaxies with redshifts $1 < z < 4$ are plotted from the Genzel et al. (2010) and Tacconi et al. (2013) samples. The arc is plotted with the total integrated gas surface density and star formation surface density. In addition, the two SMA clumps, NW and SE, are plotted (with the corresponding CO clumps V5a and V3). We find that the arc as a whole has an average star formation surface density and molecular gas surface density when comparing to the Genzel et al. (2010) and Tacconi et al. (2013) samples. The clumps on the other hand exhibit much higher star formation surface densities than the entire arc and yet the molecular gas surface densities are about the same.

It is interesting to note how different the gas consumption timescales are in the arc, which is $\sim$800 Myr, and in the clumps which are $\sim$50 Myr. A large fraction of the gas is in the star forming clumps and the arc's gas consumption timescale is diluted by the area of the arc. We benefit from the gravitational lensing by being able to resolve the individual star forming regions, which allows the determination of the area. In unresolved studies, the area is taken from the entire galaxy and it is likely that a large fraction of the gas resides in the star forming regions. This implies that the star formation rate surface densities may be larger in unresolved galaxies.

Interpretation of the CO structures

• *A Possible CO Outflow*

In §3.3.2 we identify several faint clumps that are in the same spatial position spanning large range of velocities (ΔV =300 km/s). Possible explanations to this are a spiral arm or a wind (with outflowing material).

In the simple case of a single spiral arm, you would expect to see a component's spatial position change through each velocity channel. These components would all appear to rotate like a disk. You would not see a CO component span such a large velocity range in the same spatial position, especially ΔV =300 km/s. It is unlikely that the faint clumps are part of a spiral arm.

In the wind case, you might expect to see a range of velocities in the same spatial position, which we observe. However, one concern of this scenario is the inclination of the galaxy. While the inclination is uncertain, it would be expected that if you had a powerful wind being fueled by star formation or an AGN, it would appear something like M82, where the material being thrown out of the galaxy would be perpendicular to the rotation of the galaxy. In the case of the arc, it appears that the "outflowing" CO is sitting on top of the rotating disk. It could be that the galaxy's inclination is close to face-on and then we might see the material appearing to be on top of and below the galaxy spatially.

From the line profiles of CO(1-0), CO(3-2) and CO(4-3), as we discussed in §3.2, we identify two components; a narrow bright component (main component) and a broad fainter component (blue component). If we extract the CO(1-0) spectrum at the position of the faint clumps (swapping V4b for V4a, as we discuss in §5.2.2) we would essentially recreate the broad component we see in all of the line profiles. Interestingly, if we include clump V1 (which is within $2''$ of the faint clumps), it also appears to be part of the blue component. Without information about the galaxy's inclination, we might interpret the broad faint wing as outflowing material. This further supports the outflow hypothesis. While the likely solution for the secondary structure appears to be an outflow, the inclination adds uncertainty and confusion to this interpretation. Even with a slight inclination, it would be expected to see the

outflowing material spatially offset from the rotating material.

- *A Minor Merger at the SE Edge of the Arc*

In the CO velocity slices (Figure 3.7) we identify a clump (V1) in the velocity bin -400 to -300 km/s. Clump V1 is spatially offset from the next clump (V3) and kinematically offset by 100 km/s (from the gap in panel 2 in Figure 3.7). One possible explanation is that clump V1 is another galaxy interacting with the arc. The gap seen in the velocity slices is strongly suggestive that this is a separate system. In addition, when including clump V1 into the rotation curve, the clump does not appear to be associated with the main galaxy's rotation. Another interesting aspect is that the spatial positions of clump V1 and V3 coincide with the peak of the SMA continuum emission as well as bright spot in the near-IR images. It is possible that a merger induced star formation episode is producing the bright SE SMA clump. Perhaps the rotation curve is still intact due of the mass ratio of the galaxies interacting. If we use gas mass as a proxy for total mass, by comparing the ratios of the masses between the clump V1 and the arc, we would get a ratio of ~1:10, which would be considered a minor merger.

3.5.3 $L_{[CII]}$-L_{FIR} Relation

Figure 3.16 shows the relation between [CII] luminosity and far-IR luminosity. For local galaxies, $z < 0.5$ (Malhotra et al., 2001; Sargsyan et al., 2012), [CII] becomes less luminous (or suppressed) as far-IR luminosity increases. At $z = 1 - 4$ the situation is different, empirically [CII] remains luminous regardless of L_{FIR} (Stacey et al., 2010; Valtchanov et al., 2011). The larger luminosity of [CII] could be the result of larger regions containing greater amounts of [CII]. The $L_{[CII]}/L_{FIR}$ ratio of $z = 1-4$ galaxies is similar to lower luminosity local galaxies ($< 10^{11}$ $L_\odot$). The arc appears to have a similar $L_{[CII]}/L_{FIR}$ ratio as Stacey et al. (2010), Valtchanov et al. (2011) samples at lower L_{FIR}. As we go to higher redshifts, $z > 4$, there is some evidence for [CII] suppression (Cox et al., 2011; De Breuck et al., 2011; Swinbank et al., 2012; Venemans et al., 2012; Wagg et al., 2012; Riechers et al., 2013; Rawle et al., 2014) relative to the $z = 1-4$ population, yet it is not nearly as much as seen in local galax-

ies. The suppression of [CII] could be an indication of AGN. The triplet ($z = 4.68$) has a similar $L_{[CII]}/L_{FIR}$ ratio as galaxies at $z > 4$. Rawle et al. (2014) reports that the Ra component in HLSJ0918 shows evidence of containing an AGN, which is in a similar region in the $L_{[CII]}$-L_{FIR} plot as the triplet. The other components (VB, Rb and B) of HLSJ0918 have less [CII] suppression than the Ra component.

3.6   Conclusions

One of the brightest sources in HLS, we find that HLSJ2043 is a blend of two galaxies, one at $z = 2.041$ and the other at $z = 4.68$. Using the redshift and positions of the cluster members and the redshift of the triplet, we are able to construct an accurate lens model that enables us to determine the intrinsic properties of each of the background galaxies. We find that the arc is a singly imaged galaxy with a magnification of $7.87\times$, and the triplet is a triply imaged galaxy with a total magnification of $17.55\times$.

Using MCMC and the ratio of the fluxes of the triplet, we are able to separate the blended far-IR/submm fluxes of the arc ($z = 2.041$) and the triplet ($z = 4.68$). We find that the arc and the triplet are ULIRGs. The SED of the arc is what is expected for a more typical luminosity galaxy at $z \sim 2$. The triplet has a more unusual SED, which may be the result of MCMC fitting and underestimate of the errors. With the detection of the redshift $z = 4.68$ galaxy in *Herschel*/PACS it would be expected to have a warm dust component which is suggestive it may contain an AGN.

The analysis of the arc suggests that the clumps found in the integrated CO(1-0) map do not correspond to the clumps in the SMA continuum map. By investigating the individual velocity slices we were able to match the SMA clumps to the CO(1-0) clumps. The integrated map is the result of two CO structures, one with bright clumps rotating like a disk and a second structure of fainter clumps which all fall in the same spatial position.

From the CO(1-0) line luminosity, dynamical mass and dust mass we are able to put constraints on α_{CO} and the molecular gas mass in the arc. We find that α_{CO} agrees with a value of 4, which is similar to molecular clouds in the Milky Way. Local

ULIRGs typically have α_{CO} values $\sim$0.8. However, there is redshift evolution of the star-forming main sequence and the arc's sSFR places it on the main sequence at $z = 2.0$. Genzel et al. (2015) found that galaxies on the star-forming main sequence have α_{CO} values ~ 4.

Using α_{CO}, we compare the arc on a Kennicutt-Schmidt relation, in which it appears average compared to other samples of galaxies at redshifts $z = 1 - 3$. However, when comparing the clumps, they have much larger star formation surface densities than the total amount in the arc, with a shorter gas consumption timescale of about 50 Myr. This appears to be an effect of resolution as the higher spatial resolution provided by gravitational lensing allows a more accurate measurement of the size of the star forming regions within the arc. Studies of unresolved galaxies may be underestimating the star formation surface densities and gas consumption timescales.

We find that CO structure in the arc is quite complicated. One of the structures is consistent with a rotating disk, while the other structure appears to be a CO outflow. The spatial position of the "wind" is a bit confusing as it almost implies that the galaxy is near face-on. In addition, at the SE edge of the arc there is some evidence that it is undergoing a minor merger. We identify two CO clumps, with a 100 km/s gap in velocity space, that are spatially associated with the brightest SMA emission at the SE edge of the arc. This evidence suggests that the SE edge of the arc could be undergoing merger induced star formation. Higher resolution optical/near-IR images with *HST* and submm imaging with ALMA are necessary to test these scenarios.

When comparing $L_{[CII]}/L_{FIR}$ ratio, we find that the arc is similar to other $z \sim 2$ galaxies, at a lower luminosity. The trend at $z \sim 2$ is with much higher $L_{[CII]}$ with no signs of suppression where the local samples at similar luminosity appear suppressed. Going to higher redshift the trend appears to reverse with sources $z > 4$ show slightly weaker $L_{[CII]}$ The triplet appears similar to other galaxies at $z > 4$ showing some suppression. This could be evidence of AGN activity, which we already suspect based on the far-IR SED.

Table 3.1.   Unresolved Photometry of the Bright Herschel Source

Band	HLSJ2043 Flux [mJy]
Spitzer/MIPS 24 μm	2.54±0.05
Herschel/PACS 100 μm	34±10
Herschel/PACS 160 μm	150±10
Herschel/SPIRE 250 μm	185±22
Herschel/SPIRE 350 μm	286±22
Herschel/SPIRE 500 μm	274±18
JCMT/SCUBA-2 850 μm	66±5
CSO/Bolocam 1.1 mm	47.5±4.2
LMT/AzTEC 1.1 mm	29±3
GISMO 2 mm	6±1

Table 3.2.   SMA Clump Properties

ID	S/N[a]
SE	15.4
NW	9.5

Table 3.3.   Photometry of the Bright Herschel/SMA Sources

Band	HLSJ2043-arc Magnitude [AB]	HLSJ2043-A Magnitude [AB]	HLSJ2043-B Magnitude [AB]	HLSJ2043-C Magnitude [AB]
UKIRT/WFCAM J	20.75±0.09	<21.88	<20.44	<21.75
UKIRT/WFCAM Ks	19.30±0.05	<22.25	<20.65	<22.71
Spitzer/IRAC [3.6]	17.54±0.17	⋯	⋯	⋯
Spitzer/IRAC [4.5]	16.93±0.13	⋯	⋯	⋯
Band	Flux [mJy]	Flux [mJy]	Flux [mJy]	Flux [mJy]
SMA 870 μm	46±7.6	7.8±0.9	4.4±0.8	7.3±1.0

Table 3.4.   CO(1-0) Integrated Clump Properties

ID	S/N[a]
C1	5.6
C2	7.8
C3	5.6
C4	4.4

Table 3.5. CO(1-0) Velocity Bin Clump Properties

ID	S/N[a]	Velocity bin [km s^{-1}]
V1	6.3	-350
V3	8.0	-150
V4a	7.3	-50
V4b	5.9	-50
V5a	9.6	50
V5b	5.2	50
V6a	5.3	150
V6b	4.8	150

Note. — [a] S/N is peak flux of clump compared to the RMS of the map.

Table 3.6.   Measured atomic and molecular lines

Line	Component	ν_{obs} [GHz]	ΔV_{FWHM} [km s^{-1}]	V [km s^{-1}]	I [Jy km s^{-1}]
[CII]	**Total**	624.966	<690	0	**172±26**
^{12}CO(1-0)	main	37.908	240	-20	0.6±0.1
	blue	37.936	630	-240	0.8±0.2
	Total	⋯	⋯	⋯	**1.3±0.3**
^{12}CO(2-1)^{a}	**Total**	75.827	530	⋯	**6.1±0.9**
^{12}CO(3-2)	main	113.730	250	-50	8.6±2.3
	blue	113.852	510	-370	6.6±2.6
	Total	⋯	⋯	⋯	**15.1±4.9**
^{12}CO(4-3)	main	151.608	200	0	5.7±0.9
	blue	151.780	550	-340	5.6±1.1
	Total	⋯	⋯	⋯	**11.3±2.0**

Note. — [a] Measurement is from Zavala et al. (2015)
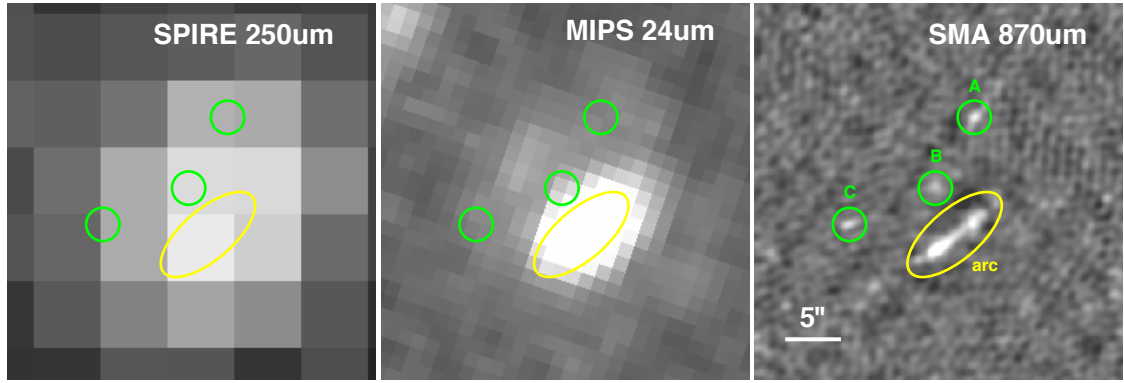
Figure 3.1: Far-IR/submm images of the HLS bright source HLSJ2043. The high resolution SMA 870 μm image reveals that the SPIRE detected source HLSJ2043 is a blend of 4 sources; an arc at redshift $z = 2.041$ (marked by the yellow ellipse) and a triply imaged galaxy at redshift $z = 4.68$ (marked by the green circles). The *Spitzer*/MIPS image only shows the arc; the triply image galaxy is undetected.
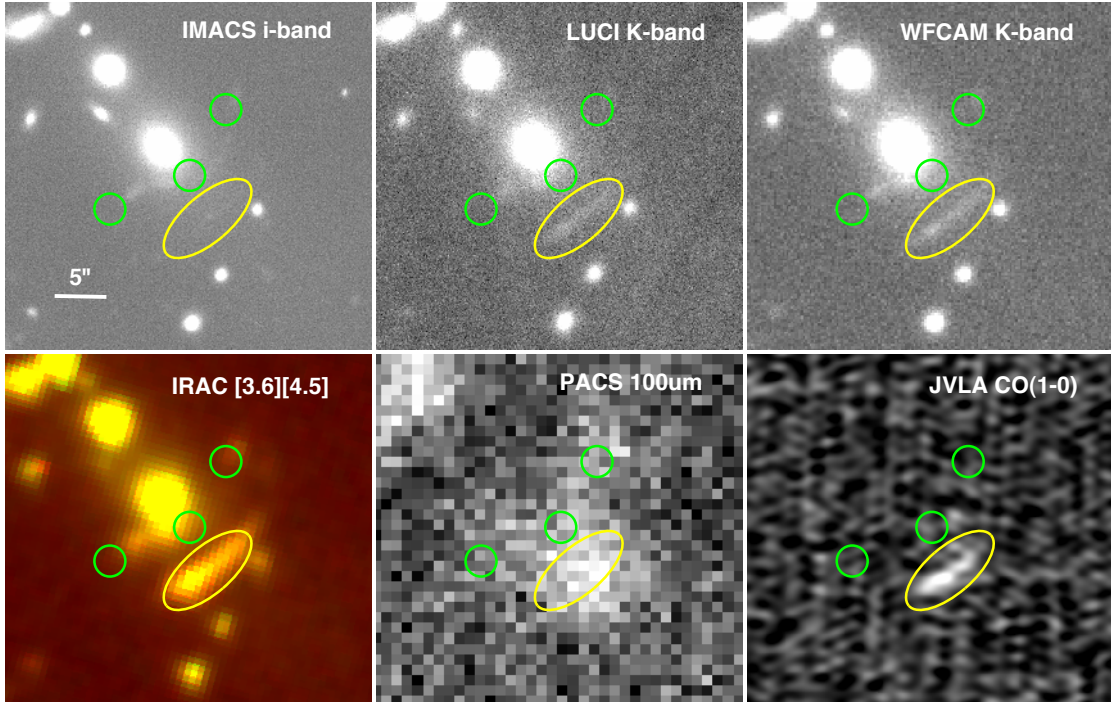
Figure 3.2: Multi-band image of the cluster core of RXCJ2043. The yellow ellipse marks the position of the singly imaged galaxy at redshift $z = 2.041$ and the green circles mark multiply imaged galaxy at redshift $z = 4.68$ presented in Zavala et al. (2015). The arc is clearly detected in the near-IR yet undetected in the optical. The $z = 4.68$ triply imaged source is only seen in the far-IR/submm images (PACS, SPIRE and SMA).
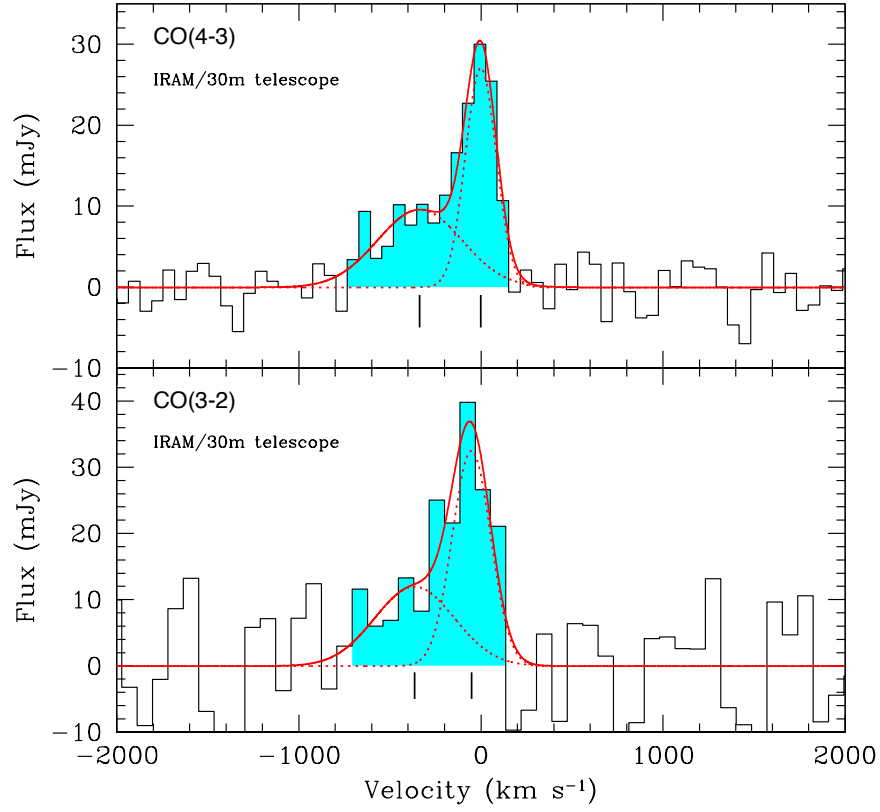
Figure 3.3: IRAM/30m detection of CO(4-3) in the upper panel and CO(3-2) in the bottom panel. The red lines shows the Gaussian fit to the CO(1-0) emission. The dashed red lines shows individual fits to the each of the components (main and blue). All the CO transitions show a main and blue component. The CO(4-3) transition clearly shows that the blue component is quite broad FWHM$\sim$500 km/s.
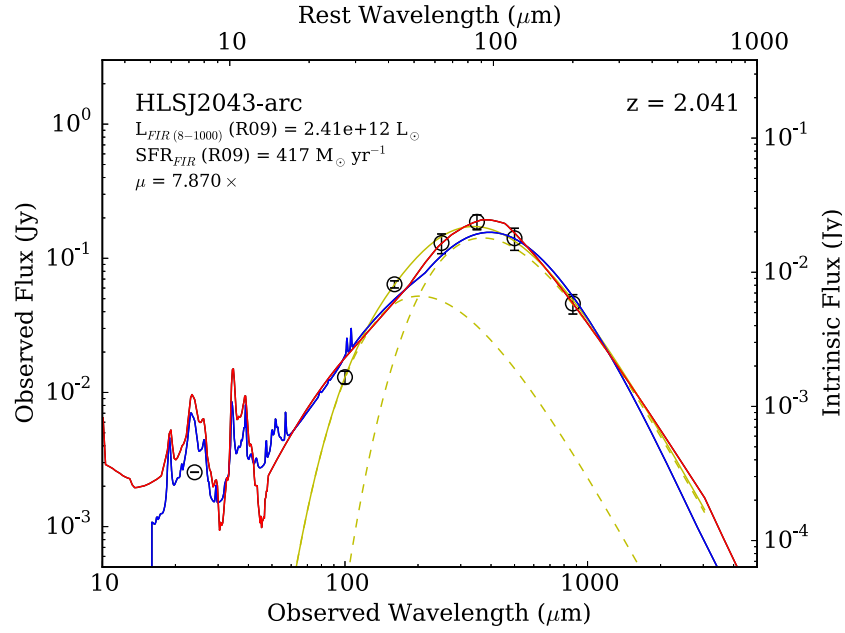
Figure 3.4: SED of the arc which includes photometry from *Spitzer*/MIPS 24 μm, *Herschel*/PACS and SPIRE (100-500 μm) and SMA 870 μm. The blue line is the best fitting scaled Rieke et al. (2009) template with an intrinsic integrated luminosity of 2.4×10^{12} L$_\odot$. The red line is the best fitting Chary and Elbaz (2001) template with an intrinsic integrated luminosity of 2.7×10^{12} L$_\odot$. The yellow line is the best two temperature component modified black black fit to the photometry. The dashed yellow lines represents each temperature component used to fit the photometry, with the main dust component at 26 ± 3 K and warmer component at 48 ± 6 K.
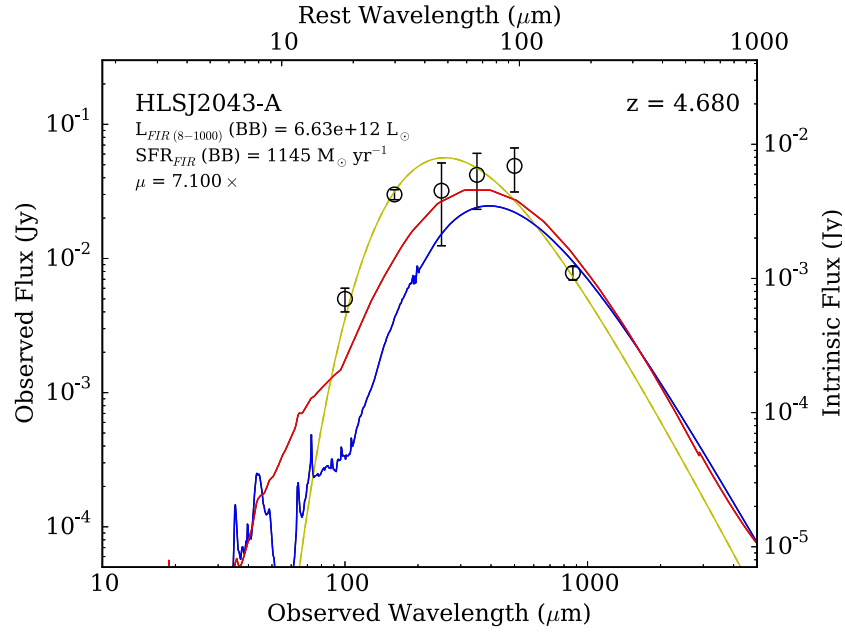
Figure 3.5: SED of image A of the triplet which includes photometry from *Herschel*/PACS and SPIRE (100-500 μm) and SMA 870 μm. Line description is same as Figure 3.4. The Rieke et al. (2009) and Chary and Elbaz (2001) templates have a hard time fitting the unusual SED. There appears to be a warmer dust component that is not in the local templates. While the modified blackbody fit is consistent with the photometry, it is unphysical at 71$\pm$2 K. We use the modified blackbody to estimate the luminosity of the galaxy.
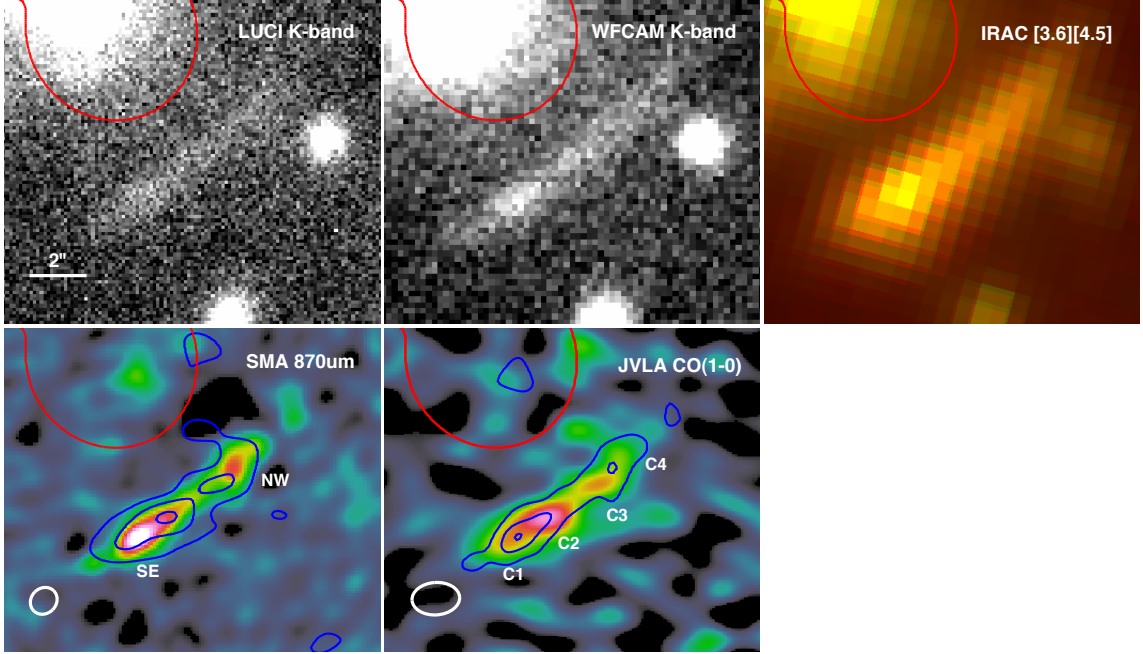
Figure 3.6: Zoom-in of the arc in RXCJ2043. The peak IRAC [3.6] and [4.5] emission corresponds with the peak near-IR emission (LUCI K-band and WFCAM K-band), SMA continuum emission, and CO(1-0) emission. There are two distinct clumps seen in the SMA image (SE and NW) and four clumps seen in the integrated JVLA image (C1, C2, C3, and C4). In the SMA map, the blue contour overlay is from the integrated JVLA CO(1-0). In the JVLA integrated image, the blue contours overlay is from SMA 870 μm image. The bottom contour level is at 3σ of the RMS in each image, and each of the contours are spaced by 2σ. The red line in each panel shows where the $z = 2.041$ critical line is located. The beam size is shown the in bottom left corners of SMA and JVLA images.
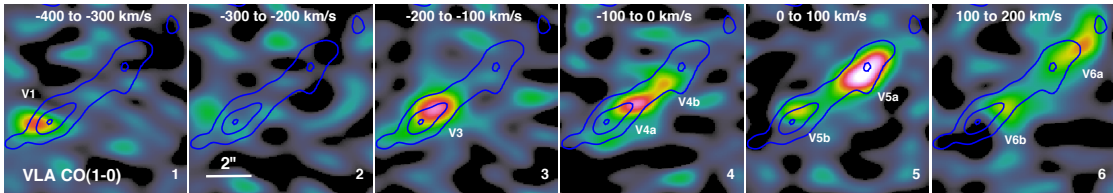
Figure 3.7: JVLA CO(1-0) maps of the arc at redshift $z = 2.041$. Each image shows velocity slice of the CO(1-0) emission. Rotation is clearly seen by following the brightest clumps, moving from the left to right panels. The contour overlay is from the SMA 870 μm image. The majority of the CO(1-0) emission appears in the lower right portion of the arc, spanning multiple velocity bins (-400 to 100 km/s). Each of the individual clumps in the velocity slices are labeled.
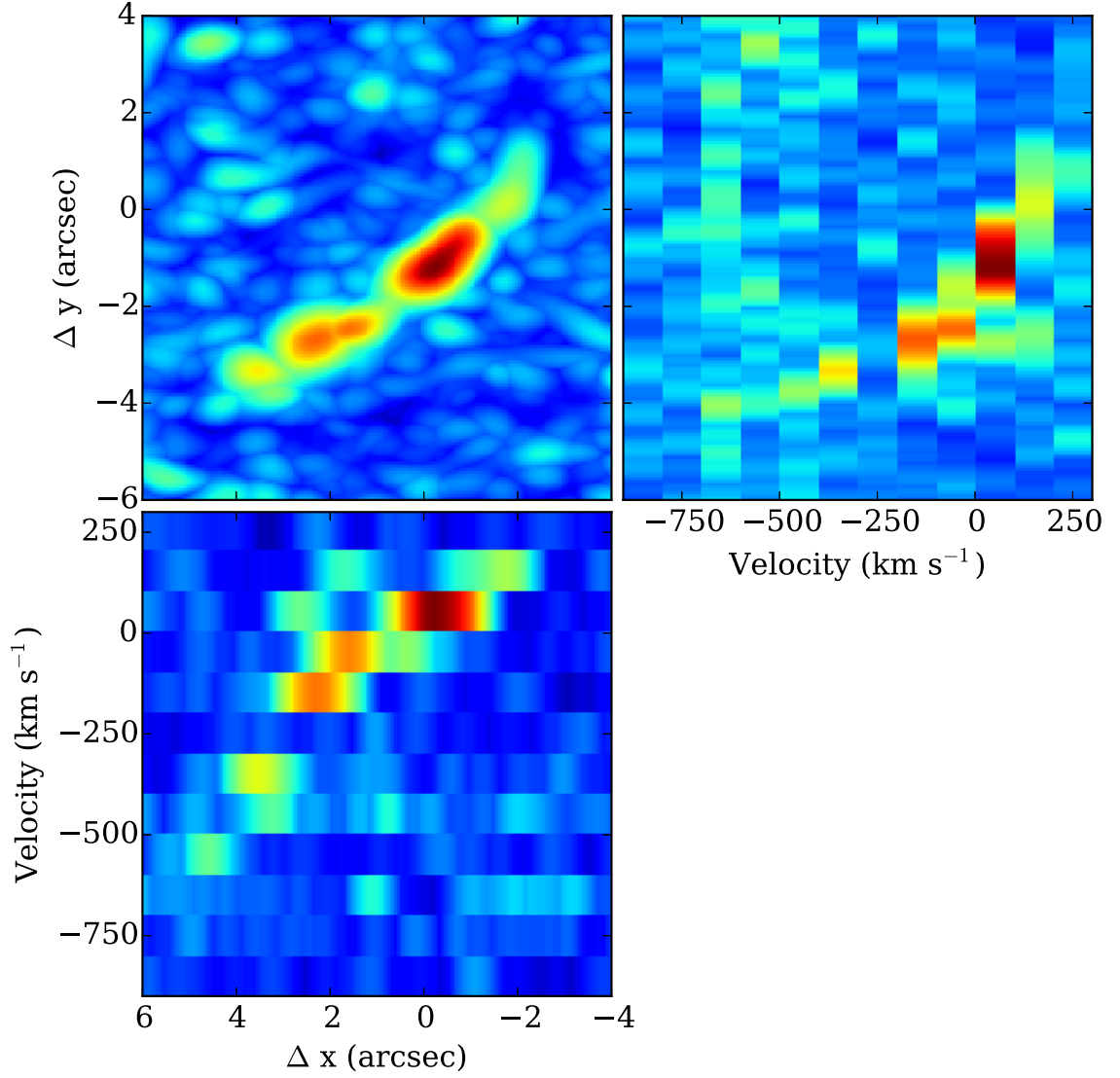
Figure 3.8: Projections of the JVLA CO(1-0) in; velocity (top left panel), x-axis (RA, bottom left panel) and y-axis (Dec, top right panel). The maximum value is shown through a given line-of-sight. The projections in RA and Dec show two CO structures; a bright main structure and a faint secondary structure. The bright structure appears to have rotation, whereas the secondary structure is at the same spatial location spanning 300 km/s. A gap in velocity space is also prominently seen in the velocity channel -200 to -300 km/s.
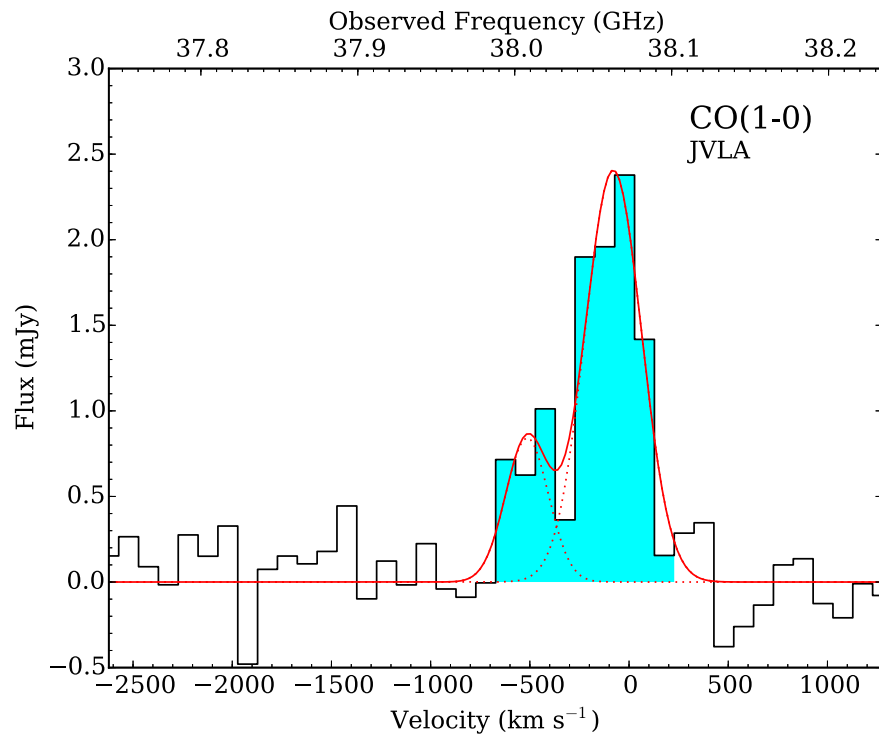
Figure 3.9: JVLA detection of CO(1-0) in the arc. Line description is same as Figure 3.3. The CO(1-0) emission also shows a main and blue component.
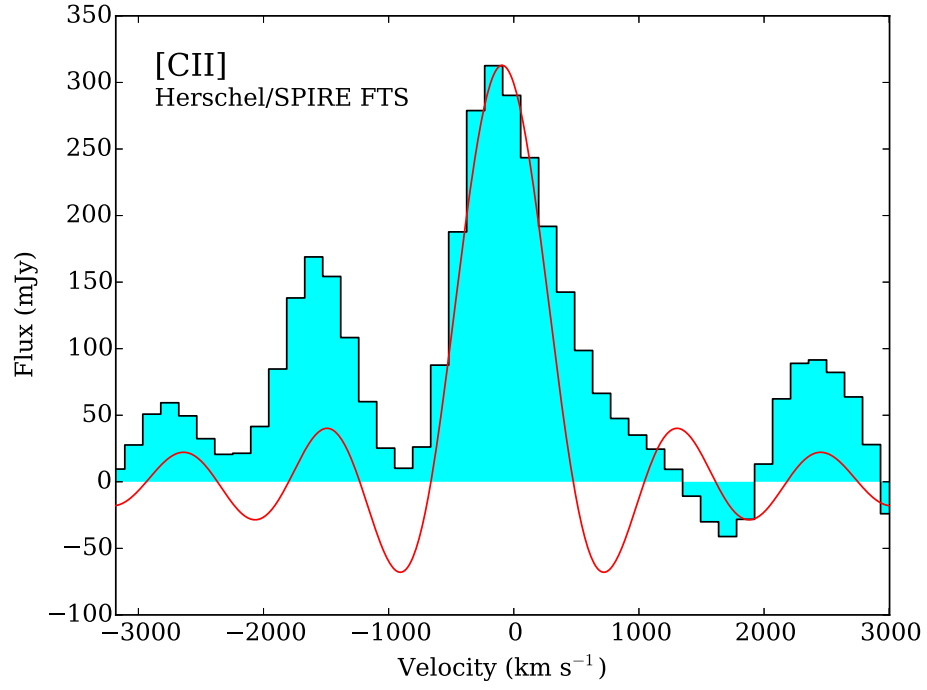
Figure 3.10: The SPIRE/FTS detection of the [CII] 158 μm line in the $z = 2.041$ arc. The red line is the fit to the [CII] line using sinc function.
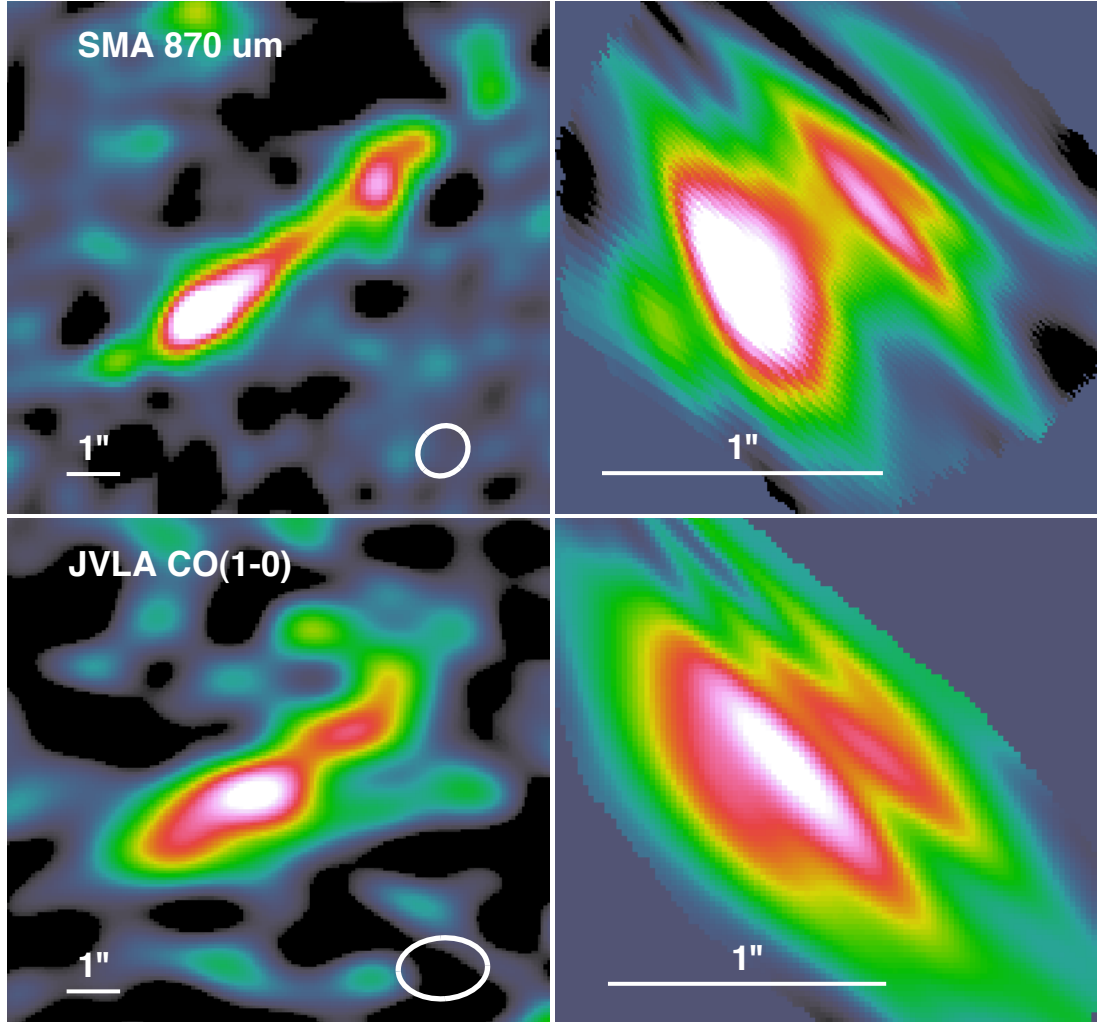
Figure 3.11: The images on the left are actual observations of the arc in the image plane, the images on the right are the source plane reconstructions of the observations. Top left panel: SMA 870 μm image of the arc. Two clumps are clearly seen in the image. The beam size is represented in the right corner (FWHM = $1.00''\times0.88''$). Top right panel: The source plane reconstruction of the SMA 870 μm image. The image is stretched along the arc, which has the highest spatial resolution. Bottom left panel: JVLA CO(1-0) integrated image. The beam size is represented in the bottom right corner (FWHM = $1.68''\times1.14''$). There appears to be 4 clumps in the image, though based on the S/N, only 3 of them may be real. The bright large SE clump appears to resolved with the JVLA beam. Bottom right panel: The source plane reconstruction of the JVLA CO(1-0) image. The bright SE clump is being probed at high spatial resolution, benefiting from the stretching provided by the gravitational lensing.
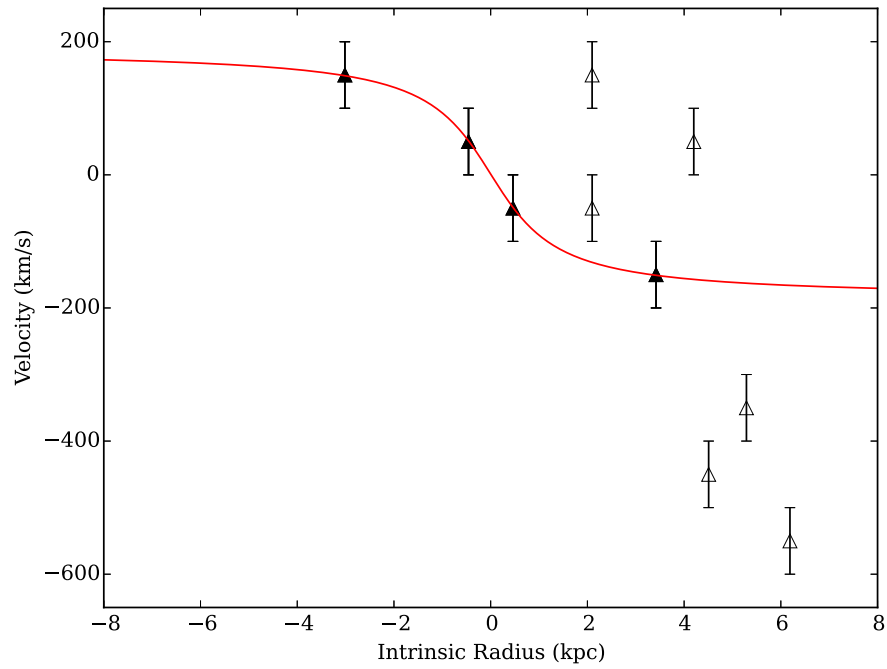
Figure 3.12: Rotation curve of CO(1-0) measured in the arc. The solid triangles are the CO clumps used to measure the rotational velocity. The open triangles are detected clumps without any ordered rotation, which spatially appear to part a secondary component found at the SE edge of the arc. They are not included in the fit. The secondary component spans $\Delta V = 600$ km/s. The red line is the arctangent function fit to the solid triangles.
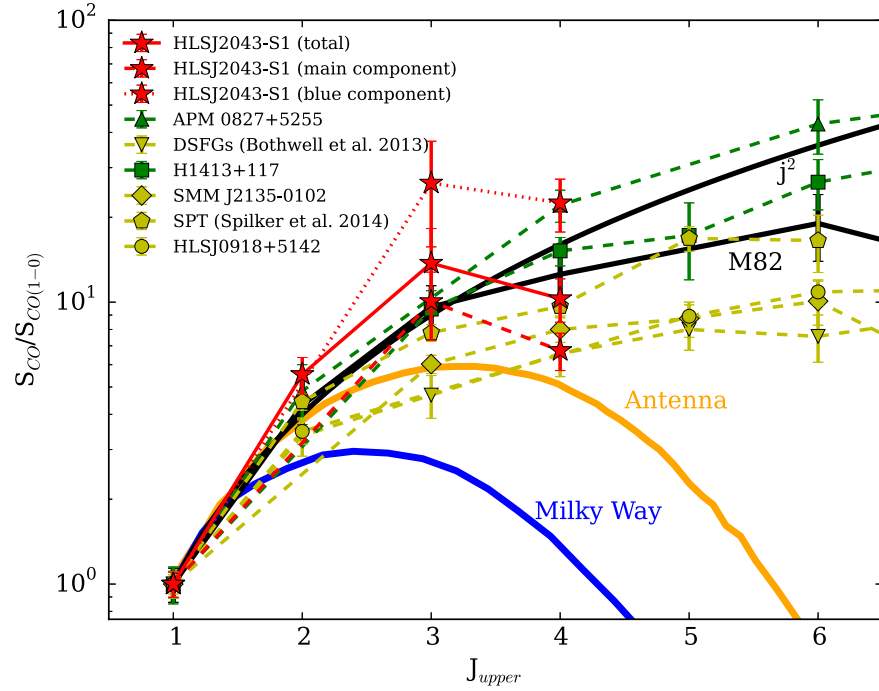
Figure 3.13: Spectral line energy diagram (SLED) for the arc, shown with the red lines. The solid red line is the total CO for the system, the dashed red line is the main component, and the dotted red line is the blue component. Over-plotted are local galaxies Milky Way, Antenna and M82. Yellow dashed lines are sample of SMGs (Bothwell et al., 2013; Danielson et al., 2013; Rawle et al., 2014; Spilker et al., 2014). The green dashed lines are a sample of QSOs (Egami et al., 2000; Bradford et al., 2009). The black solid line is j^2 excitation.
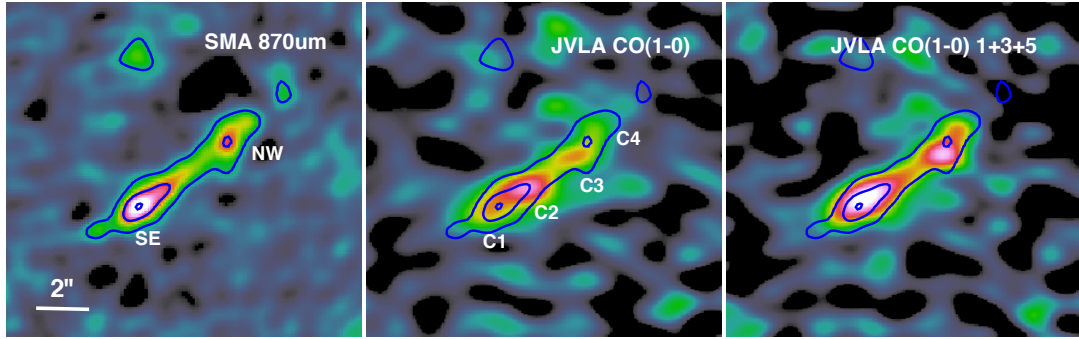
Figure 3.14: Left panel: SMA 870 μm image with SMA contours. The two prominent clumps are are labeled. Middle panel: JVLA CO(1-0) integrated image with SMA contours. The four JVLA clumps are labeled. The mismatch between the SMA clumps and JVLA clumps can be clearly seen. Right panel: JVLA CO(1-0) with the velocity channels 1, 3, and 5 combined with SMA contours. When only the velocity channels 1, 3 and 5 (from Figure 3.7) are combined, the SMA 870 μm map corresponds well with the JVLA CO(1-0). This strongly suggests that the other CO is unassociated with star formation.
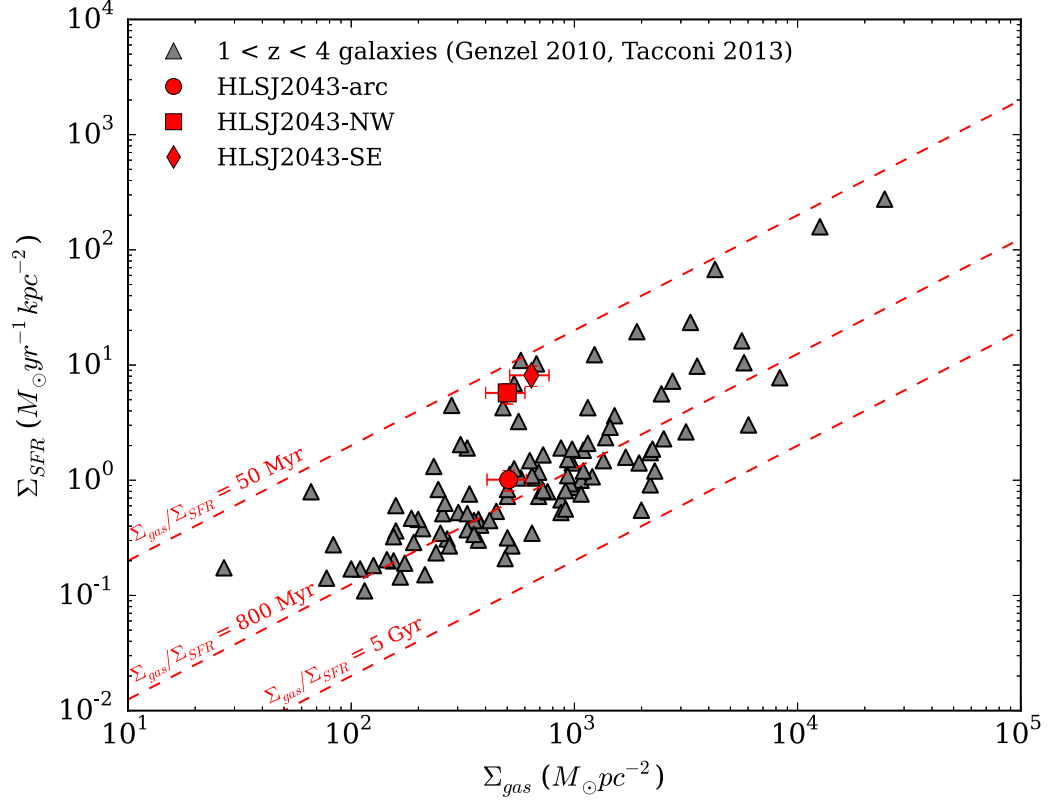
Figure 3.15: Kennicutt-Schmidt relation showing the star formation surface density as a function of gas surface density. Genzel et al. (2010) and Tacconi et al. (2013) samples are plotted for comparison. The entire arc of HLSJ2043 is plotted as well as the two star forming clumps identified in the SMA 870 μm data (NW and SE). The arc appears similar to the other galaxies over-plotted. The two clumps appear strikingly different than the arc, partly from the resolution gained from the gravitational lensing and partly from the CO unassociated with star formation.
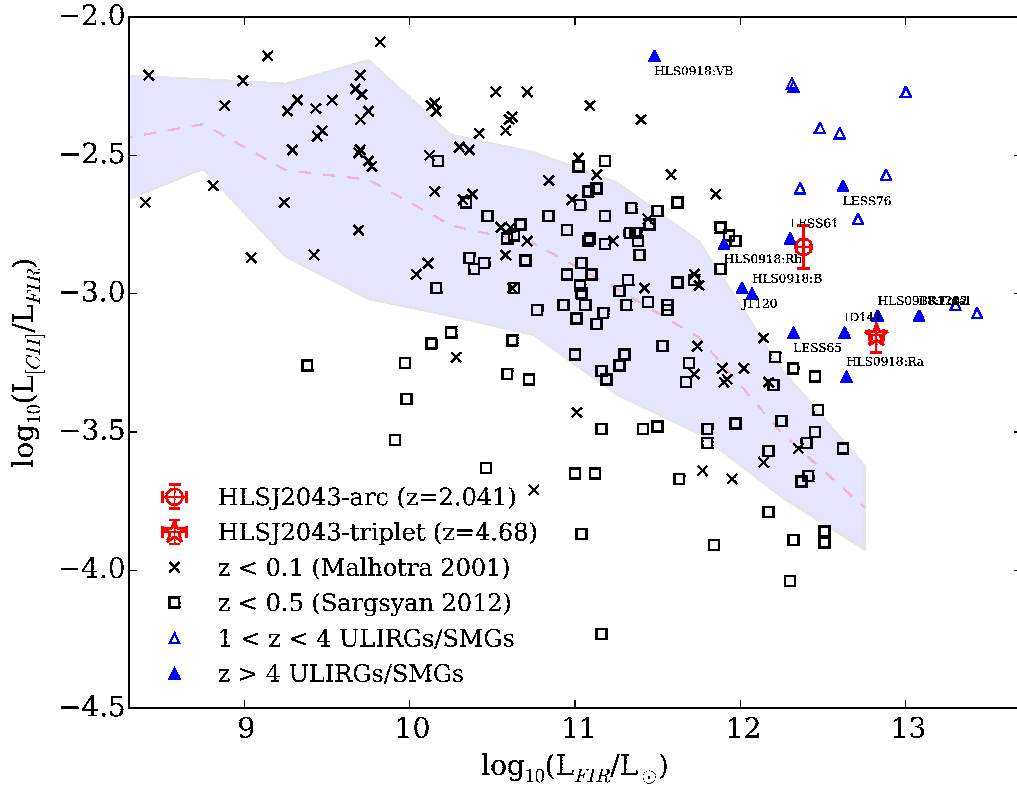
Figure 3.16: $L_{[CII]}$-L_{FIR} relation. The blue shaded region shows the $\pm 1\sigma$ range of local galaxies at redshifts $z < 0.5$ (Malhotra et al., 2001; Sargsyan et al., 2012). The higher luminosity local galaxies show [CII] suppression. Galaxies at redshift $z = 1 - 4$ (Stacey et al., 2010; Valtchanov et al., 2011) show [CII] is more luminous than the local galaxies. $z > 4$ galaxies (Cox et al., 2011; De Breuck et al., 2011; Swinbank et al., 2012; Venemans et al., 2012; Wagg et al., 2012; Riechers et al., 2013; Rawle et al., 2014) show some suppression of [CII] but overall are still more luminous than local galaxies. The arc resembles the $z = 1 - 4$ population and the triplet resembles $z > 4$ population. Large suppression of [CII] is thought to be an indication of AGN.

CHAPTER 4

The Rest-frame Optical Spectra of *Herschel* Selected Gravitationally Lensed Dusty, Star-Forming Galaxies†

We report on the near-IR spectroscopic observations of 12 luminous gravitationally lensed dusty, star-forming galaxies at redshifts $z = 1-4$ in the fields of 10 massive galaxy clusters. These bright sources are selected with *Herschel* from the *Herschel* Lensing Survey, with a peak flux density of $S_{peak} > 100$ mJy and a *Herschel*/SPIRE flux ratio of $S_{500}/S_{250} > 0.4$ which implies that they are all gravitationally lensed and at redshifts $z > 1$. From their flux densities, these sources all have observed luminosities $> 10^{13}$ $L_\odot$ and it is anticipated that their inferred rest-frame optical nebular emission lines are easily accessible with current ground based telescopes, even with large dust attenuations. If we assume a magnification factor of $10\times$, these sources would all have intrinsic luminosities that are at the LIRG/ULIRG threshold. From our sample, we detect nebular emission lines in 9 of the 12 galaxies targeted, which include Balmer lines (Hα and Hβ) and forbidden lines ([NII] and [OIII]). When comparing the star formation rates derived from both the far-IR and Balmer emission lines (from Hα or Hβ), we find that the Balmer lines under-predict the star formation rates by a median factor of $30\times$, larger than previously reported in the literature. This implies that these galaxies are all heavily dust obscured. We find

that the median dust attenuation for this sample is $A_V = 3.7 \pm 1.5$. One of the sources in particular is a significant outlier in the sample with Hα under-predicting the far-IR derived star formation rate by a factor of $550\times$. The [NII]/Hα line ratio of this galaxy suggests it contains an AGN. Other AGN diagnostics, such as velocity dispersion of the Hα and the best fitting template luminosity to the photometry suggest otherwise. This is suggestive that this galaxy only possibly contains a weak AGN and the majority of the far-IR/submm emission is caused by star formation.

4.1   Introduction

Very little is known about the rest-frame UV and optical emission of dusty, star-forming galaxies at high redshift ($z > 1$). Dusty, star-forming galaxies are typically selected in the far-IR/submm and most ISM studies focus on the molecular gas and dust. While molecular gas and dust play an important role in how star formation is fueled and where the star formation is occurring, the perspective is limited. However, by probing the rest-frame UV and optical emission, we will get the complete picture of star formation, by studying the nebular emission. The nebular emission provides a more instantaneous star formation rate indicator as well other physical properties which can tell us more about the stars living in these galaxies.

Targeting dusty, star-forming galaxies in their rest-frame UV is challenging. In Casey et al. (2012b,a), using Keck/LRIS for a *Herschel* selected sample, they were only able to detect emission from 268 galaxies out of 664 (40%) in the optical. From their 268 detections, only 36 (5%) were at redshifts $z > 2$, (e.g. detecting emission lines such as Lyα, [C IV], and [Si IV]). In addition, the majority of these sources have luminosities $> 5 \times 10^{12}$ $L_\odot$. UV studies may also be problematic in that emission lines will be more heavily affected by dust than the stellar continuum. This means in many cases it may not be possible to detect emission lines, requiring surveys to go to lower flux densities in order to detect the continuum. This is not unexpected as the dust more severely attenuates the UV light, especially for dusty galaxies. There is also the potential for sample bias; by targeting the rest-frame UV for follow-up you may bias your sample to luminous galaxies that may appear no different than

Lyman α emitters or Lyman break galaxies. Instead, going after rest-frame optical emission might be more promising since Balmer lines, such as Hα and Hβ, are not as affected by dust attenuation as the UV. From the inferred star formation rates, the Balmer emission will be quite bright enabling easy follow-up of such sources.

The rest-frame optical provides an ample amount of information about the physical properties of a galaxy. Nebular emission lines specifically reveal; instantaneous star formation (Hα, Hβ, [OII]) (Kennicutt, 1998; Kewley et al., 2004), ionization ([OIII]/[OII]), metallicity (R23, N2, O3HB) (Kewley and Ellison, 2008; Pettini and Pagel, 2004; Maiolino et al., 2008) and whether the galaxy contains an AGN (Kewley et al., 2001; Kauffmann et al., 2003; Juneau et al., 2011). Some of these properties require the detection of sets of emission lines, which can also be challenging for dusty, star-forming galaxies.

A rest-frame optical study by Swinbank et al. (2004) looked at a sample of ultra-luminous SCUBA selected galaxies at redshifts $z = 1.4 - 2.7$. While they were a mix of star forming galaxies and AGN, they all showed less luminous Hα emission (suppression) than what was predicted from the far-IR/submm inferred star formation rates. For their sample, the median suppression of Hα was a factor of $10\times$, which could be attributed to dust. Since these are the galaxies with the most star formation in the Universe, it is not unexpected that they would generate a lot of dust, as has been seen locally. However, the expectation is that the dust attenuation is smaller in lower luminosity galaxies.

More recent near-IR surveys now either use a sample selection from UV (Steidel et al., 2014) or rest-frame optical (Shapley et al., 2015) to target typical star forming galaxies. While these samples are providing a wealth of information about star forming galaxies, their selection is biased against dusty, star-forming galaxies. Due to their large dust attenuations, dusty galaxies drop out of these selections and those that are detected are atypical. In order to have an unbiased sample selection of dusty, star-forming galaxies we use the far-IR to target galaxies with dust emission.

Herschel selected samples in blank field studies are only able to probe the highest luminosity galaxies $> 10^{12}\ L_{\odot}$ for redshifts $z > 2$. *Herschel* reaches the confusion

limit quickly and no amount of integration will push beyond that limit. Utilizing the gravitational lensing power of massive galaxy clusters, it is possible to surpass the confusion limit enabling the detection of more typical dusty, star-forming galaxies at high redshift.

Recent work by Rujopakarn et al. (2012) detect rest-frame optical emission lines in a sample of bright gravitationally lensed galaxies. The majority of the galaxies in this sample have intrinsic luminosities in the LIRG regime ($10^{11} - 10^{12}$ L$_\odot$). The dust attenuation for the majority of these sources ranges from an A$_V = 0 - 3$, with a significant outlier at ~ 4.5. The majority of these sources have lower dust attenuations than the Swinbank et al. (2004) sample, possibly providing evidence that LIRGs exhibit lower dust attenuations than ULIRGs. While these galaxies are undoubtedly dusty, star-forming galaxies, they were not selected in the far-IR/submm where the dust continuum peaks. By selecting in the far-IR/submm will provide an unbiased sample of the dustiest galaxies.

The *Herschel* Lensing Survey is a survey of 581 massive galaxy clusters using the *Herschel* Space Observatory with the goal of detecting gravitationally lensed dusty, star-forming galaxies. From this sample we target the brightest galaxies for near-IR spectroscopy in order to detect their nebular emission. The inferred far-IR/submm star formation rates of these galaxies suggests that we should be able to detect faint nebular emission, even with high dust attenuation.

In this paper we present a sample of gravitationally lensed dusty, star-forming galaxies in which we detect rest-frame optical nebular emission lines using Keck/MOSFIRE, LBT/LUCI and Magellan/FIRE.

The paper outline is as follows. In section 2 we present the sample, observations and data reduction methods. In section 3 we present the results. In section 4 we discuss the star formation rates, dust attenuations, far-IR colors, metallicity, extreme sources and implications of the study. In section 5 we summarize our results.

The following cosmology is used throughout this paper; H$_0 = 70$ km s^{-1} Mpc^{-1}, $\Omega_M = 0.3$, and $\Omega_\Lambda = 0.7$. The magnitudes are reported in AB and all flux densities are in mJy.

4.2 Data

4.2.1 Sample

The sample in this study comes from the *Herschel* Lensing Survey (HLS; Egami et al., 2010). Two selections were established for the sample presented in this paper.

The first selection targets bright sources (S_{peak} >100 mJy) with SPIRE colors ($S_{500}/S_{250} > 0.4$) suggestive of high redshift far-IR SEDs. Redshifts of the sources were determined by conducting a blind CO redshift search using the IRAM 30m. We carefully selected sources in which the nebular emission lines would be detectable through atmospheric windows in the near-IR. The lines targeted were Hα, Hβ, [NII]λ6583, [OIII]λ5007 and [OII]λ3727. Additional bright sources without redshifts were also targeted, with the emphasis on sources within a few arc minutes of the clusters' cores. Many of the bright sources discovered came from HLS-snapshot which is much shallower in depth than HLS-deep. Typically in HLS-snapshot only one or a few sources were detected, limiting the follow-up using multi-object spectroscopy (MOS). In addition, the majority of the snapshot clusters lacked high resolution optical/near-IR imaging which made counterpart selection difficult. Finally, a few of the sources were well outside the cluster core by several arcminutes which were usually galaxy-galaxy lensed.

The second sample selection in the full sample is a systematic survey of well studied cluster cores (which include several CLASH clusters) of lensed *Herschel* sources of varying brightness, with an emphasis on higher redshift sources selected based on their SEDs. This sample utilizes the MOS capabilities of many near-IR instruments. The sample presented in this paper is much smaller than the main sample and focuses on two clusters, Abell 851 and Abell 1703, that were selected using this method.

These two sample selections provide complementary aspects. The bright sources provide targets that can easily be followed up with a wealth of ancillary data to do detailed studies. The faint sources will provide exciting higher redshift/lower luminosity targets for ALMA and future follow-up with next generation facilities, such as JWST and twenty – thirty meter class telescopes.

4.2.2 Imaging

The *Herschel* Space Observatory observed 581 X-ray selected massive galaxy clusters as part of HLS (Egami et al. 2015 in prep.). The survey consists of two surveys; a deep survey (HLS-deep; 366 hrs) of 54 clusters using *Herschel*/PACS and SPIRE with the bands 100, 160, 250, 350, 500 μm and a snapshot survey (HLS-snapshot; 52 hrs) of 527 clusters using *Herschel*/SPIRE with the bands 250, 350 and 500 μm. In the HLS-deep survey, the PACS images covered a FOV $\sim 7' \times 7'$ and the SPIRE images covered a FOV of $\sim 20' \times 20'$. In the HLS-snapshot survey, the SPIRE images covered a FOV $\sim 12' \times 12'$.

4.2.3 Spectroscopy

Near-IR spectroscopy was obtained for sources in 10 clusters; the details of all the observations are listed in Table 4.1. The clusters targeted are Abell 611, Abell 773, Abell 851, Abell 1703, Abell 2813, CLJ1226, MACSJ0032, MACSJ0111, MACSJ0455 and MACSJ1314. The typical exposure times were 3600–15600 seconds. For the sample presented in this paper we used Keck/MOSFIRE, LBT/LUCI and Magellan/FIRE to obtain the near-IR spectra.

LBT/LUCI

LUCI is a near-IR spectrograph/imager with a FOV of $4' \times 4'$ ($4' \times 2'$ for spectroscopy) and covers a wavelength range of $0.85 - 2.4$ μm. Two gratings were used during the observations; 200 HK and 210 zJHK with resolutions 1880-2600 and 6890–8460 respectively. LUCI has a HAWAII-II detector with 2048×2048 pixels. The N1.8 camera is used for spectroscopy which has a plate scale of $0.249''$/pixel.

LUCI data were reduced using a custom IDL pipeline written by L. Jiang which is based on a modified version of the NIRSPEC pipeline (Bian et al., 2015, 2010; Becker et al., 2009). We used OH sky lines to perform the wavelength calibration. The mapping of the spectral curvature in the multi-object mode of LUCI was determined by tracing the edges of the flat fields. Similarly for the longslit mode,

the spectral curvature was determined by tracing the spatial position of the standard stars. The sky-subtraction was performed by subtracting neighboring science frames from each other, using one as the sky and the other as a science (A-B). The residuals of the sky subtracted frames were fit and removed using the Kelson (2003) sky-subtraction routine. Since there was significant movement in the instrument ($\sim$5 pixels) for a number of the observations, the sky-subtracted science frames were rectified and rebinned. The final science frames were then median combined.

Keck/MOSFIRE

MOSFIRE is a near-IR spectrograph/imager with a FOV of 6.1$'\times$6.1$'$ (6.1$'\times$3$'$ for spectroscopy) and covers a wavelength range of 0.9-2.5 μm. The J grating was used with resolution of 3318. MOSFIRE contains a HAWAII-2RG detector with 2K$\times$2K pixels. The plate scale is 0.18$''$/pixel.

MOSFIRE data were reduced using the MOSFIRE Data Reduction Pipeline (DRP). The MOSFIRE DRP performs the flat-fielding, wavelength calibration, sky-subtraction and Cosmic Ray removal to produce a final product of the 2D spectra. The pipeline uses OH sky lines for the wavelength calibration. The sky-subtraction routine uses neighboring frames to subtract from each other (A-B) and then residuals are fit and removed. We used a star in the mask to perform the flux calibration. *HST* ACS/WFC3 photometry of the star was then used to scale the spectra. A power law was fit to the photometry which was used to correct the spectral slope.

Magellan/FIRE

FIRE is a near-IR spectrograph that covers a wavelength range 0.8 - 2.5 μm. In the Echelle mode, it has a velocity resolution of 50 km/s (R=6000). The Echelle orders covered are 11-32. FIRE contains a HAWAII-2RG detector with 2K$\times$2K pixels. It has a spatial resolution of 0.18$''$/pixel.

FIRE data were reduced using FIREHOSE pipeline. FIREHOSE is written in IDL using the standard IDL packages as well as key packages from Jason Prochaska's xidl package, and Mike Cushing's Spextool. The Echelle mode of the pipeline runs

the following steps; 1) locates the order boundaries using the dome flats, 2) generates flat fields from the internal quartz lamps, sky flats for illumination correction and ThAr lamps to correct the slit tilt, 3) uses OH skylines for the wavelength calibration, 4) 2D sky subtraction and 5) optimally weighted object extraction. Since the source was faint in the spectrum, we were unable to use the object tracing modes of the pipeline. Instead, we used a mode that traces the telluric star at the dither positions A and B to apply to the object.

4.3   Results

A summary of all the sources targeted and the lines detected is listed in Table 4.2. A total of 9 bright sources were targeted for near-IR spectroscopy, with emission lines detected in 5 of the sources. Of the 4 sources with non-detections; two had an unknown redshift and the other two were galaxy-galaxy lensed systems where the targeted line was [OII] (HLSJ0800 at $z = 1.885$ and HLSJ0918 at $z = 5.24$). In the sources that we detect emission lines, Balmer lines were detected, either Hα or Hβ. In the sources that we detect Hα, [NII]λ6583 was always detected. In the sources that we were able to detect Hβ, [OIII]λ5007 was always detected. More details about individual bright sources can be found in the appendix.

The two masks that targeted the clusters Abell 851 and Abell 1703 were observed in a single band (H-band and J-band respectively). From these masks, three *Herschel* sources were added to the sample that did not satisfy the bright source criteria. We targeted 21 *Herschel* sources with these two masks. Out of the 21 sources we obtained the following results; 5 sources we successfully detect emission lines and can determine a redshift, 2 sources we detect a single emission line but are unable to determine the redshift, 5 sources were undetected and 9 sources we only detect in continuum. Of the 5 sources with redshifts we note the following; 1 is a bright source in Abell 851 (included in the bright source count), 1 is a galaxy at $z = 0.3958$ that we detect Paschen β (not included in the sample), and the remaining three are additional sources that are included but are not bright sources. Three of the 9 sources in which we detect continuum were bright (hinting that they might be at

lower redshift) while the remaining 6 were faint.

The fluxes for nebular emission lines are measured by fitting a Gaussian to the line, integrating and subtracting off the continuum. In the cases where the line is too noisy to fit, we sum the flux between two points that enclose the line and subtract off the continuum. Line fluxes for all of the sources are listed in Table 4.3.

4.4   Discussion

4.4.1   Star formation

Balmer Lines

The sample we are selecting from either has Hα or Hβ (but not both) which means we are unable to calculate the dust attenuation by comparing Balmer line ratios. If the dust attenuation is sufficiently high such that the lines are optically thick, the Balmer ratio would not reflect the true dust attenuation. We do not assume a dust attenuation for the sample since one of the goals is to measure it. The Balmer line luminosity is computed for each of the lines, and in the cases of Hβ we assume the theoretical ratio between Hα/Hβ = 2.847 from Osterbrock and Ferland (2006), which assumes a temperature of 10000 K and density of 10^4 cm^{-3}. We then use the linear relation from Kennicutt (1998), which associates Hα line luminosity to the amount of star formation, in Eq. 4.1,

$$SFR \ [M_\odot/yr] = 7.9 \times 10^{-42} \ L_{H\alpha} \ [ergs/s] \tag{4.1}$$

*[O*II*]*

We include the two galaxies for which we had non-detections of [OII] (HLSJ0800 and HLSJ0918). In order to properly estimate the flux limit, we take a blank region of the spectrum and compute the standard deviation of a column of pixels for each wavelength element. For the limit we take the 5σ value. We then use the relation from Kennicutt (1998) to estimate the star formaton from [OII] line luminosity, in Eq. 4.2,

$$SFR \ [M_\odot/yr] = 1.4 \times 10^{-41} \ L_{[OII]} \ [ergs/s] \tag{4.2}$$

Far-IR

We fit the far-IR and submm photometry for all the sources with local galaxy templates from Rieke et al. (2009) and Chary and Elbaz (2001). Each of the template libraries is scaled to the photometry and the best template is decided by which one has the smallest χ^2 value. For the best fitting template we integrate the template from 8 – 1000 μm in order to measure the far-IR luminosity. We then use the Kennicutt (1998) relation for converting to the observed star formation rate using Eq. 4.3.

$$SFR \ [M_\odot/yr] = 4.5 \times 10^{-44} \ L_{FIR(8-1000\mu\mathrm{m})} \ [ergs/s] \tag{4.3}$$

We use the Rieke et al. (2009) luminosities when calculating the far-IR SFRs. The SEDs of the bright sources are in Figure 4.7. The SEDs of the HLS sources detected in Abell 851 and Abell 1703 are in Figure 4.8.

In Figure 4.4 (top-left panel) we plot the observed Balmer and [OII] luminosity versus the observed far-IR luminosity. From the two star formation relations from Kennicutt (1998), for the equivalent amount of star formation, the Hα line luminosity is $\sim$200$\times$ fainter than the far-IR luminosity. For comparison, we include a sample of well known bright gravitationally lensed star forming galaxies from Rujopakarn et al. (2012), represented by open circles. The Rujopakarn et al. (2012) sample includes the galaxies; A2218b ($z = 1.034$), A2667a ($z = 1.035$), The Clone ($z = 2.003$), A2218a ($z = 2.520$), A1835a ($z = 2.566$), cB58 ($z = 2.729$) and the 8 O'clock arc ($z = 2.731$). When we plot the SFRs from each of the relations we can see how the SFRs compare (Figure 4.4, top-right panel). Immediately, it is apparent from our sample that the SFRs from Hα are less than the SFRs derived from the far-IR. The dashed line shows the median Hα SFR suppression factor of 10$\times$ from Swinbank et al. (2004). The suppression factor in Swinbank et al. (2004) sample comes from ULIRGS at redshifts $z = 1.4 - 2.7$. Another way to show this is by comparing the ratio of SFRs

(far-IR to Balmer or [OII]) versus L_{FIR} (shown in Figure 4.4, bottom-left panel). We call the ratio between the SFRs the suppression factor. There appears to be a range of suppression factors for the sources spanning 4–550×, with the median suppression factor of 32× (mean suppression factor of 89×).

In order to compare to the luminosities of the Swinbank et al. (2004) and Rujopakarn et al. (2012) samples we need to determine the intrinsic luminosities from our sample of galaxies. Typically in cluster lensed galaxies you can expect to find a range of magnifications with a range of 5-10× and up to 50×. This depends on the location of the source relative to the center of the cluster and the size of the cluster. Since there are so few sources with luminosities greater than 1×10^{13} $L_\odot$, it is expected that the bright sources in our sample would have a large magnification factor. In order to move forward, we assume all of the bright sources without a lens model have a magnification $\sim 10\times$. Even with such a modest magnification, most of the sources fall in the lower end ULIRG regime, close to the LIRG threshold.

While our sample borders on the LIRG/ULIRG regime, the Swinbank et al. (2004) sample spans the luminosity range 2.4 – 14.8 $\times10^{12}$ $L_\odot$, with the majority of their galaxies with luminosities above 5×10^{12} $L_\odot$. Our sample appears to probe lower luminosities than the Swinbank et al. (2004) sample. The Rujopakarn et al. (2012) sample spans luminosities from 0.1 – 5×10^{12} $L_\odot$, with the majority of their sources below 10^{12} $L_\odot$. Overall, the Rujopakarn et al. (2012) sample has lower Hα suppression than our sample and the Swinbank et al. (2004) sample. A1835a is the one notable exception from the Rujopakarn et al. (2012) sample, with a suppression factor of 61×. The bright star forming galaxy sample from Rujopakarn et al. (2012) may not necessarily completely overlap with our *Herschel* selected sample. In addition, many of the galaxies in the Rujopakarn et al. (2012) sample are bright in *HST*/ACS, whereas preliminary analysis from our sample suggests that many of our sources' SEDs are quite steep and expected to be much fainter in the observed optical. There is one notable exception, MACSJ032 at redshift $z = 3.632$, in which it is detected in *HST*/ACS F606W and F814W.

4.4.2 Dust attenuation

Without Hβ or higher order Balmer transitions it is difficult to compute the reddening in order to determine how much the dust is affecting the Balmer lines. As we mentioned earlier, if the lines are optically thick, the reddening determined from Balmer line ratios would not reflect the true dust attenuation in the galaxy. One way to estimate the dust attenuation is by comparing the ratio of the far-IR SFR to the SFR computed from the Balmer or [OII] lines. If we assume that all of the suppression that we measure in the Balmer or [OII] lines is due to dust, we would come up with equation 4.4,

$$A_V = 2.5 \ log_{10} \left[\frac{SFR_{FIR(8-1000\mu\mathrm{m})}}{SFR_{Balmer \ or \ [OII]}} \right] \tag{4.4}$$

In Figure 4.4 (bottom-right panel) shows the distribution of attenuations. As expected, it looks similar to the logarithm of the ratio of the SFRs. From our sample we find that the median dust attenuation is $A_V = 3.7 \pm 1.1$ (mean is $A_V = 3.7 \pm 1.5$). In the Swinbank et al. (2004) sample they find a median dust attenuation $A_V = 3.0 \pm 1.0$. Our sample appears to have a larger median dust attenuation than seen in Swinbank et al. (2004). However, we need to cautious as our sample is small and it could be dominated by a few extremely dusty sources. When comparing to the Rujopakarn et al. (2012) sample, the A_V range they span is 0.4–4.5, with the majority of their sources below A_V of 3.0. Their one extreme source we identified earlier is A1835a, which has an A_V of 4.5.

4.4.3 *Herschel*/SPIRE Colors

One way to check that our assumption for the magnification factor is a reasonable one is by comparing the *Herschel*/SPIRE colors of our galaxy sample to local galaxy templates. Figure 4.1 shows the three colors of the *Herschel*/SPIRE bands by comparing the flux ratios of S_{350}/S_{250}, S_{500}/S_{350} and S_{500}/S_{250}. Plotted are the colors of the galaxies targeted in the sample (listed in Table 4.2). The 2D histogram shows the full distribution of all the sources in HLS. The Rieke et al. (2009) templates col-

ors are over-plotted for comparison showing what they would look like at redshifts $z = 1 - 6$ for three luminosities (10^{11}, 10^{12} and 10^{13} L$_\odot$). The Rieke et al. (2009) templates all appear to follow similar tracks. The higher luminosity templates (10^{12} and 10^{13} L$_\odot$) appear similar to each other and roughly have similar redshift-color space. When comparing the lower luminosity template (10^{11} L$_\odot$) to the higher luminosity ones, we find that the lower luminosity template covers a slightly different color space and redshift range, which is offset to lower redshifts by ~ 1. Comparing the HLS sample in a similar way we find that the redshift distribution agrees more with the lower luminosity template (10^{11} L$_\odot$) than the higher luminosity ones, with the notable exception of HLSJ0918 at $z = 5.24$.

4.4.4   Metallicity

For our sample we did not have a complete set of Balmer and forbidden lines (e.g. [NII], [OIII] and [OII]) so we must rely on two methods for determining metallicity for each galaxy; N2 and O3HB. For the sources where we were able to detect Hα and [NII]$\lambda 6583$, at redshifts $z < 2.6$, we used the N2 method (Pettini and Pagel, 2004). For sources at higher redshift ($z = 3.3 - 3.7$) without [OII]$\lambda 3727$ we used O3HB (Maiolino et al., 2008). The O3HB method is double valued and we report both values in Table 4.4. The expectation is that since these are dusty, star-forming galaxies, they should have more metals in them from the ongoing star formation, therefore their metallicity values would be larger than typical LBG or LAE at similar redshifts. In the O3HB calculation we assume that the upper value is the metallicity for each galaxy since it appears more reasonable.

We find that the 4 galaxies with the N2 diagnostic have metallicities ranging from 8.4–8.9. In the Swinbank et al. (2004) sample, the majority of galaxies had sub-solar metallicity with a range of metallicities 8.2–9.0, at redshifts $z = 1.4 - 2.7$. The Rujopakarn et al. (2012) sample spans the metallicity range of 8.2–8.9. We do not see any differences between the metallicities in our sample compared to the Swinbank et al. (2004) or Rujopakarn et al. (2012) samples. One of the sources, HLSJ1314, was outside of the valid range used for the N2 diagnostic, which is -2.5

< N2 < -0.3.

4.4.5   The Extreme Hα Suppression in HLSJ1314

Counterpart Identification and Morphology

HLSJ1314 has the largest suppression of Hα in our sample with a suppression factor of 550×. Figure 4.5 shows the multi-band image of HLSJ1314 (*Herschel*/SPIRE 250 μm, *Spitzer*/MIPS 24, *Spitzer*/IRAC [3.6] and [4.5], UKIRT/WFCAM J and K, JVLA 4-8 GHz). The source was detected in *Herschel* and satisfied the bright source criteria. The *Spitzer*/MIPS 24 μm image shows an elongated source. IRAM 30m observations identified the redshift at $z = 1.447$ from CO(3-2) and CO(2-1). Further follow-up with *Spitzer*/IRAC reveal two bright sources near the center of the cluster MACSJ1314.3-2515. The source on the left is the BCG of MACSJ1314.3-2515 and the source on the right corresponds to the *Herschel* and *Spitzer* sources. UKIRT/WFCAM J and K imaging show a bright red arc (J-K = 1.64). JVLA 4-8 GHz imaging detects 3 star forming knots at the position of the arc, with the center knot being significantly detected (S/N∼6.9) and two knots at the edge tentatively detected (S/N∼4.1 and 3.8).

*Hα and [N*II*]*

Magellan/FIRE spectroscopy targeted the arc with the slit corresponding to the position of the bright knot in the JVLA image. Figure 4.6 shows the 2D and 1D spectrum of HLSJ1314. Magellan/FIRE clearly detects Hα and [NII]. With such a large suppression factor, we want to emphasize that the Hα line is detected and it is not a limit. The stellar continuum is also detected, which strongly contrasts with how faint the Hα line is. The spectrum shows that the amplitude of the Hα line is about the same as the [NII] line. The line ratio suggests that MACSJ1314 could be an AGN; we will discuss this further in the next section. In the 2D spectrum, there is a region above the continuum in which Hα is also detected but without the stellar continuum. This region could contain a younger stellar population.

The Hα suppression factor is not corrected for slit loss, which could potentially decrease the value. Due to the slit size ($7''\times0.75''$), it was necessary to place the slit perpendicular to the arc. This requires a slit loss correction. Assuming Hα is detected throughout the arc, the slit loss correction would be no larger than $5\times$ (based on the flux in the WFCAM K-band image). Since we do not know what the flux of Hα is throughout the arc, this is adds to the overall uncertainty in our suppression calculation. Near-IR IFU observations are necessary to resolve whether Hα could be detected throughout the arc.

AGN Contribution

The other concern, mentioned earlier, is that the [NII]/Hα ratio suggests that MACSJ1314 could be an AGN. If the galaxy contained an AGN, we would need to worry about how much the AGN contributes to the far-IR emission, potentially reducing the far-IR derived star formation rate.

There are several ways to test for an AGN. The first is by using the BPT diagram. The [NII]/Hα ratio can tell us if a galaxy is in the star forming region, composite region or AGN region. We find $\log_{10}$([NII]/Hα) = -0.044±0.09, which is not in the BPT star forming region (Kauffmann et al., 2003). Without a detection of Hβ and [OIII] we will be unable to determine if the [OIII]/Hβ ratio is either in the composite region or AGN region (Kewley et al., 2001; Juneau et al., 2011). While the single line ratio is suggestive of whether a galaxy contains an AGN, it is not deterministic. We note that at high redshift ($z > 1$) there is evidence for an offset in the BPT relative to local galaxies, with higher [NII]/Hα and [OIII]/Hβ (Shapley et al., 2005; Erb et al., 2006; Liu et al., 2008). It has been suggested that this offset could be a selection effect as UV-selected galaxies experience a stronger offset than the rest-frame optical selected galaxies (Shapley et al., 2015). In addition, there is evidence that the offset could be mass-dependent, with the lower stellar mass galaxies experiencing the offset (Shapley et al., 2015). One possible intrepetation of the offset could be that more galaxies at high redshift contain a weak AGN (Wright et al., 2010). With the redshift evolution of the BPT in mind, the [NII]/Hα line ratio for HLSJ1314 is far enough

over in the composite/AGN region for it to still be considered possibly an AGN.

Another way to test for an AGN is by the velocity width of the Balmer lines. The line width of an AGN's broad line region is typically >1000 km/s. We find that the velocity width (FWHM) of Hα in MACSJ1314 is 370$\pm$54 km/s. However, Type-2 Seyfert galaxies have line widths of about 400 km/s. It is thought that the broad line regions in Type-2 Seyfert galaxies are obscured due to the steep viewing angle down its rotation axis (Antonucci, 1993). The line width suggests that we cannot rule out the possibility of an AGN.

Finally, investigating the mid-IR and far-IR fluxes will tell us whether we may potentially have an obscured AGN. The *Spitzer*/MIPS 24 μm flux of HLSJ1314 is 1.4$\pm$0.2 mJy. The *Herschel*/SPIRE 250 μm flux is 155 mJy. The slope between SPIRE 250 μm and MIPS 24 μm is too steep for an AGN. A significant fraction of galaxies with luminosities $> 10^{13}$ $L_{\odot}$ have an AGN. We fit local templates to the far-IR/submm photometry of HLSJ1314 and find that the best fitting Rieke et al. (2009) template is 10^{11} $L_{\odot}$. From this evidence we conclude that there could be a weak AGN in HLSJ1314 and that its far-IR contribution is mostly from star formation.

4.4.6 Implications of this study

While the sample is small, it is tantalizing that the majority of these sources' Balmer lines experience a suppression factor $> 10\times$. With the magnification factors, we might be able to answer the question whether LIRGs have less dust attenuation than seen in ULIRGs and HyLIRGs at redshifts $z = 1 - 4$. The challenge is the limited number of detections of multiple Balmer lines (i.e. Hα and Hβ). The full sample of 48 galaxies only contains 5 with both Hα and Hβ. Confirmation of the Hα suppression with a measurement of the dust reddening would strengthen this result. However, as mentioned earlier, large dust attenuations may imply that the lines are optically thick and may not represent the true dust attenuation.

One possible implication of this result is that several studies exploring the total SFR density may be missing star formation from highly dust obscured sources. While this idea is not unique, this study brings to light the existence of these extremely

dusty sources. It may be difficult with such a study to determine the number density of this population, and ultimately determine the total obscured SFR contribution. This also has implications to higher redshifts ($z > 4$) where galaxies are almost exclusively selected in the UV. Dust may have a greater role in the Universe than originally thought. Some caution is necessary as this is still a small sample of non-uniformly selected galaxies. The only common selection of sources is that they are from *Herschel* in the fields of galaxy clusters.

Regardless of this caution, it is interesting to note that a number of sources remain undetected. The UV follow-up of *Herschel* selected galaxies yielded very few redshifts of galaxies ($\sim 5\%$) (Casey et al., 2012b). Near-IR follow-up has done slightly better, but still has a high failure rate of detection. Not only is this demonstrated with the 2 masks we mention here but in the full sample which covers J, H, and K bands in a uniform way. There are several caveats to this, such as limited number of atmospheric windows, incorrect counterparts, or blends of several sources spanning a range of redshifts. A non-detection could imply that a source is highly dust obscured or simply that the nebular emission lines were outside of the atmospheric windows.

Dust obscuration could play a larger role in these galaxies and it may be important to note that using different Hydrogen series may yield a better correlation with the far-IR star formation rates. Rujopakarn et al. (2012) investigated Paschen and Bracket series for a sample of lensed galaxies galaxies. While these galaxies had lower dust attenuations than in our sample, they found that while Hα under-predicted the star formation rates, the Paschen and Brackett lines agreed with the far-IR derived star formation rates. This is also most recently shown in a sample of low redshift galaxies ($z < 0.4$) by Shipley et al. (2015).

An interesting possibility yet to be explored is that we may not be seeing dust attenuation of Hα but instead seeing a difference in star formation timescales. It is known that the Balmer lines are considered an instantaneous star formation indicator, with the star formation averaged over the past 10 Myr (Kennicutt and Evans, 2012). Similarly, the far-IR star formation indicator is star formation averaged over the past 100 Myr (Kennicutt and Evans, 2012). Hayward et al. (2014) demonstrate

that in simulations of galaxies undergoing mergers, the far-IR SFR over-predicts the SFR derived from Hα, resembling a post-starburst phase. Hayward et al. (2014) also notes that this over-prediction of the SFR would also occur in galaxies in which the star formation suddenly shuts off.

There are several mechanisms for shutting off star formation in a galaxy, through interactions with the gas, such as it being: 1) blown out by either a stellar wind or an AGN/QSO, 2) depleted through star formation or 3) ejected through a merger or interaction (though the gas would eventually re-accrete and form stars). If the gas is missing, it may be from one of these processes. However, a recent study by French et al. (2015) showed that for a sample of local post-starburst galaxies, that they still contained their molecular gas, even though they showed little to no Hα emission. This is troubling and possibly indicates some other mechanism that shuts off star formation.

4.5 Conclusions

We conducted a near-IR spectroscopic survey of gravitationally lensed dusty, star-forming galaxies targeting their nebular emission lines. We were able to detect nebular emission lines in 8 of the 12 galaxies that we targeted. Of the 4 galaxies that we were unable to detect nebular emission lines, 2 of them had an unknown redshift.

- For the gravitationally lensed dusty, star-forming galaxies in our sample, the Balmer lines under-predict the far-IR star formation rates by a median factor of 30×, which is larger than reported in Swinbank et al. (2004) (10×). If a magnification factor of 10× is assumed for all of the sources, their luminosities would fall on the LIRG/ULIRG threshold. This is larger nebular suppression reported than previously in the literature at lower luminosity.

- When comparing the Hα derived star formation rates to the far-IR, we find that the median dust attenuation of the sample is A$_V$ = 3.7±1.5.

- By using the N2 diagnostics in determining metallicity, we find that our galaxies

are similar to the Swinbank et al. (2004) and Rujopakarn et al. (2012) samples
with metallicities ranging from 8.4-8.9.

- We discover that one of the sources in our sample, HLSJ1314, under-predicts
  the far-IR star formation rate by a factor of $550\times$ ($A_V = 6.9 \pm 0.5$).

- HLSJ1314 exhibits an [NII]/Hα ratio of -0.44 which suggests that it is in the
  composite/AGN region of the BPT. Further analysis suggests that it may only
  contain a weak AGN, which means most of the far-IR/submm luminosity is
  from star formation.
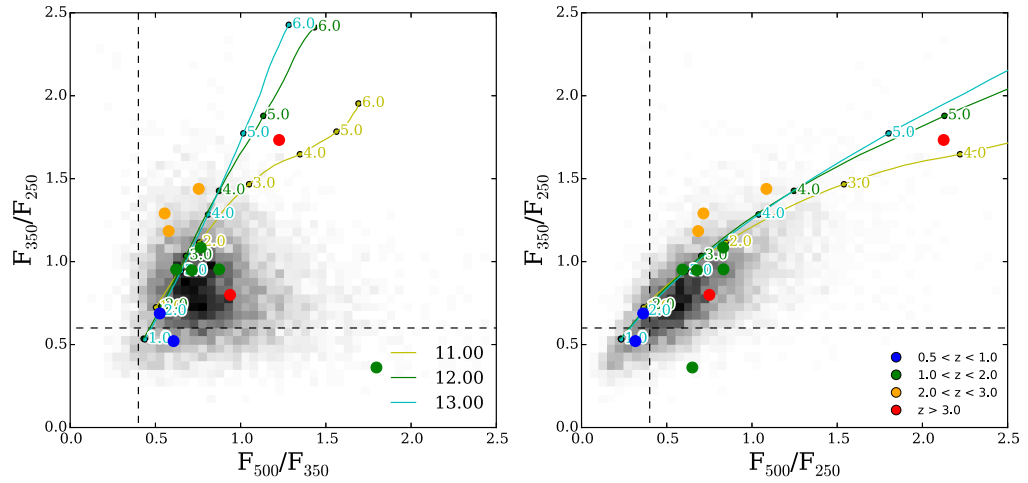
Figure 4.1: *Herschel*/SPIRE color-color diagram showing the flux ratios of F_{350}/F_{250},
F_{500}/F_{350} and F_{500}/F_{250} of the HLS sample. The circles are the galaxies targeted in
this sample. The gray histogram shows the full HLS sample for comparison. The
solid lines represent Rieke et al. (2009) a given templates color at redshifts $z = 1-6$.
The number plotted are marking the redshift of a given template. Three templates
are plotted for comparison (10^{11}, 10^{12}, and 10^{13} $L_\odot$). The dashed lines show the
color cuts for the bright sources.
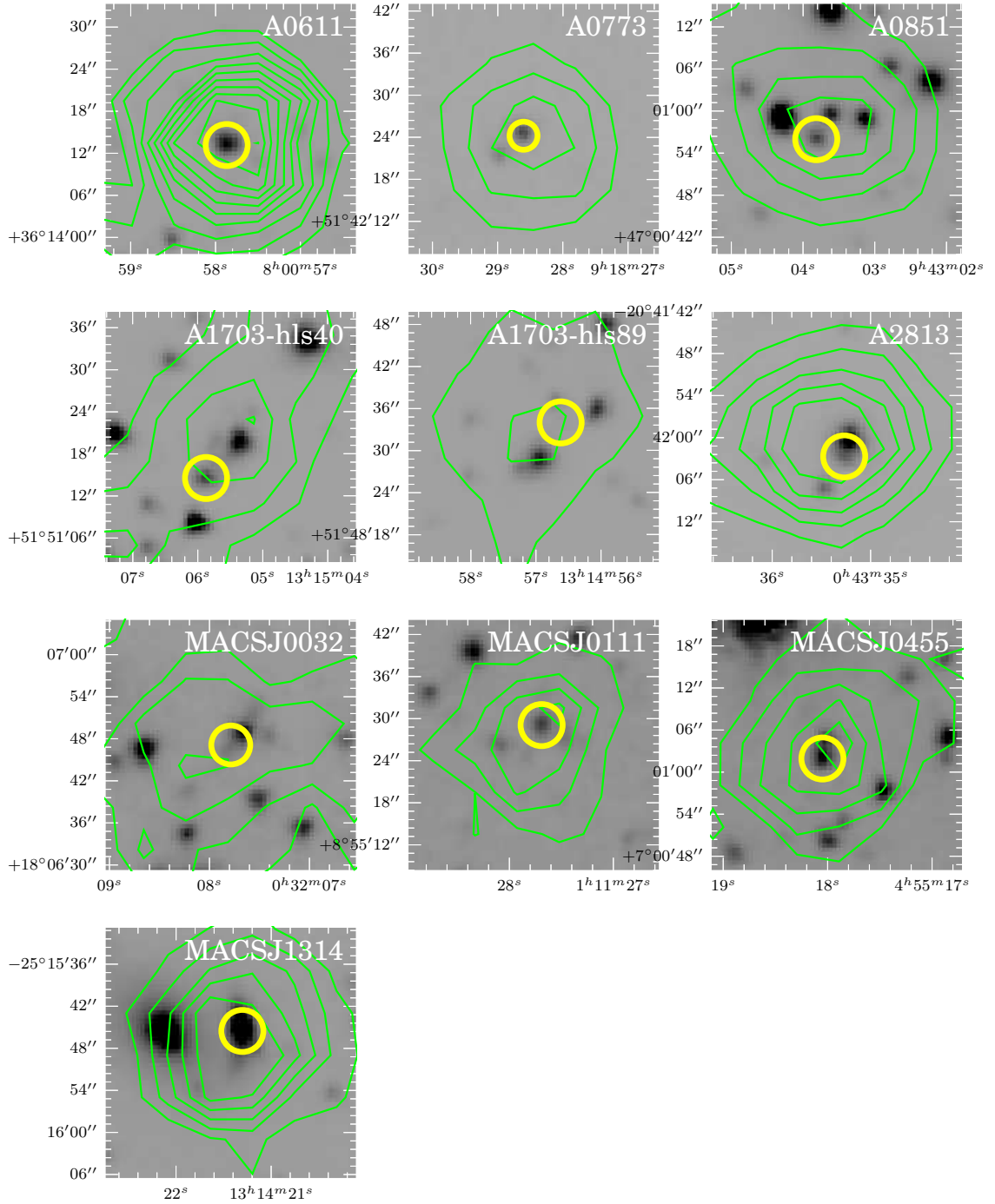
Figure 4.2: *Spitzer*/IRAC [3.6] images of each of the galaxies targeted. The green contour is the *Herschel*/SPIRE 250 μm. The yellow circle marks the source targeted for spectroscopy.
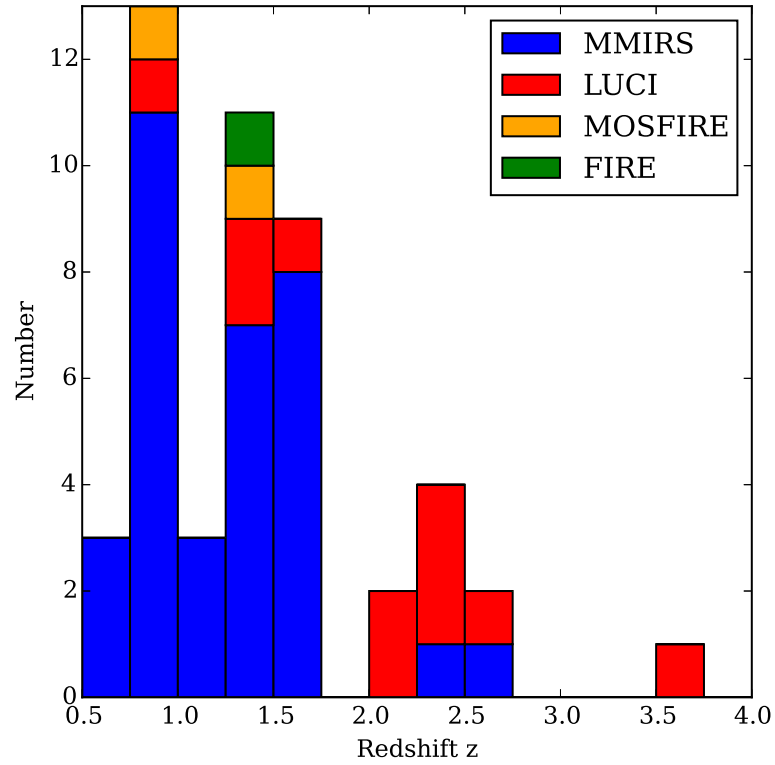
Figure 4.3: A preview of the distribution of the full sample when the survey is complete. The Magellan/MMIRS sample is biased towards lower redshifts since at the time of observations there was no K-band grism. This would make detection of galaxies at $z = 2 - 2.6$ more challenging since you would only be able to detect Hβ and [OIII] in the H-band. The LBT/LUCI and Magellan/FIRE samples are targeted on bright sources with known redshifts. The Keck/MOSFIRE sample comes from the a joint effort to study the UV emission lines in $z > 6$ galaxies (Stark et al., 2015).
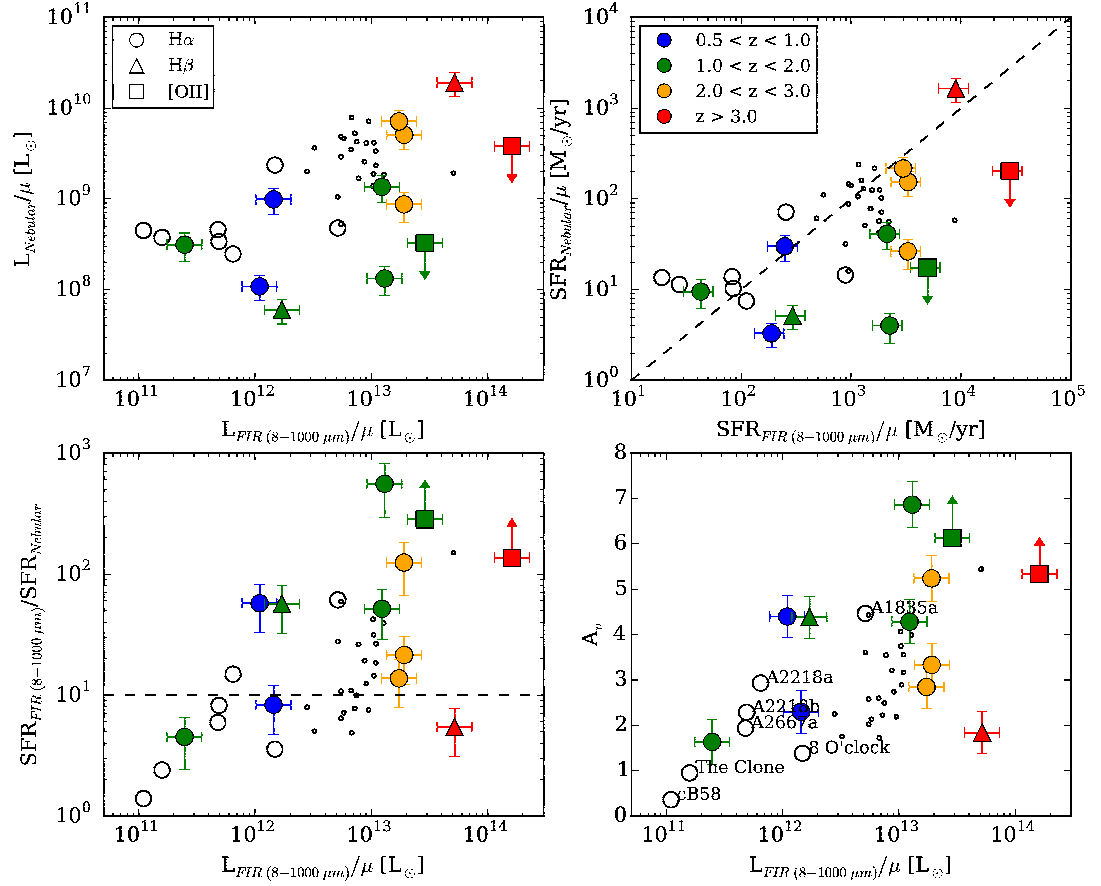
Figure 4.4: Top left: Nebular luminosity versus far-IR luminosity. Top right: Nebular SFR versus far-IR SFR. Bottom left: Ratio of far-IR SFR to the nebular SFR versus far-IR luminosity. Bottom right: Dust attenuation versus far-IR luminosity. The filled shapes with colors are sources from our sample. Their observed values are plotted (not accounting for each of their magnification factors). The circles represent Hα, triangles represent Hβ and boxes represent [OII]. The colors represent redshift; blue is $0.5 < z < 1.0$, green is $1.0 < z < 2.0$, yellow is $2.0 < z < 3.0$ and red is $z > 3.0$. The small black circles are from Swinbank et al. (2004). The large black circle are from Rujopakarn et al. (2012) sample of bright gravitationally lensed galaxies. Their intrinsic values are plotted. The dashed line is the median suppression factor from the Swinbank et al. (2004) sample.
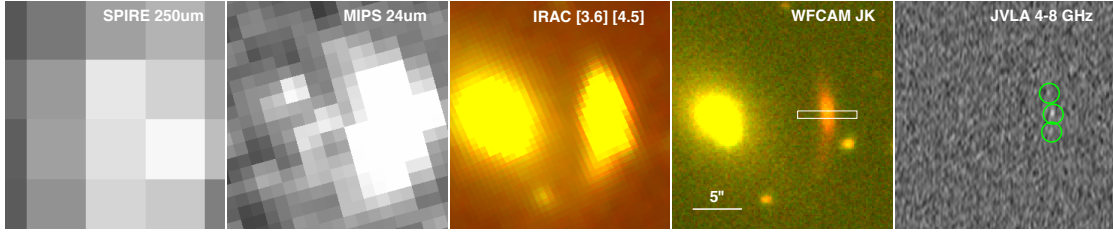
Figure 4.5: Multi-band image of the the HLS bright source HLSJ1314. UKIRT/WFCAM J and K images reveals a red arc at the position of the *Herschel*/SPIRE 250 μm and *Spitzer*/MIPS 24 μm sources. In *Spitzer*/IRAC the arc is as bright at the BCG of MACSJ1314.3-2515. The white box marks the position of the Magellan/FIRE slit (7″×0.75″) The green circles mark the positions of the three sources detected in the JVLA 4-8 GHz image.
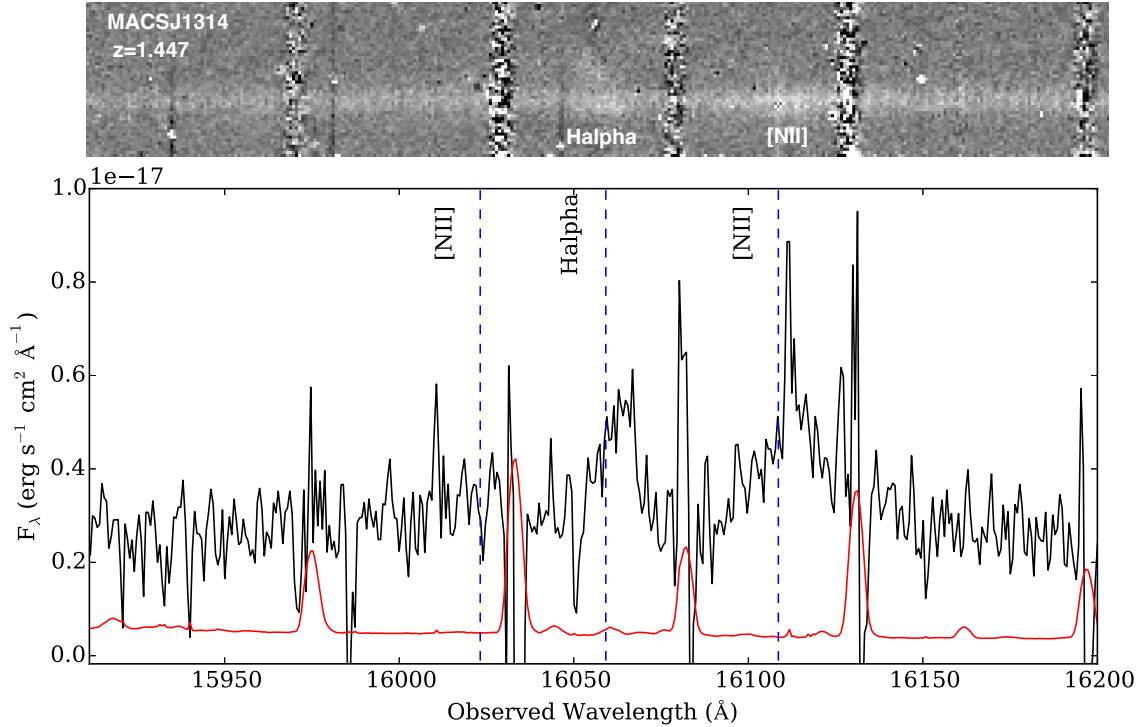
Figure 4.6: 2D and 1D spectrum of HLSJ1314. Hα and [NII] are detected in HLSJ1314, as well as the continuum. The stellar continuum contrasts how faint the Hα line is.
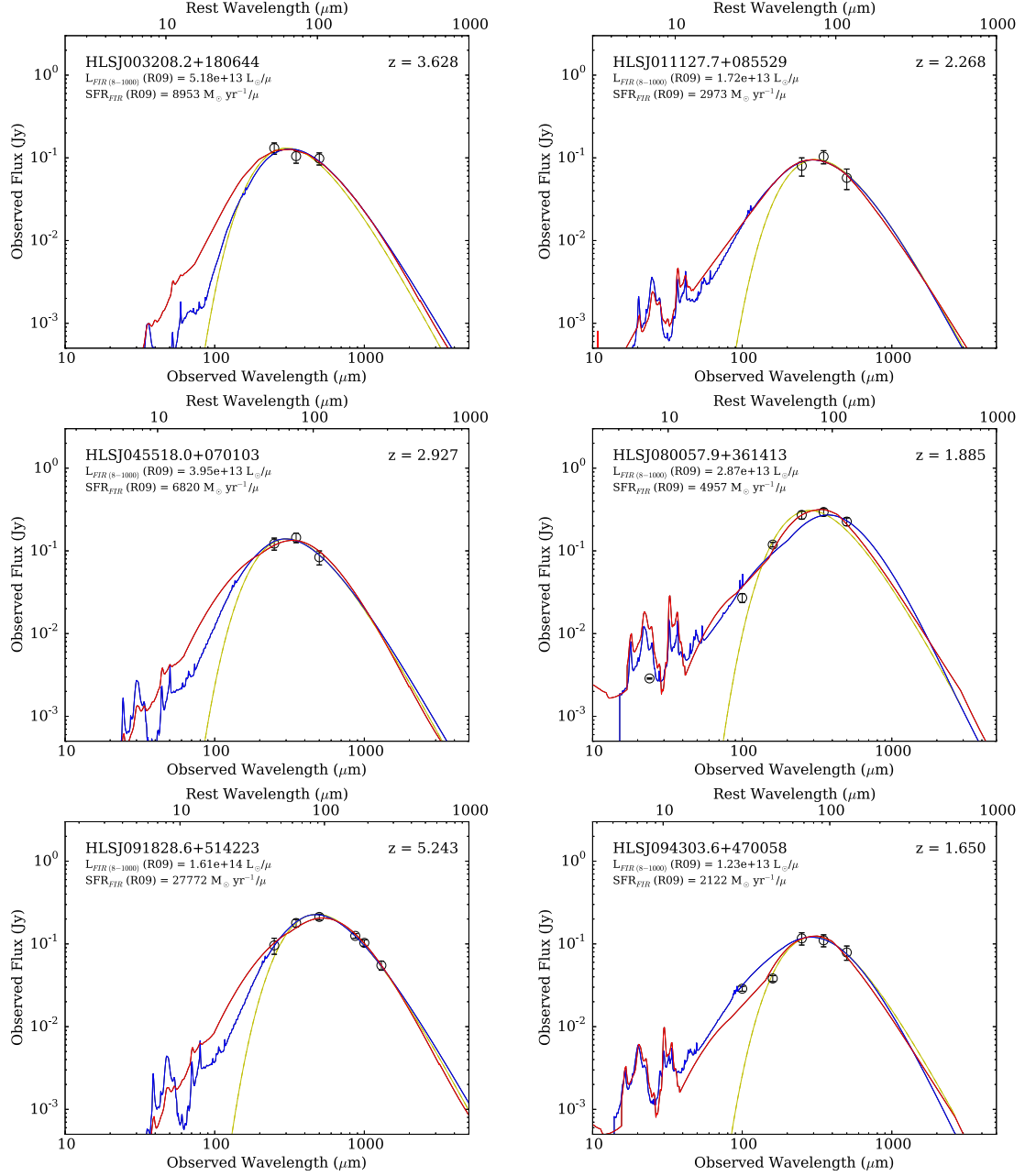
Figure 4.7: Far-IR SEDs of the HLS bright sources. The red line is the best fitting Chary and Elbaz (2001) template. The blue line is the best fitting Rieke et al. (2009) template. The yellow line is the best fitting modified blackbody fit to the photometry.
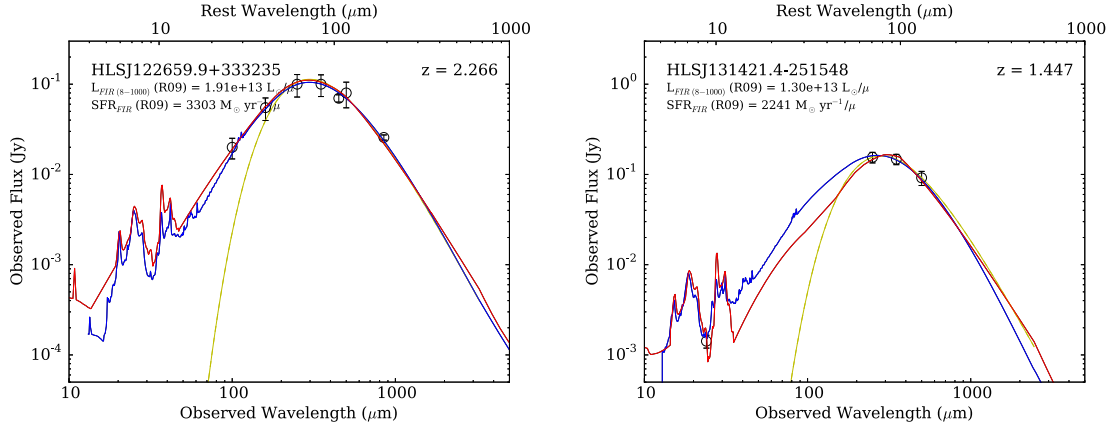
Figure 4.7: (continued)
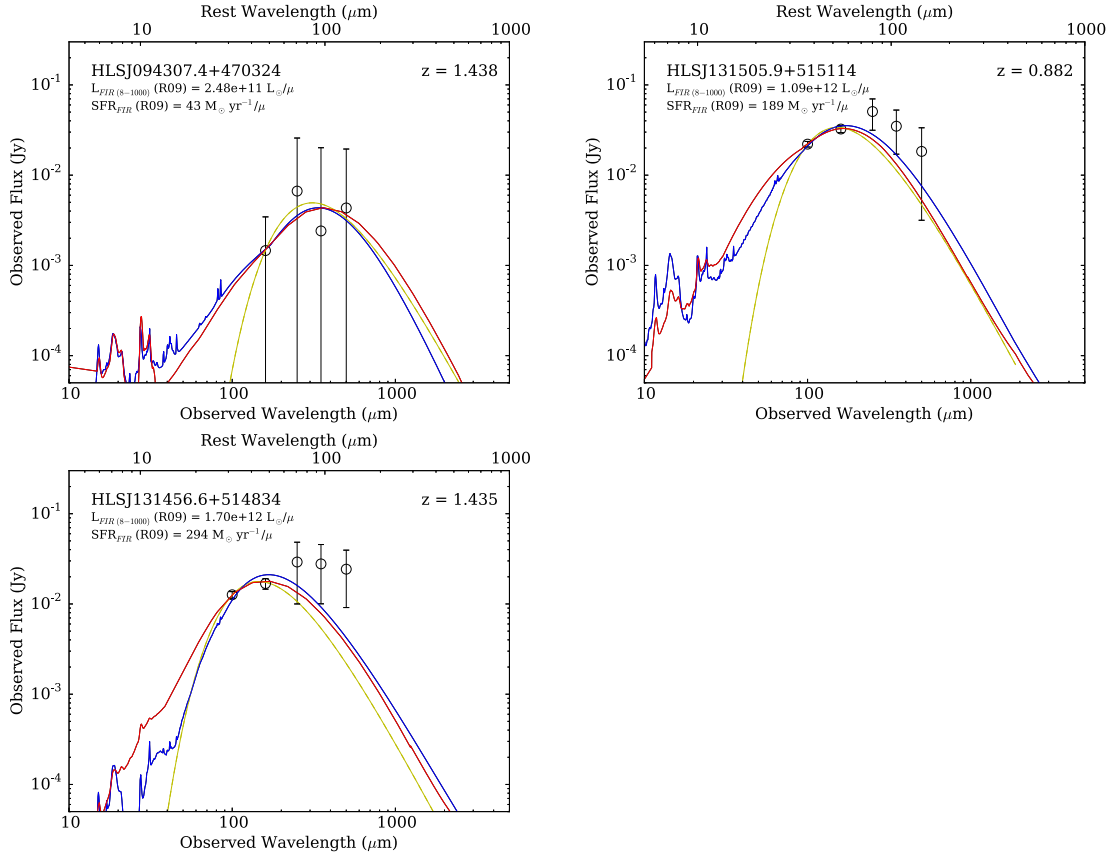
Figure 4.8: Far-IR SEDs of the HLS sources detected in Abell 851 and Abell 1703. Line descriptions same as Figure 4.7.

Table 4.1.   Observations

Cluster	Instrument	Grating/Mode	Filters	Central Wavelegnth [μm]	Wavelength Range [μm]	t_{exp} [s]	Date
A0611	LBT/LUCI	200 HK	zJ	1.175	1.00–1.50	15600	20140413, 20141025
A0773	LBT/LUCI	210 zJHK	K	2.30	2.13–2.45	10800	20140103
A0851	LBT/LUCI	210 zJHK	H	1.70	1.60–1.79	6600	20130305
A1703	Keck/MOSFIRE	YJ	J	1.25	1.15–1.35	9360	20140411
A2813	LBT/LUCI	200 HK	HK	1.93	1.50–2.30	3600	20141026
CLJ1226	LBT/LUCI	200 HK	HK	1.93	1.50–2.30	3600	20140413
MACSJ0032	LBT/LUCI	210 zJHK	K	2.20	2.03–2.35	14400	20141024
MACSJ0111	LBT/LUCI	200 HK	HK	1.93	1.50–2.30	3600	20141024
MACSJ0455	LBT/LUCI	210 zJHK	H	1.65	1.55–1.74	12000	20141024
MACSJ1314	Magellan/FIRE	Echelle	$\cdots$	$\cdots$	0.81–2.51	3888	20141231

Table 4.2.   *Herschel* Sources Targeted

ID	Cluster	Redshift	Lines
Bright Sources (S$_{peak}$ > 100 mJy and S$_{500}$/S$_{250}$ > 0.4)			
HLSJ003208.2+180644	MACSJ0032	3.628	Hβ, [OIII]λ4959,5007
HLSJ004335.4-204200	A2813	?	(no lines detected)
HLSJ011127.7+085529	MACSJ0111	2.269	Hα, [NII]λ6583,
HLSJ045518.0+070103	MACSJ0455	2.927^a	(no lines detected)
HLSJ080057.9+361413	A0611	1.885	[OII]λ3727 (non-detection)
HLSJ091828.6+514223	A0773	5.243	[OII]λ3727 (non-detection)
HLSJ094303.6+470058	A0851	1.650	Hα, [NII]λ6583
HLSJ122659.9+333235	CLJ1226	2.265	Hα, [NII]$\lambda\lambda$6548,6583
HLSJ131421.4-251548	MACSJ1314	1.447	Hα, [NII]λ6583
Bright Sources from the Literature			
HLSJ204314.2-214439	RXCJ2043	2.041	Hα, [NII]
HLSJ224841.8-443157	AS1063	0.610	Hα-H8, [NII]$\lambda\lambda$6548,6583, [OIII]λ4959,5007, [OII]λ3727
Sources S$_{peak}$ < 100 mJy			
HLSJ094307.4+470324	A0851	1.438	Hα, [NII]λ6583
HLSJ131456.6+514834	A1703	1.435	Hβ, [OIII]$\lambda\lambda$4959, 5007
HLSJ131505.9+515114	A1703	0.882	Hα, [NII]λ6583, [SII]$\lambda\lambda$6717,6731

Note. — [a] HLSJ045518.0+070103 redshift is unknown, Zavala et al. 2015 CO results suggests the redshift could be at 2.927, however there is a solution at z=1.618. The LBT/LUCI non-detection makes the lower redshift solution less likely.

Table 4.3.   Nebular Line Fluxes

Source	Hβ [10^{18} erg/s/cm^2]	[OIII]λ4959 [10^{18} erg/s/cm^2]	[OIII]λ5007 [10^{18} erg/s/cm^2]	[NII]λ6548 [10^{18} erg/s/cm^2]	Hα [10^{18} erg/s/cm^2]	[NII]λ6583 [10^{18} erg/s/cm^2]	[SII]λ6717 [10^{18} erg/s/cm^2]	[SII]λ6731 [10^{18} erg/s/cm^2]
Bright Sources (S$_{peak}$ > 100 mJy and S$_{500}$/S$_{250}$ > 0.4)								
HLSJ003208.2+180644	599.4±24.9	94.0±30.0	378.9±32.3	⋯	⋯	⋯	⋯	⋯
HLSJ011127.7+085529	⋯	⋯	⋯	⋯	696.9±35.8	⋯	⋯	⋯
HLSJ094303.6+470058	⋯	⋯	⋯	⋯	289.0±37.8	45.1±20.7	⋯	⋯
HLSJ122659.9+333235	⋯	⋯	⋯	61.3±32.4	496.8±28.5	257.9±60.0	⋯	⋯
HLSJ131421.4-251548	⋯	⋯	⋯	⋯	39.1±7.7	35.3±2.4	⋯	⋯
Sources S$_{peak}$ < 100 mJy								
HLSJ094307.1+470326	⋯	⋯	⋯	⋯	93.8±16.3	⋯	⋯	⋯
HLSJ131456.6+514834	18.0±0.8	21.4±1.2	69.9±1.4	⋯	⋯	⋯	⋯	⋯
HLSJ131505.9+515114	⋯	⋯	⋯	⋯	108.8±3.2	47.6±2.4	24.7±3.3	17.5±7.8

Table 4.4.   Metallicity

Source	Redshift	N2	O3HB	
			lower	upper
Bright Sources (S$_{peak}$ > 100 mJy and S$_{500}$/S$_{250}$ > 0.4)				
HLSJ003208.2+180644	3.628	$\cdots$	6.86±0.05	8.90±0.05
HLSJ094303.6+470058	1.650	8.39±0.06	$\cdots$	$\cdots$
HLSJ122659.9+333235	2.265	8.89±0.13	$\cdots$	$\cdots$
HLSJ131421.4-251548	1.447	9.29±0.27	$\cdots$	$\cdots$
Sources S$_{peak}$ < 100 mJy				
HLSJ131456.6+514834	1.435	$\cdots$	7.50±0.15	8.31±0.15
HLSJ131505.9+515114	0.882	8.80±0.12	$\cdots$	$\cdots$

CHAPTER 5

Conclusions and Future Directions

5.1   Main Results of this Thesis

Chapter 2: When investigating one of the most massive galaxy clusters Abell S1063
we learn the following:

- In the massive galaxy cluster Abell S1063 we find 3 bright IR galaxies. Two
  of the galaxies are infalling cluster members, and the third is a gravitationally
  lensed galaxy at redshift $z = 0.6$.

- For the galaxy at redshift $z = 0.6$ we discover a luminous giant star forming
  region that is about a kiloparsec in diameter and 2 orders of magnitude brighter
  than local HII regions, similar to star forming galaxies at $z \sim 2$.

- We detect a significant offset in the *Spitzer*/MIPS 24 μm emission from the
  $z = 0.6$ galaxy, suggesting that we are detecting the giant star forming region.
  The star forming region appears to contribute 30 $M_\odot$/yr in the far-IR/submm,
  which is 3× larger than the star formation rate inferred from Hβ.

- The kinematics of the $z = 0.6$ galaxy suggest that its HII region formed in
  isolation, without interaction from any nearby galaxies, similar to star forming
  galaxies at $z \sim 2$.

- When investigating the dust, we can estimate the gas fraction and depletion
  time scale for the star forming region and find that it is similar to other galaxies'
  star forming regions at its redshift. The depletion timescale is about 130-340
  Myr.

- The star forming region's size and luminosity appear similar to other star forming regions at higher redshifts ($z \sim 2$), making it an excellent nearby laboratory to study star forming regions at high redshift.

Chapter 3: When exploring the molecular gas and dust emission from one of the most luminous galaxies in HLS, in the cluster RXCJ2043, we discover the following:

- One of the brightest sources in HLS is a blend of two galaxies, one at $z = 2.0$ and the other at $z = 4.7$. High resolution SMA imaging reveals that the $z = 2.0$ galaxy is a large arc and the $z = 4.7$ galaxy is triply imaged, which implies that other bright *Herschel* sources could have such multiplicity.

- Using MCMC to deblend the far-IR/submm flux densities we are able to determine that both galaxies are ULIRGs. We also find that the $z = 4.7$ galaxy is detected in *Herschel*/PACS. It has a warmer dust component than found in the local templates which hints at it possibly being an AGN.

- We find that clumps in the integrated CO(1-0) maps of the $z = 2.0$ galaxy do not match the SMA 870 μm star forming clumps. This is a result of there being two distinct structures in the CO(1-0). When removing the secondary CO structure from the CO(1-0) map, we can reproduce the morphology and intensity we find in the SMA 870 μm map. This suggests that other galaxies may contain molecular gas that is unassociated with star formation.

- From the dynamical mass, dust emission and CO(1-0) line luminosity we are able to accurately compute the molecular gas mass. With this abundance of information we are able to constrain α_{CO}. We find that α_{CO} is consist with the value of 4, which is similar to molecular clouds in the Milky Way. Local ULIRGs have an $\alpha_{CO} \approx 0.8$. When accounting for the redshift evolution of the star-forming main sequence, the arc's sSFR falls on the sequence. Galaxies on the star-forming main sequence typically have α_{CO} values of ~ 4.

- When removing the secondary structure in the $z = 2.0$ galaxy, we find the integrated CO(1-0) maps correlate well with the SMA 870 μm map. We find

when comparing the clumps on a Kennicutt-Schmidt relation to the entire galaxy that they have shorter lifetimes. This suggests that unresolved studies may be underestimate the star formation rate surface density of galaxies.

- We investigate the secondary CO structure in the $z = 2.0$ galaxy and find that it could be a wind as its CO(4-3) line profile contains a second faint broad component. In addition, there is a gap in the CO(1-0) emission which also hints that a kinematically distinct structure is at the edge of the arc, which could be another galaxy merging with the arc.

Chapter 4: When studying the rest-frame optical emission of a sample of the brightest sources detected in HLS, we learn the following:

- We find that star formation rates derived from the Hα under-predict the star formation rates derived from the far-IR. The "suppression" of Hα in the sample has a median value of $30\times$, which is larger than reported in the literature for galaxies at high redshift. If we assume a magnification factor of $10\times$ for all the sources, they would fall at the LIRG/ULIRG threshold.

- When comparing the Hα derived star formation rates to the far-IR, we find that the median dust attenuation is 3.7$\pm$1.5.

- The N2 derived metallicity in the sample is no different than previous work on dusty, star-forming galaxies with a range of 8.4-9.3.

- One of the sources in the sample has an extreme Hα suppression by a factor of $550\times$ (A$_V \sim 7$). This is similar to the dust attenuations of ULIRGs in the local Universe. While the galaxy appears to contain a weak AGN, from the line ratios, the majority of the far-IR emission appears to come from star formation.

5.2 Future Prospects

5.2.1 Molecular Gas

With ALMA now available for general use, the study of dusty, star-forming galaxies will progress much further on the molecular side. Large samples of typical dusty, star-forming galaxies will eventually have CO measurements. This advancement will be made possible with the sensitivities and resolutions available to ALMA. Previous generation facilities were limited to the brightest sources and much lower redshift sources.

5.2.2 Dust

The *Herschel* Space Observatory was able to for the first time sample the full far-IR SED of dusty, star-forming galaxies at high redshift ($z > 1$). Even with a 3.5m telescope the sensitivity only was able to detect more typical galaxies at redshifts $z < 2$. Beyond, only the brightest sources would be able to be studied.

While ALMA will provide useful constraints on the Rayleigh-Jeans side of the dust emission, because of the atmosphere ALMA will be unable to sample the full far-IR/submm dust emission. Future space missions will be necessary to provide the sensitivity and resolution to advance the field.

5.2.3 Nebular Emission

While 20-30 meter class telescopes will push the detection threshold down significantly, ultimately the limited number of atmospheric windows will limit ground based follow-up of nebular emission lines for dusty, star-forming galaxies. Facilities such as *JWST*/NIRSpec will become necessary to follow-up such high redshift dusty galaxies. Its medium resolution spectroscopy from 1-5 μm would allow the detection of Hα from redshift $z = 0.5 - 6.6$. With the dust attenuations potentially being large for dusty, star-forming galaxies, it may be necessary to investigate weaker Hydrogen series transitions, such as the Paschen or Brackett series. Early work has already been conducted for bright lensed galaxies ($z = 1 - 3$) by Rujopakarn et al. (2012) and

local galaxies ($z < 0.4$) by Shipley et al. (2015), which finds an agreement with star formation rates derived from the Paschen and Brackett series to the far-IR derived star formation rates. JWST will open up the window for studying a complete set of Hydrogen series and we will be able to see if the current conclusions will hold for this even dustier population at high redshift.

Studies of UV selected galaxies suggest that the SFR drops quite significantly, along with the fluxes of the emission lines. In addition, we only have a limited sampling of the number of dusty, star-forming galaxies at high redshift. Large samples from H-ATLAS (Negrello et al., 2010), HerMES (Wardlow et al., 2013) and SPT (Weiß et al., 2013) have pushed the redshift threshold to $z \sim 6$. Even at the highest redshifts there is some evidence for dust, such as HFLS3 at $z = 6.34$ (Riechers et al., 2013) and the recently discovered gravitationally lensed galaxy in the cluster Abell 1689 at $z = 7.5$ (Watson et al., 2015).

APPENDIX A

24 μm Selected Galaxies with Spectroscopic Redshifts

In Tables 2.8 and 2.9 we list the 67 MIPS 24 μm sources in this sample; 61 of which were targeted with Magellan/LDSS-3 and the redshifts for 6 are from the literature Gómez et al. (2012). For 45 of these sources a spectroscopic redshift (Table 2.8) was determined with either one or more emission or absorption features, 27 of which were previously unknown. The emission lines detected are listed in table 6 for the LDSS-3 sample. We adopt similar spectroscopic quality codes as the DEEP2 survey. The redshift quality codes are defined as the following; z_q of 2 is a single emission or absorption feature where the redshift is dubious, z_q of 3 there is a few emission or absorption features where the redshift is secure, and a z_q of 4 several emission and absorption features and the redshift is very secure.

Figure 2.12 shows the positions of the galaxies from our sample and the Gómez et al. (2012) sample. From the spectroscopic sample of 45 galaxies we find that 27 are background galaxies, 15 are cluster members and 4 are foreground galaxies. For one of the sources the correct counterpart is ambiguous, there are two galaxies within 1.58″ of each other and they both fall within the LDSS-3 slit. Based on the distance from the optical counterparts to the 24 μm source, the lower redshift galaxy ($z = 0.474$) appears to be the more likely candidate of the 24 μm emission. Of the 26 background galaxies; 9 have redshifts $z > 1$, one of which is within the central arcmin of the cluster center. Of the 27 galaxies with previously unknown redshifts, 22 of the galaxies are found in the background of the cluster.

We also identify 5 galaxies at redshift $z \sim 0.6$, one of which is discovered in Gómez et al. (2012). The distance between these galaxies and AS1063a are 260, 540 and 1110 kpc. This study, Gómez et al. (2012) and Karman et al. (2015) identify 6 galaxies at $z \sim 0.6$ all within 2.4′ of each other and a Δv of 2400 km/s (5 within 1.4′and with Δv of 370 km/s). Gruen et al. (2013) uses weak lensing to suggest

that there is a background cluster at $z \sim 0.6$, offset by $14.5'$ from AS1063. This could potentially be an infalling group, however this is speculative, more wide field spectroscopy is needed to determine the size and structure of the background cluster at $z \sim 0.6$

APPENDIX B

HLS Bright Sources

Here we go into greater detail about the bright *Herschel* sources targeted in this sample. The sources typically have a peak flux $S_{peak} > 100$ mJy and color $S_{500}/S_{250} > 0.4$, see Egami et al. 2015 in prep. Hα fluxes for two of bright sources come from the literature; HLSJ2248 (Walth et al. 2015a in prep) and HLSJ2043 (Nakajima et al. 2015 in prep).

HLSJ003208.2+180644 – Dessauges-Zavadsky et al. 2015 in prep report the detection of the *Herschel* bright source ($S_{peak} = 128$ mJy) in the cluster MACSJ0032.1+1808. IRAM 30m observations of CO place the redshift of the source at $z = 3.628$. *HST*/ACS F606W and F814W imaging reveals 3 arcs near the position of the *Herschel*/SPIRE 250 flux peak. The arcs are 1.4′ SW from the cluster center. The lens model suggests that the arcs are a set of 5 images, with the critical line passing through the central arc (where the two images blend together). Morphologically each image has two bright spots with a gap between them. The colors of the bright spots suggest they could be two separate galaxies. LBT/LUCI K-band observations of the *Herschel* source detect Hβ and [OIII] for 3 of the images. The fifth image was not targeted. The central arc shows velocity structures for both images which mirror each other and merge at the center, where the critical line passes through the central arc.

HLSJ004335.4-204200 – A bright *Herschel* source ($S_{peak} = 166$ mJy) found 5.4′ SE of the cluster Abell 2813. Imaging evidence suggests that the source is galaxy-galaxy lensed. Two sources are seen in *Spitzer*/IRAC [3.6] and [4.5] imaging, separated by 2″, with the southern source having redder colors. Magellan/IMACS imaging only detects the northern source, which appears to be an elliptical galaxy. JVLA 4-8 GHz imaging reveals the background galaxy at the position of the southern IRAC source and a possible counter-image north (1.2″) of the northern source. Interestingly, the

northern source appears to have a radio jet. LBT/LUCI observations are unable to detect any lines with the HK grating with 0.4-0.6″ seeing. SED fitting to the *Herschel* photometry suggest a redshift of $z = 2.0$.

HLSJ011127.7+085529 – A bright *Herschel* ($S_{peak} = 95$ mJy) source detected in the cluster MACSJ0111.5+0855. IRAC [3.6] and [4.5] imaging reveals two red sources at the position of the *Herschel*/SPIRE flux peak, located 1′ W of the cluster center. The southern source is fainter and redder (less [3.6] micron flux) than the northern source. The sources are undetected in SDSS images. JVLA 4-8 GHz continuum imaging detects both sources. The southern source is $\sim$3× brighter than the northern source with no distinguishable morphology. The northern source appears to have a bright spot with two lobes; one each on the north and south side of the source. We targeted both sources with LBT/LUCI near-IR spectroscopy with the HK grating. We detect Hα and [NII] in the northern source at redshift $z = 2.268$. No line is detected for the southern source.

HLSJ045518.0+070103 – Zavala et al. 2015 report the detection of a single CO line at 88.051 GHz for the bright *Herschel* source ($S_{peak} = 139$ mJy) in the field of the cluster MACSJ0455.2+0657. Possible redshift solutions to this source are $z =1.618$, 2.927, and 4.236. Zavala et al. 2015 rule out the $z = 4.236$ solution based on the non-detection of the CO(5-4) line at 110.1 GHz. The galaxy is 3.1′ from the cluster core and is possibly galaxy-galaxy lensed. LBT/MODS g and r band imaging reveals two sources at the position of the *Herschel*/SPIRE 250 μm flux peak. The southern source has redder colors than the northern source which is also seen in *Spitzer*/IRAC [3.6] and [4.5]. It is unclear which source is the lens. Assuming the northern source is the lens and the southern source is the *Herschel* counterpart, the southern source is targeted for near-IR spectroscopy. LBT/LUCI observations were unable to detect Hα in the H-band after 3.3 hours of integration with seeing 0.5″.

HLSJ080057.9+361413 – Rujopakarn et al. 2015 in prep report the discovery of bright *Herschel* source ($S_{peak} = 317$ mJy) which is a galaxy-galaxy lensed system at redshift $z = 1.885$ (from CO). The *Herschel* source is $\sim$10.8′ N of the cluster core of Abell 611. JVLA 4-8 GHz imaging reveals that the background galaxy appears

as a ring-like structure. The background galaxy is detected in *HST*/F105W and F140W images after subtracting the lens from the image. LBT/LUCI observations are unable to detect the [OII] doublet in the zJ band after 4.3 hours of integration with seeing 0.3-0.8″ and subtracting off the continuum from the lens. The slit was placed on the brightest knots in the JVLA image.

HLSJ091828.6+514223 – Combes et al. (2012) reported the discovery of this galaxy at redshift $z = 5.24$ and peak flux of $S_{peak} = 226$ mJy. It is the highest redshift galaxy found to date in HLS and it is a galaxy-galaxy lensed system found 5.7′ outside the cluster core of Abell 773. Ground based optical/near-IR imaging only reveal the lens, the background galaxy is undetected. CO observations with IRAM 30m and JVLA detect 4 individual velocity structures (Combes et al., 2012). Continuum observation with the SMA detect a ring-like structure (Rawle et al., 2014). There is evidence that some of the structures may contain an AGN. The lens model predicts a magnification of 8.9×. LBT/LUCI observations are unable to detect the [OII] doublet in the K-band after 3 hours of integration with seeing 0.3-0.5″ and subtracting off the continuum of the lens. The slit was aligned along the bright knots from the SMA image.

HLSJ094303.6+470058 – A bright *Herschel* source ($S_{peak} = 120$ mJy) detected in the field of Abell 851, which is ∼2′ from the cluster center. *Spitzer*/IRAC imaging shows 4 sources at the position of the *Herschel*/SPIRE 250 μm source, with the left and right sources separated by about 14″ (shown in top-right panel of Figure 4.2). *Spitzer*/MIPS 24 μm imaging reveals flux from the left, right and bottom sources, with the majority of the flux coming from the left and right sources. In *Herschel*/SPIRE the bottom and right sources blend together with the majority of the flux is coming from them. The centroid of *Herschel*/SPIRE 250 μm source matches the position of the bottom source. *HST*/WFPC2 F702W imaging detect the left, top and right sources, the bottom source is undetected. In addition, The right source's IRAC centroid is offset by 0.5″ from the *HST* position, suggesting the optical emission could mostly be obscured. IRAM 30m observations detect multiple CO lines which place the redshift of the *Herschel* source at $z = 1.65$. Further investigation

reveals that the left and top sources are cluster members at redshifts 0.3960 and 0.3958 respectively. LBT/LUCI observations targeted the bottom source and detect Hα and [NII] at the CO redshift of $z = 1.65$. The right source's redshift is unknown.

HLSJ122659.9+333235 – Clement et al. 2015 in prep report the discovery of a bright *Herschel* source ($S_{peak} = 111$ mJy) in the cluster CLJ1226.9+3332. *Spitzer*/MIPS 24 μm images show that the *Herschel*/SPIRE 250 μm source split into two individual sources. At the position of the top *Spitzer*/MIPS 24 μm source, *HST*/WFC3 imaging reveals 3 bright star forming knots, which appear to be located at the bottom of a large ($\sim$18″) red arc (23″ SE of the cluster center). The bottom *Spitzer*/MIPS 24 μm source appears to be associated with another large red galaxy that is 10″ S of the large red arc. LBT/LUCI near-IR spectroscopy targeted the bright star forming knots and found the redshift was at $z = 2.265$. Hα and [NII] were detected for all three knots, though the spatial resolution of LUCI blends the top two knots together. Additional LUCI observations also confirm the redshift of the large arc is the same as the star forming knots. The redshift of the southern red galaxy is unknown.

HLSJ131421.4-251548 – A cluster lensed *Herschel* source ($S_{peak} = 165$ mJy) found in the cluster MACSJ1314.3-2515. IRAM 30m detects multiple CO lines placing the redshift at $z = 1.447$. Near-IR UKIRT/WFCAM and IRAC images (Figure 4.5) show a large red arc (8″) at the position of the *Herschel*/SPIRE 250 μm peak. The arc is 11″ away from the cluster center. JVLA 4-8 GHz observations of the arc reveal a clump at the central location with two tentative detections of clumps at the edges. Preliminary evaluation of the lensing configuration suggests that the arc may be a singly imaged system, with no evidence for counterparts. The bright star forming region found in the JVLA continuum image (which also corresponds to bright spot in near-IR) was targeted for near-IR spectroscopy with Magellan/FIRE. Hα and [NII] are detected in the arc (Figure 4.6). In addition, continuum for the galaxy is also detected.

HLSJ204314.2-214439 – One of the brightest sources detected in HLS, with peak flux density of $S_{peak} = 300$ mJy, which is gravitationally lensed by the cluster

RXCJ2043.2-2144. Zavala et al. 2015 shows it is a blend of 3 galaxies at redshifts $z = 2.041$, 3.252 and 4.68. High resolution SMA data show that the galaxy at $z = 4.68$ is a triply lensed and the galaxy at $z = 2.041$ is a large arc (Walth et al. 2015b). The $z = 3.252$ galaxy is undetected in the SMA image. UKIRT/WFCAM K-band imaging reveals the $z = 2.041$ arc seen in the SMA image. Deblending the far-IR/submm fluxes we find that the $z = 2.041$ galaxy has a peak flux density of $S_{peak} = 194$ mJy. The $z = 2.041$ galaxy is $8''$ from the BCG and the lens model predicts a magnification of $7.87\times$. VLT/SINFONI near-IR spectroscopy detect Hα with a $0.2''$ spatial offset from the SMA arc and measure of a flux of 1.1×10^{16} erg/s/cm^2 (Nakajima et al. 2015 in prep).

HLSJ224841.8-443157 – A gravitationally lensed *Herschel* source detected in the cluster AS1063, $24''$ from the cluster center, at redshift $z = 0.61$ (Gómez et al., 2012). Identified as a *Herschel* source by Walth et al. 2015a in prep with peak flux density of $S_{peak} = 100$ mJy and SPIRE color of S$_{500}$/S$_{250}$=0.3. The lens model suggests the galaxy has a magnification of $3.69\times$. The galaxy is clearly detected in *HST*/ACS and WFC3. Multiple Balmer lines (Hβ–H8) are detected in the optical with Magellan/LDSS3 and Hα is detect in the near-IR with Magellan/MMIRS. We measure a visual extinction of A$_V$ = 1.23 mag using the Hβ/Hδ ratio. What is striking is the galaxy appears to have a large luminous HII region a kpc in diameter with a SFR of 10 M$_\odot$/yr.

REFERENCES

Antonucci, R. (1993). Unified models for active galactic nuclei and quasars. *ARA&A*, **31**, pp. 473–521. doi:10.1146/annurev.aa.31.090193.002353.

Arnouts, S., S. Cristiani, L. Moscardini, S. Matarrese, F. Lucchin, A. Fontana, and E. Giallongo (1999). Measuring and modelling the redshift evolution of clustering: the Hubble Deep Field North. *MNRAS*, **310**, pp. 540–556. doi:10.1046/j.1365-8711.1999.02978.x.

Balestra, I., E. Vanzella, P. Rosati, A. Monna, C. Grillo, M. Nonino, A. Mercurio, A. Biviano, L. Bradley, D. Coe, A. Fritz, M. Postman, S. Seitz, M. Scodeggio, P. Tozzi, W. Zheng, B. Ziegler, A. Zitrin, M. Annunziatella, M. Bartelmann, N. Benitez, T. Broadhurst, R. Bouwens, O. Czoske, M. Donahue, H. Ford, M. Girardi, L. Infante, S. Jouvel, D. Kelson, A. Koekemoer, U. Kuchner, D. Lemze, M. Lombardi, C. Maier, E. Medezinski, P. Melchior, M. Meneghetti, J. Merten, A. Molino, L. Moustakas, V. Presotto, R. Smit, and K. Umetsu (2013). CLASH-VLT: spectroscopic confirmation of a z = 6.11 quintuply lensed galaxy in the Frontier Fields cluster RXC J2248.7-4431. *A&A*, **559**, L9. doi:10.1051/0004-6361/201322620.

Becker, G. D., M. Rauch, and W. L. W. Sargent (2009). High-Redshift Metals. I. The Decline of C IV at z > 5.3. *ApJ*, **698**, pp. 1010–1019. doi:10.1088/0004-637X/698/2/1010.

Bertin, E. and S. Arnouts (1996). SExtractor: Software for source extraction. *A&AS*, **117**, pp. 393–404. doi:10.1051/aas:1996164.

Bian, F., X. Fan, J. Bechtold, I. D. McGreer, D. W. Just, D. J. Sand, R. F. Green, D. Thompson, C. Y. Peng, W. Seifert, N. Ageorges, M. Juette, V. Knierim, and P. Buschkamp (2010). LBT/LUCIFER Observations of the z ˜ 2 Lensed Galaxy J0900+2234. *ApJ*, **725**, pp. 1877–1885. doi:10.1088/0004-637X/725/2/1877.

Bian, F., D. P. Stark, X. Fan, L. Jiang, B. Clément, E. Egami, B. Frye, R. F. Green, I. D. McGreer, and Z. Cai (2015). LBT/LUCI Spectroscopic Observations of z≃7 Galaxies. *ApJ*, **806**, 108. doi:10.1088/0004-637X/806/1/108.

Blain, A. W. (1999). The differential magnification of high-redshift ultraluminous infrared galaxies. *MNRAS*, **304**, pp. 669–673. doi:10.1046/j.1365-8711.1999.02426.x.

Blain, A. W., V. E. Barnard, and S. C. Chapman (2003). Submillimetre and far-infrared spectral energy distributions of galaxies: the luminosity-temperature relation and consequences for photometric redshifts. *MNRAS*, **338**, pp. 733–744. doi:10.1046/j.1365-8711.2003.06086.x.

Böhringer, H., P. Schuecker, L. Guzzo, C. A. Collins, W. Voges, R. G. Cruddace, A. Ortiz-Gil, G. Chincarini, S. De Grandi, A. C. Edge, H. T. MacGillivray, D. M. Neumann, S. Schindler, and P. Shaver (2004). The ROSAT-ESO Flux Limited X-ray (REFLEX) Galaxy cluster survey. V. The cluster catalogue. *A&A*, **425**, pp. 367–383. doi:10.1051/0004-6361:20034484.

Bolatto, A. D., M. Wolfire, and A. K. Leroy (2013). The CO-to-H_2 Conversion Factor. *ARA&A*, **51**, pp. 207–268. doi:10.1146/annurev-astro-082812-140944.

Boone, F., B. Clément, J. Richard, D. Schaerer, D. Lutz, A. Weiß, M. Zemcov, E. Egami, T. D. Rawle, G. L. Walth, J.-P. Kneib, F. Combes, I. Smail, A. M. Swinbank, B. Altieri, A. W. Blain, S. Chapman, M. Dessauges-Zavadsky, R. J. Ivison, K. K. Knudsen, A. Omont, R. Pelló, P. G. Pérez-González, I. Valtchanov, P. van der Werf, and M. Zamojski (2013). An extended Herschel drop-out source in the center of AS1063: a normal dusty galaxy at z = 6.1 or SZ substructures? *A&A*, **559**, L1. doi:10.1051/0004-6361/201322552.

Bothwell, M. S., I. Smail, S. C. Chapman, R. Genzel, R. J. Ivison, L. J. Tacconi, S. Alaghband-Zadeh, F. Bertoldi, A. W. Blain, C. M. Casey, P. Cox, T. R. Greve, D. Lutz, R. Neri, A. Omont, and A. M. Swinbank (2013). A survey of molecular gas in luminous sub-millimetre galaxies. *MNRAS*, **429**, pp. 3047–3067. doi:10.1093/mnras/sts562.

Bradford, C. M., J. E. Aguirre, R. Aikin, J. J. Bock, L. Earle, J. Glenn, H. Inami, P. R. Maloney, H. Matsuhara, B. J. Naylor, H. T. Nguyen, and J. Zmuidzinas (2009). The Warm Molecular Gas around the Cloverleaf Quasar. *ApJ*, **705**, pp. 112–122. doi:10.1088/0004-637X/705/1/112.

Bruzual, G. and S. Charlot (2003). Stellar population synthesis at the resolution of 2003. *MNRAS*, **344**, pp. 1000–1028. doi:10.1046/j.1365-8711.2003.06897.x.

Caputi, K. I., G. Lagache, L. Yan, H. Dole, N. Bavouzet, E. Le Floc'h, P. I. Choi, G. Helou, and N. Reddy (2007). The Infrared Luminosity Function of Galaxies at Redshifts z = 1 and z ˜ 2 in the GOODS Fields. *ApJ*, **660**, pp. 97–116. doi:10.1086/512667.

Carilli, C. L. and F. Walter (2013). Cool Gas in High-Redshift Galaxies. *ARA&A*, **51**, pp. 105–161. doi:10.1146/annurev-astro-082812-140953.

Casey, C. M., S. Berta, M. Béthermin, J. Bock, C. Bridge, J. Budynkiewicz, D. Burgarella, E. Chapin, S. C. Chapman, D. L. Clements, A. Conley, C. J. Conselice, A. Cooray, D. Farrah, E. Hatziminaoglou, R. J. Ivison, E. le Floc'h, D. Lutz, G. Magdis, B. Magnelli, S. J. Oliver, M. J. Page, F. Pozzi, D. Rigopoulou, L. Riguccini, I. G. Roseboom, D. B. Sanders, D. Scott, N. Seymour, I. Valtchanov, J. D. Vieira, M. Viero, and J. Wardlow (2012a). A Redshift Survey of Herschel Far-infrared Selected Starbursts and Implications for Obscured Star Formation. *ApJ*, **761**, 140. doi:10.1088/0004-637X/761/2/140.

Casey, C. M., S. Berta, M. Béthermin, J. Bock, C. Bridge, D. Burgarella, E. Chapin, S. C. Chapman, D. L. Clements, A. Conley, C. J. Conselice, A. Cooray, D. Farrah, E. Hatziminaoglou, R. J. Ivison, E. le Floc'h, D. Lutz, G. Magdis, B. Magnelli, S. J. Oliver, M. J. Page, F. Pozzi, D. Rigopoulou, L. Riguccini, I. G. Roseboom, D. B. Sanders, D. Scott, N. Seymour, I. Valtchanov, J. D. Vieira, M. Viero, and J. Wardlow (2012b). A Population of z > 2 Far-infrared Herschel-SPIRE-selected Starbursts. *ApJ*, **761**, 139. doi:10.1088/0004-637X/761/2/139.

Casey, C. M., D. Narayanan, and A. Cooray (2014). Dusty star-forming galaxies at high redshift. *Phys. Rep.*, **541**, pp. 45–161. doi:10.1016/j.physrep.2014.02.009.

Chary, R. and D. Elbaz (2001). Interpreting the Cosmic Infrared Background: Constraints on the Evolution of the Dust-enshrouded Star Formation Rate. *ApJ*, **556**, pp. 562–581. doi:10.1086/321609.

Combes, F., M. Rex, T. D. Rawle, E. Egami, F. Boone, I. Smail, J. Richard, R. J. Ivison, M. Gurwell, C. M. Casey, A. Omont, A. Berciano Alba, M. Dessauges-Zavadsky, A. C. Edge, G. G. Fazio, J.-P. Kneib, N. Okabe, R. Pelló, P. G. Pérez-González, D. Schaerer, G. P. Smith, A. M. Swinbank, and P. van der Werf (2012). A bright z = 5.2 lensed submillimeter galaxy in the field of Abell 773. HLSJ091828.6+514223. *A&A*, **538**, L4. doi:10.1051/0004-6361/201118750.

Courteau, S. (1997). Optical Rotation Curves and Linewidths for Tully-Fisher Applications. *AJ*, **114**, p. 2402. doi:10.1086/118656.

Cowie, L. L., E. M. Hu, and A. Songaila (1995). Faintest Galaxy Morphologies From HST WFPC2 Imaging of the Hawaii Survey Fields. *AJ*, **110**, p. 1576. doi:10.1086/117631.

Cox, P., M. Krips, R. Neri, A. Omont, R. Güsten, K. M. Menten, F. Wyrowski, A. Weiß, A. Beelen, M. A. Gurwell, H. Dannerbauer, R. J. Ivison, M. Negrello, I. Aretxaga, D. H. Hughes, R. Auld, M. Baes, R. Blundell, S. Buttiglione, A. Cava, A. Cooray, A. Dariush, L. Dunne, S. Dye, S. A. Eales, D. Frayer, J. Fritz, R. Gavazzi, R. Hopwood, E. Ibar, M. Jarvis, S. Maddox, M. Michałowski, E. Pascale, M. Pohlen, E. Rigby, D. J. B. Smith, A. M. Swinbank, P. Temi, I. Valtchanov,

P. van der Werf, and G. de Zotti (2011). Gas and Dust in a Submillimeter Galaxy at z = 4.24 from the Herschel Atlas. *ApJ*, **740**, 63. doi:10.1088/0004-637X/740/2/63.

da Cunha, E., B. Groves, F. Walter, R. Decarli, A. Weiss, F. Bertoldi, C. Carilli, E. Daddi, D. Elbaz, R. Ivison, R. Maiolino, D. Riechers, H.-W. Rix, M. Sargent, and I. Smail (2013). On the Effect of the Cosmic Microwave Background in High-redshift (Sub-)millimeter Observations. *ApJ*, **766**, 13. doi:10.1088/0004-637X/766/1/13.

Daddi, E., F. Bournaud, F. Walter, H. Dannerbauer, C. L. Carilli, M. Dickinson, D. Elbaz, G. E. Morrison, D. Riechers, M. Onodera, F. Salmi, M. Krips, and D. Stern (2010). Very High Gas Fractions and Extended Gas Reservoirs in z = 1.5 Disk Galaxies. *ApJ*, **713**, pp. 686–707. doi:10.1088/0004-637X/713/1/686.

Danielson, A. L. R., A. M. Swinbank, I. Smail, E. Bayet, P. P. van der Werf, P. Cox, A. C. Edge, C. Henkel, and R. J. Ivison (2013). ^{13}CO and C^{18}O emission from a dense gas disc at z = 2.3: abundance variations, cosmic rays and the initial conditions for star formation. *MNRAS*, **436**, pp. 2793–2809. doi:10.1093/mnras/stt1775.

De Breuck, C., R. Maiolino, P. Caselli, K. Coppin, S. Hailey-Dunsheath, and T. Nagao (2011). Enhanced [CII] emission in a z = 4.76 submillimetre galaxy. *A&A*, **530**, L8. doi:10.1051/0004-6361/201116868.

Dekel, A., R. Sari, and D. Ceverino (2009). Formation of Massive Galaxies at High Redshift: Cold Streams, Clumpy Disks, and Compact Spheroids. *ApJ*, **703**, pp. 785–801. doi:10.1088/0004-637X/703/1/785.

Dressler, A., B. Bigelow, T. Hare, B. Sutin, I. Thompson, G. Burley, H. Epps, A. Oemler, A. Bagish, C. Birk, K. Clardy, S. Gunnels, D. Kelson, S. Shectman, and D. Osip (2011). IMACS: The Inamori-Magellan Areal Camera and Spectrograph on Magellan-Baade. *PASP*, **123**, pp. 288–332. doi:10.1086/658908.

Egami, E., G. Neugebauer, B. T. Soifer, K. Matthews, M. Ressler, E. E. Becklin, T. W. Murphy, Jr., and D. A. Dale (2000). APM 08279+5255: Keck Near- and Mid-Infrared High-Resolution Imaging. *ApJ*, **535**, pp. 561–574. doi:10.1086/308862.

Egami, E., M. Rex, T. D. Rawle, P. G. Pérez-González, J. Richard, J.-P. Kneib, D. Schaerer, B. Altieri, I. Valtchanov, A. W. Blain, D. Fadda, M. Zemcov, J. J. Bock, F. Boone, C. R. Bridge, B. Clement, F. Combes, M. Dessauges-Zavadsky, C. D. Dowell, O. Ilbert, R. J. Ivison, M. Jauzac, D. Lutz, L. Metcalfe, A. Omont, R. Pelló, M. J. Pereira, G. H. Rieke, G. Rodighiero, I. Smail, G. P. Smith, G. Tramoy, G. L. Walth, P. van der Werf, and M. W. Werner

(2010). The Herschel Lensing Survey (HLS): Overview. *A&A*, **518**, L12. doi:10.1051/0004-6361/201014696.

Elmegreen, D. M., B. G. Elmegreen, and A. C. Hirst (2004a). Discovery of Face-on Counterparts of Chain Galaxies in the Tadpole Advanced Camera for Surveys Field. *ApJ*, **604**, pp. L21–L23. doi:10.1086/383312.

Elmegreen, D. M., B. G. Elmegreen, and C. M. Sheets (2004b). Chain Galaxies in the Tadpole Advanced Camera for Surveys Field. *ApJ*, **603**, pp. 74–81. doi:10.1086/381357.

Erb, D. K., C. C. Steidel, A. E. Shapley, M. Pettini, N. A. Reddy, and K. L. Adelberger (2006). Hα Observations of a Large Sample of Galaxies at z ~ 2: Implications for Star Formation in High-Redshift Galaxies. *ApJ*, **647**, pp. 128–139. doi:10.1086/505341.

Fazio, G. G., J. L. Hora, L. E. Allen, M. L. N. Ashby, P. Barmby, L. K. Deutsch, J.-S. Huang, S. Kleiner, M. Marengo, S. T. Megeath, G. J. Melnick, M. A. Pahre, B. M. Patten, J. Polizotti, H. A. Smith, R. S. Taylor, Z. Wang, S. P. Willner, W. F. Hoffmann, J. L. Pipher, W. J. Forrest, C. W. McMurty, C. R. McCreight, M. E. McKelvey, R. E. McMurray, D. G. Koch, S. H. Moseley, R. G. Arendt, J. E. Mentzell, C. T. Marx, P. Losch, P. Mayman, W. Eichhorn, D. Krebs, M. Jhabvala, D. Y. Gezari, D. J. Fixsen, J. Flores, K. Shakoorzadeh, R. Jungo, C. Hakun, L. Workman, G. Karpati, R. Kichak, R. Whitley, S. Mann, E. V. Tollestrup, P. Eisenhardt, D. Stern, V. Gorjian, B. Bhattacharya, S. Carey, B. O. Nelson, W. J. Glaccum, M. Lacy, P. J. Lowrance, S. Laine, W. T. Reach, J. A. Stauffer, J. A. Surace, G. Wilson, E. L. Wright, A. Hoffman, G. Domingo, and M. Cohen (2004). The Infrared Array Camera (IRAC) for the Spitzer Space Telescope. *ApJS*, **154**, pp. 10–17. doi:10.1086/422843.

Förster Schreiber, N. M., R. Genzel, N. Bouché, G. Cresci, R. Davies, P. Buschkamp, K. Shapiro, L. J. Tacconi, E. K. S. Hicks, S. Genel, A. E. Shapley, D. K. Erb, C. C. Steidel, D. Lutz, F. Eisenhauer, S. Gillessen, A. Sternberg, A. Renzini, A. Cimatti, E. Daddi, J. Kurk, S. Lilly, X. Kong, M. D. Lehnert, N. Nesvadba, A. Verma, H. McCracken, N. Arimoto, M. Mignoli, and M. Onodera (2009). The SINS Survey: SINFONI Integral Field Spectroscopy of z ~ 2 Star-forming Galaxies. *ApJ*, **706**, pp. 1364–1428. doi:10.1088/0004-637X/706/2/1364.

Förster Schreiber, N. M., A. E. Shapley, D. K. Erb, R. Genzel, C. C. Steidel, N. Bouché, G. Cresci, and R. Davies (2011a). Constraints on the Assembly and Dynamics of Galaxies. I. Detailed Rest-frame Optical Morphologies on Kiloparsec Scale of z ~ 2 Star-forming Galaxies. *ApJ*, **731**, 65. doi:10.1088/0004-637X/731/1/65.

Förster Schreiber, N. M., A. E. Shapley, R. Genzel, N. Bouché, G. Cresci, R. Davies, D. K. Erb, S. Genel, D. Lutz, S. Newman, K. L. Shapiro, C. C. Steidel, A. Sternberg, and L. J. Tacconi (2011b). Constraints on the Assembly and Dynamics of Galaxies. II. Properties of Kiloparsec-scale Clumps in Rest-frame Optical Emission of z ˜ 2 Star-forming Galaxies. *ApJ*, **739**, 45. doi:10.1088/0004-637X/739/1/45.

French, K. D., Y. Yang, A. Zabludoff, D. Narayanan, Y. Shirley, F. Walter, J.-D. Smith, and C. A. Tremonti (2015). Discovery of Large Molecular Gas Reservoirs in Post-starburst Galaxies. *ApJ*, **801**, 1. doi:10.1088/0004-637X/801/1/1.

Frye, B. L., M. Hurley, D. V. Bowen, G. Meurer, K. Sharon, A. Straughn, D. Coe, T. Broadhurst, and P. Guhathakurta (2012). Spatially Resolved HST Grism Spectroscopy of a Lensed Emission Line Galaxy at z ˜ 1. *ApJ*, **754**, 17. doi:10.1088/0004-637X/754/1/17.

Geach, J. E., R. C. Hickox, A. M. Diamond-Stanic, M. Krips, G. H. Rudnick, C. A. Tremonti, P. H. Sell, A. L. Coil, and J. Moustakas (2014). Stellar feedback as the origin of an extended molecular outflow in a starburst galaxy. *Nature*, **516**, pp. 68–70. doi:10.1038/nature14012.

Geach, J. E., I. Smail, S. M. Moran, L. A. MacArthur, C. d. P. Lagos, and A. C. Edge (2011). On the Evolution of the Molecular Gas Fraction of Star-Forming Galaxies. *ApJ*, **730**, L19. doi:10.1088/2041-8205/730/2/L19.

Genzel, R., S. Newman, T. Jones, N. M. Förster Schreiber, K. Shapiro, S. Genel, S. J. Lilly, A. Renzini, L. J. Tacconi, N. Bouché, A. Burkert, G. Cresci, P. Buschkamp, C. M. Carollo, D. Ceverino, R. Davies, A. Dekel, F. Eisenhauer, E. Hicks, J. Kurk, D. Lutz, C. Mancini, T. Naab, Y. Peng, A. Sternberg, D. Vergani, and G. Zamorani (2011). The Sins Survey of z ˜ 2 Galaxy Kinematics: Properties of the Giant Star-forming Clumps. *ApJ*, **733**, 101. doi:10.1088/0004-637X/733/2/101.

Genzel, R., L. J. Tacconi, J. Gracia-Carpio, A. Sternberg, M. C. Cooper, K. Shapiro, A. Bolatto, N. Bouché, F. Bournaud, A. Burkert, F. Combes, J. Comerford, P. Cox, M. Davis, N. M. F. Schreiber, S. Garcia-Burillo, D. Lutz, T. Naab, R. Neri, A. Omont, A. Shapley, and B. Weiner (2010). A study of the gas-star formation relation over cosmic time. *MNRAS*, **407**, pp. 2091–2108. doi:10.1111/j.1365-2966.2010.16969.x.

Genzel, R., L. J. Tacconi, D. Lutz, A. Saintonge, S. Berta, B. Magnelli, F. Combes, S. García-Burillo, R. Neri, A. Bolatto, T. Contini, S. Lilly, J. Boissier, F. Boone, N. Bouché, F. Bournaud, A. Burkert, M. Carollo, L. Colina, M. C. Cooper, P. Cox, C. Feruglio, N. M. Förster Schreiber, J. Freundlich, J. Gracia-Carpio, S. Juneau, K. Kovac, M. Lippa, T. Naab, P. Salome, A. Renzini, A. Sternberg, F. Walter, B. Weiner, A. Weiss, and S. Wuyts (2015). Combined CO and

Dust Scaling Relations of Depletion Time and Molecular Gas Fractions with Cosmic Time, Specific Star-formation Rate, and Stellar Mass. *ApJ*, **800**, 20. doi: 10.1088/0004-637X/800/1/20.

Gómez, P. L., L. E. Valkonen, A. K. Romer, E. Lloyd-Davies, T. Verdugo, C. M. Cantalupo, M. D. Daub, J. H. Goldstein, C. L. Kuo, A. E. Lange, M. Lueker, W. L. Holzapfel, J. B. Peterson, J. Ruhl, M. C. Runyan, C. L. Reichardt, and K. Sabirli (2012). Optical and X-Ray Observations of the Merging Cluster AS1063. *AJ*, **144**, 79. doi:10.1088/0004-6256/144/3/79.

Greve, T. R., J. D. Vieira, A. Weiß, J. E. Aguirre, K. A. Aird, M. L. N. Ashby, B. A. Benson, L. E. Bleem, C. M. Bradford, M. Brodwin, J. E. Carlstrom, C. L. Chang, S. C. Chapman, T. M. Crawford, C. de Breuck, T. de Haan, M. A. Dobbs, T. Downes, C. D. Fassnacht, G. Fazio, E. M. George, M. Gladders, A. H. Gonzalez, N. W. Halverson, Y. Hezaveh, F. W. High, G. P. Holder, W. L. Holzapfel, S. Hoover, J. D. Hrubes, M. Johnson, R. Keisler, L. Knox, A. T. Lee, E. M. Leitch, M. Lueker, D. Luong-Van, M. Malkan, D. P. Marrone, V. McIntyre, J. J. McMahon, J. Mehl, K. M. Menten, S. S. Meyer, T. Montroy, E. J. Murphy, T. Natoli, S. Padin, T. Plagge, C. Pryke, C. L. Reichardt, A. Rest, M. Rosenman, J. Ruel, J. E. Ruhl, K. K. Schaffer, K. Sharon, L. Shaw, E. Shirokoff, B. Stalder, S. A. Stanford, Z. Staniszewski, A. A. Stark, K. Story, K. Vanderlinde, W. Walsh, N. Welikala, and R. Williamson (2012). Submillimeter Observations of Millimeter Bright Galaxies Discovered by the South Pole Telescope. *ApJ*, **756**, 101. doi: 10.1088/0004-637X/756/1/101.

Griffin, M. J., A. Abergel, A. Abreu, P. A. R. Ade, P. André, J.-L. Augueres, T. Babbedge, Y. Bae, T. Baillie, J.-P. Baluteau, M. J. Barlow, G. Bendo, D. Benielli, J. J. Bock, P. Bonhomme, D. Brisbin, C. Brockley-Blatt, M. Caldwell, C. Cara, N. Castro-Rodriguez, R. Cerulli, P. Chanial, S. Chen, E. Clark, D. L. Clements, L. Clerc, J. Coker, D. Communal, L. Conversi, P. Cox, D. Crumb, C. Cunningham, F. Daly, G. R. Davis, P. de Antoni, J. Delderfield, N. Devin, A. di Giorgio, I. Didschuns, K. Dohlen, M. Donati, A. Dowell, C. D. Dowell, L. Duband, L. Dumaye, R. J. Emery, M. Ferlet, D. Ferrand, J. Fontignie, M. Fox, A. Franceschini, M. Frerking, T. Fulton, J. Garcia, R. Gastaud, W. K. Gear, J. Glenn, A. Goizel, D. K. Griffin, T. Grundy, S. Guest, L. Guillemet, P. C. Hargrave, M. Harwit, P. Hastings, E. Hatziminaoglou, M. Herman, B. Hinde, V. Hristov, M. Huang, P. Imhof, K. J. Isaak, U. Israelsson, R. J. Ivison, D. Jennings, B. Kiernan, K. J. King, A. E. Lange, W. Latter, G. Laurent, P. Laurent, S. J. Leeks, E. Lellouch, L. Levenson, B. Li, J. Li, J. Lilienthal, T. Lim, S. J. Liu, N. Lu, S. Madden, G. Mainetti, P. Marliani, D. McKay, K. Mercier, S. Molinari, H. Morris, H. Moseley, J. Mulder, M. Mur, D. A. Naylor, H. Nguyen, B. O'Halloran, S. Oliver, G. Olofsson, H.-G. Olofsson, R. Orfei, M. J. Page, I. Pain, P. Panuzzo, A. Papageorgiou, G. Parks, P. Parr-Burman, A. Pearce, C. Pearson, I. Pérez-

Fournon, F. Pinsard, G. Pisano, J. Podosek, M. Pohlen, E. T. Polehampton, D. Pouliquen, D. Rigopoulou, D. Rizzo, I. G. Roseboom, H. Roussel, M. Rowan-Robinson, B. Rownd, P. Saraceno, M. Sauvage, R. Savage, G. Savini, E. Sawyer, C. Scharmberg, D. Schmitt, N. Schneider, B. Schulz, A. Schwartz, R. Shafer, D. L. Shupe, B. Sibthorpe, S. Sidher, A. Smith, A. J. Smith, D. Smith, L. Spencer, B. Stobie, R. Sudiwala, K. Sukhatme, C. Surace, J. A. Stevens, B. M. Swinyard, M. Trichas, T. Tourette, H. Triou, S. Tseng, C. Tucker, A. Turner, M. Vaccari, I. Valtchanov, L. Vigroux, E. Virique, G. Voellmer, H. Walker, R. Ward, T. Waskett, M. Weilert, R. Wesson, G. J. White, N. Whitehouse, C. D. Wilson, B. Winter, A. L. Woodcraft, G. S. Wright, C. K. Xu, A. Zavagno, M. Zemcov, L. Zhang, and E. Zonca (2010). The Herschel-SPIRE instrument and its in-flight performance. *A&A*, **518**, L3. doi:10.1051/0004-6361/201014519.

Gruen, D., F. Brimioulle, S. Seitz, C.-H. Lee, J. Young, J. Koppenhoefer, T. Eichner, A. Riffeser, V. Vikram, T. Weidinger, and A. Zenteno (2013). Weak lensing analysis of RXC J2248.7-4431. *MNRAS*, **432**, pp. 1455–1467. doi:10.1093/mnras/stt566.

Gruppioni, C., F. Pozzi, G. Rodighiero, I. Delvecchio, S. Berta, L. Pozzetti, G. Zamorani, P. Andreani, A. Cimatti, O. Ilbert, E. Le Floc'h, D. Lutz, B. Magnelli, L. Marchetti, P. Monaco, R. Nordon, S. Oliver, P. Popesso, L. Riguccini, I. Roseboom, D. J. Rosario, M. Sargent, M. Vaccari, B. Altieri, H. Aussel, A. Bongiovanni, J. Cepa, E. Daddi, H. Domínguez-Sánchez, D. Elbaz, N. Förster Schreiber, R. Genzel, A. Iribarrem, M. Magliocchetti, R. Maiolino, A. Poglitsch, A. Pérez García, M. Sanchez-Portal, E. Sturm, L. Tacconi, I. Valtchanov, A. Amblard, V. Arumugam, M. Bethermin, J. Bock, A. Boselli, V. Buat, D. Burgarella, N. Castro-Rodríguez, A. Cava, P. Chanial, D. L. Clements, A. Conley, A. Cooray, C. D. Dowell, E. Dwek, S. Eales, A. Franceschini, J. Glenn, M. Griffin, E. Hatziminaoglou, E. Ibar, K. Isaak, R. J. Ivison, G. Lagache, L. Levenson, N. Lu, S. Madden, B. Maffei, G. Mainetti, H. T. Nguyen, B. O'Halloran, M. J. Page, P. Panuzzo, A. Papageorgiou, C. P. Pearson, I. Pérez-Fournon, M. Pohlen, D. Rigopoulou, M. Rowan-Robinson, B. Schulz, D. Scott, N. Seymour, D. L. Shupe, A. J. Smith, J. A. Stevens, M. Symeonidis, M. Trichas, K. E. Tugwell, L. Vigroux, L. Wang, G. Wright, C. K. Xu, M. Zemcov, S. Bardelli, M. Carollo, T. Contini, O. Le Févre, S. Lilly, V. Mainieri, A. Renzini, M. Scodeggio, and E. Zucca (2013). The Herschel PEP/HerMES luminosity function - I. Probing the evolution of PACS selected Galaxies to z ≃ 4. *MNRAS*, **432**, pp. 23–52. doi:10.1093/mnras/stt308.

Guo, Y., H. C. Ferguson, E. F. Bell, D. C. Koo, C. J. Conselice, M. Giavalisco, S. Kassin, Y. Lu, R. Lucas, N. Mandelker, D. M. McIntosh, J. R. Primack, S. Ravindranath, G. Barro, D. Ceverino, A. Dekel, S. M. Faber, J. J. Fang, A. M. Koekemoer, K. Noeske, M. Rafelski, and A. Straughn (2015). Clumpy Galaxies in CANDELS. I. The Definition of UV Clumps and the Fraction of Clumpy Galaxies at 0.5 < z < 3. *ApJ*, **800**, 39. doi:10.1088/0004-637X/800/1/39.

Guo, Y., M. Giavalisco, H. C. Ferguson, P. Cassata, and A. M. Koekemoer (2012). Multi-wavelength View of Kiloparsec-scale Clumps in Star-forming Galaxies at z ~ 2. *ApJ*, **757**, 120. doi:10.1088/0004-637X/757/2/120.

Guzzo, L., P. Schuecker, H. Böhringer, C. A. Collins, A. Ortiz-Gil, S. de Grandi, A. C. Edge, D. M. Neumann, S. Schindler, C. Altucci, and P. A. Shaver (2009). The REFLEX galaxy cluster survey. VIII. Spectroscopic observations and optical atlas,. *A&A*, **499**, pp. 357–369. doi:10.1051/0004-6361/200810838.

Hayward, C. C., P. S. Behroozi, R. S. Somerville, J. R. Primack, J. Moreno, and R. H. Wechsler (2013). Spatially unassociated galaxies contribute significantly to the blended submillimetre galaxy population: predictions for follow-up observations of ALMA sources. *MNRAS*, **434**, pp. 2572–2581. doi:10.1093/mnras/stt1202.

Hayward, C. C., L. Lanz, M. L. N. Ashby, G. Fazio, L. Hernquist, J. R. Martínez-Galarza, K. Noeske, H. A. Smith, S. Wuyts, and A. Zezas (2014). The total infrared luminosity may significantly overestimate the star formation rate of quenching and recently quenched galaxies. *MNRAS*, **445**, pp. 1598–1604. doi:10.1093/mnras/stu1843.

Hezaveh, Y. D., D. P. Marrone, and G. P. Holder (2012). Size Bias and Differential Lensing of Strongly Lensed, Dusty Galaxies Identified in Wide-Field Surveys. *ApJ*, **761**, 20. doi:10.1088/0004-637X/761/1/20.

Hildebrand, R. H. (1983). The Determination of Cloud Masses and Dust Characteristics from Submillimetre Thermal Emission. *QJRAS*, **24**, p. 267.

Hodge, J. A., A. Karim, I. Smail, A. M. Swinbank, F. Walter, A. D. Biggs, R. J. Ivison, A. Weiss, D. M. Alexander, F. Bertoldi, W. N. Brandt, S. C. Chapman, K. E. K. Coppin, P. Cox, A. L. R. Danielson, H. Dannerbauer, C. De Breuck, R. Decarli, A. C. Edge, T. R. Greve, K. K. Knudsen, K. M. Menten, H.-W. Rix, E. Schinnerer, J. M. Simpson, J. L. Wardlow, and P. van der Werf (2013). An ALMA Survey of Submillimeter Galaxies in the Extended Chandra Deep Field South: Source Catalog and Multiplicity. *ApJ*, **768**, 91. doi:10.1088/0004-637X/768/1/91.

Houck, J. R., T. L. Roellig, J. van Cleve, W. J. Forrest, T. Herter, C. R. Lawrence, K. Matthews, H. J. Reitsema, B. T. Soifer, D. M. Watson, D. Weedman, M. Huisjen, J. Troeltzsch, D. J. Barry, J. Bernard-Salas, C. E. Blacken, B. R. Brandl, V. Charmandaris, D. Devost, G. E. Gull, P. Hall, C. P. Henderson, S. J. U. Higdon, B. E. Pirger, J. Schoenwald, G. C. Sloan, K. I. Uchida, P. N. Appleton, L. Armus, M. J. Burgdorf, S. B. Fajardo-Acosta, C. J. Grillmair, J. G. Ingalls, P. W. Morris, and H. I. Teplitz (2004). The Infrared Spectrograph (IRS) on the Spitzer Space Telescope. *ApJS*, **154**, pp. 18–24. doi:10.1086/423134.

Hwang, H. S., D. Elbaz, G. Magdis, E. Daddi, M. Symeonidis, B. Altieri, A. Amblard, P. Andreani, V. Arumugam, R. Auld, H. Aussel, T. Babbedge, S. Berta, A. Blain, J. Bock, A. Bongiovanni, A. Boselli, V. Buat, D. Burgarella, N. Castro-Rodríguez, A. Cava, J. Cepa, P. Chanial, E. Chapin, R.-R. Chary, A. Cimatti, D. L. Clements, A. Conley, L. Conversi, A. Cooray, H. Dannerbauer, M. Dickinson, H. Dominguez, C. D. Dowell, J. S. Dunlop, E. Dwek, S. Eales, D. Farrah, N. F. Schreiber, M. Fox, A. Franceschini, W. Gear, R. Genzel, J. Glenn, M. Griffin, C. Gruppioni, M. Halpern, E. Hatziminaoglou, E. Ibar, K. Isaak, R. J. Ivison, W.-S. Jeong, G. Lagache, D. Le Borgne, E. Le Floc'h, H. M. Lee, J. C. Lee, M. G. Lee, L. Levenson, N. Lu, D. Lutz, S. Madden, B. Maffei, B. Magnelli, G. Mainetti, R. Maiolino, L. Marchetti, A. M. J. Mortier, H. T. Nguyen, R. Nordon, B. O'Halloran, K. Okumura, S. J. Oliver, A. Omont, M. J. Page, P. Panuzzo, A. Papageorgiou, C. P. Pearson, I. Pérez-Fournon, A. M. P. García, A. Poglitsch, M. Pohlen, P. Popesso, F. Pozzi, J. I. Rawlings, D. Rigopoulou, L. Riguccini, D. Rizzo, G. Rodighiero, I. G. Roseboom, M. Rowan-Robinson, A. Saintonge, M. S. Portal, P. Santini, M. Sauvage, B. Schulz, D. Scott, N. Seymour, L. Shao, D. L. Shupe, A. J. Smith, J. A. Stevens, E. Sturm, L. Tacconi, M. Trichas, K. E. Tugwell, M. Vaccari, I. Valtchanov, J. D. Vieira, L. Vigroux, L. Wang, R. Ward, G. Wright, C. K. Xu, and M. Zemcov (2010). Evolution of dust temperature of galaxies through cosmic time as seen by Herschel. *MNRAS*, **409**, pp. 75–82. doi:10.1111/j.1365-2966.2010.17645.x.

Ilbert, O., S. Arnouts, H. J. McCracken, M. Bolzonella, E. Bertin, O. Le Fèvre, Y. Mellier, G. Zamorani, R. Pellò, A. Iovino, L. Tresse, V. Le Brun, D. Bottini, B. Garilli, D. Maccagni, J. P. Picat, R. Scaramella, M. Scodeggio, G. Vettolani, A. Zanichelli, C. Adami, S. Bardelli, A. Cappi, S. Charlot, P. Ciliegi, T. Contini, O. Cucciati, S. Foucaud, P. Franzetti, I. Gavignaud, L. Guzzo, B. Marano, C. Marinoni, A. Mazure, B. Meneux, R. Merighi, S. Paltani, A. Pollo, L. Pozzetti, M. Radovich, E. Zucca, M. Bondi, A. Bongiorno, G. Busarello, S. de La Torre, L. Gregorini, F. Lamareille, G. Mathez, P. Merluzzi, V. Ripepi, D. Rizzo, and D. Vergani (2006). Accurate photometric redshifts for the CFHT legacy survey calibrated using the VIMOS VLT deep survey. *A&A*, **457**, pp. 841–856. doi:10.1051/0004-6361:20065138.

Jones, T., R. Ellis, E. Jullo, and J. Richard (2010a). Measurement of a Metallicity Gradient in a z = 2 Galaxy: Implications for Inside-out Assembly Histories. *ApJ*, **725**, pp. L176–L180. doi:10.1088/2041-8205/725/2/L176.

Jones, T., R. S. Ellis, J. Richard, and E. Jullo (2013). The Origin and Evolution of Metallicity Gradients: Probing the Mode of Mass Assembly at z ˜= 2. *ApJ*, **765**, 48. doi:10.1088/0004-637X/765/1/48.

Jones, T. A., A. M. Swinbank, R. S. Ellis, J. Richard, and D. P. Stark (2010b). Resolved spectroscopy of gravitationally lensed galaxies: recovering coherent ve-

locity fields in subluminous z ~ 2-3 galaxies. *MNRAS*, **404**, pp. 1247–1262. doi:10.1111/j.1365-2966.2010.16378.x.

Jullo, E. and J.-P. Kneib (2009). Multiscale cluster lens mass mapping - I. Strong lensing modelling. *MNRAS*, **395**, pp. 1319–1332. doi:10.1111/j.1365-2966.2009.14654.x.

Jullo, E., J.-P. Kneib, M. Limousin, Á. Elíasdóttir, P. J. Marshall, and T. Verdugo (2007). A Bayesian approach to strong lensing modelling of galaxy clusters. *New Journal of Physics*, **9**, p. 447. doi:10.1088/1367-2630/9/12/447.

Juneau, S., M. Dickinson, D. M. Alexander, and S. Salim (2011). A New Diagnostic of Active Galactic Nuclei: Revealing Highly Absorbed Systems at Redshift >0.3. *ApJ*, **736**, 104. doi:10.1088/0004-637X/736/2/104.

Karman, W., K. I. Caputi, C. Grillo, I. Balestra, P. Rosati, E. Vanzella, D. Coe, L. Christensen, A. M. Koekemoer, T. Krühler, M. Lombardi, A. Mercurio, M. Nonino, and A. van der Wel (2015). MUSE integral-field spectroscopy towards the Frontier Fields cluster Abell S1063. I. Data products and redshift identifications. *A&A*, **574**, A11. doi:10.1051/0004-6361/201424962.

Kauffmann, G., T. M. Heckman, C. Tremonti, J. Brinchmann, S. Charlot, S. D. M. White, S. E. Ridgway, J. Brinkmann, M. Fukugita, P. B. Hall, Ž. Ivezić, G. T. Richards, and D. P. Schneider (2003). The host galaxies of active galactic nuclei. *MNRAS*, **346**, pp. 1055–1077. doi:10.1111/j.1365-2966.2003.07154.x.

Kelson, D. D. (2003). Optimal Techniques in Two-dimensional Spectroscopy: Background Subtraction for the 21st Century. *PASP*, **115**, pp. 688–699. doi:10.1086/375502.

Kennicutt, R. C. and N. J. Evans (2012). Star Formation in the Milky Way and Nearby Galaxies. *ARA&A*, **50**, pp. 531–608. doi:10.1146/annurev-astro-081811-125610.

Kennicutt, R. C., Jr. (1998). Star Formation in Galaxies Along the Hubble Sequence. *ARA&A*, **36**, pp. 189–232. doi:10.1146/annurev.astro.36.1.189.

Kewley, L. J. and S. L. Ellison (2008). Metallicity Calibrations and the Mass-Metallicity Relation for Star-forming Galaxies. *ApJ*, **681**, pp. 1183–1204. doi:10.1086/587500.

Kewley, L. J., M. J. Geller, and R. A. Jansen (2004). [O II] as a Star Formation Rate Indicator. *AJ*, **127**, pp. 2002–2030. doi:10.1086/382723.

Kewley, L. J., C. A. Heisler, M. A. Dopita, and S. Lumsden (2001). Optical Classification of Southern Warm Infrared Galaxies. *ApJS*, **132**, pp. 37–71. doi:10.1086/318944.

Kneib, J.-P., R. S. Ellis, I. Smail, W. J. Couch, and R. M. Sharples (1996). Hubble Space Telescope Observations of the Lensing Cluster Abell 2218. *ApJ*, **471**, p. 643. doi:10.1086/177995.

Kruegel, E. and R. Siebenmorgen (1994). Dust in protostellar cores and stellar disks. *A&A*, **288**, pp. 929–941.

Law, D. R., C. C. Steidel, D. K. Erb, J. E. Larkin, M. Pettini, A. E. Shapley, and S. A. Wright (2009). The Kiloparsec-scale Kinematics of High-redshift Star-forming Galaxies. *ApJ*, **697**, pp. 2057–2082. doi:10.1088/0004-637X/697/2/2057.

Le Floc'h, E., C. Papovich, H. Dole, E. F. Bell, G. Lagache, G. H. Rieke, E. Egami, P. G. Pérez-González, A. Alonso-Herrero, M. J. Rieke, M. Blaylock, C. W. Engelbracht, K. D. Gordon, D. C. Hines, K. A. Misselt, J. E. Morrison, and J. Mould (2005). Infrared Luminosity Functions from the Chandra Deep Field-South: The Spitzer View on the History of Dusty Star Formation at $0 <^\sim z <^\sim 1$. *ApJ*, **632**, pp. 169–190. doi:10.1086/432789.

Leroy, A. K., A. Bolatto, K. Gordon, K. Sandstrom, P. Gratier, E. Rosolowsky, C. W. Engelbracht, N. Mizuno, E. Corbelli, Y. Fukui, and A. Kawamura (2011). The CO-to-H_2 Conversion Factor from Infrared Dust Emission across the Local Group. *ApJ*, **737**, 12. doi:10.1088/0004-637X/737/1/12.

Liu, X., A. E. Shapley, A. L. Coil, J. Brinchmann, and C.-P. Ma (2008). Metallicities and Physical Conditions in Star-forming Galaxies at z ˜ 1.0-1.5. *ApJ*, **678**, pp. 758–779. doi:10.1086/529030.

Livermore, R. C., T. Jones, J. Richard, R. G. Bower, R. S. Ellis, A. M. Swinbank, J. R. Rigby, I. Smail, S. Arribas, J. Rodriguez Zaurin, L. Colina, H. Ebeling, and R. A. Crain (2012). Hubble Space Telescope Hα imaging of star-forming galaxies at z $\simeq$ 1-1.5: evolution in the size and luminosity of giant H II regions. *MNRAS*, **427**, pp. 688–702. doi:10.1111/j.1365-2966.2012.21900.x.

Madau, P., L. Pozzetti, and M. Dickinson (1998). The Star Formation History of Field Galaxies. *ApJ*, **498**, pp. 106–116. doi:10.1086/305523.

Magdis, G. E., E. Daddi, M. Sargent, D. Elbaz, R. Gobat, H. Dannerbauer, C. Feruglio, Q. Tan, D. Rigopoulou, V. Charmandaris, M. Dickinson, N. Reddy, and H. Aussel (2012). The Molecular Gas Content of z = 3 Lyman Break Galaxies: Evidence of a Non-evolving Gas Fraction in Main-sequence Galaxies at z > 2. *ApJ*, **758**, L9. doi:10.1088/2041-8205/758/1/L9.

Magnelli, B., D. Elbaz, R. R. Chary, M. Dickinson, D. Le Borgne, D. T. Frayer, and C. N. A. Willmer (2011). Evolution of the dusty infrared luminosity function from z = 0 to z = 2.3 using observations from Spitzer. *A&A*, **528**, A35. doi: 10.1051/0004-6361/200913941.

Maiolino, R., T. Nagao, A. Grazian, F. Cocchia, A. Marconi, F. Mannucci, A. Cimatti, A. Pipino, S. Ballero, F. Calura, C. Chiappini, A. Fontana, G. L. Granato, F. Matteucci, G. Pastorini, L. Pentericci, G. Risaliti, M. Salvati, and L. Silva (2008). AMAZE. I. The evolution of the mass-metallicity relation at z > 3. *A&A*, **488**, pp. 463–479. doi:10.1051/0004-6361:200809678.

Malhotra, S., M. J. Kaufman, D. Hollenbach, G. Helou, R. H. Rubin, J. Brauher, D. Dale, N. Y. Lu, S. Lord, G. Stacey, A. Contursi, D. A. Hunter, and H. Dinerstein (2001). Far-Infrared Spectroscopy of Normal Galaxies: Physical Conditions in the Interstellar Medium. *ApJ*, **561**, pp. 766–786. doi:10.1086/323046.

Maraston, C. (2005). Evolutionary population synthesis: models, analysis of the ingredients and application to high-z galaxies. *MNRAS*, **362**, pp. 799–825. doi: 10.1111/j.1365-2966.2005.09270.x.

Martin, C. L. (2005). Mapping Large-Scale Gaseous Outflows in Ultraluminous Galaxies with Keck II ESI Spectra: Variations in Outflow Velocity with Galactic Mass. *ApJ*, **621**, pp. 227–245. doi:10.1086/427277.

Maughan, B. J., C. Jones, W. Forman, and L. Van Speybroeck (2008). Images, Structural Properties, and Metal Abundances of Galaxy Clusters Observed with Chandra ACIS-I at 0.1<z<1.3. *ApJS*, **174**, pp. 117–135. doi:10.1086/521225.

McLeod, B., D. Fabricant, G. Nystrom, K. McCracken, S. Amato, H. Bergner, W. Brown, M. Burke, I. Chilingarian, M. Conroy, D. Curley, G. Furesz, J. Geary, E. Hertz, J. Holwell, A. Matthews, T. Norton, S. Park, J. Roll, J. Zajac, H. Epps, and P. Martini (2012). MMT and Magellan Infrared Spectrograph. *PASP*, **124**, pp. 1318–1335. doi:10.1086/669044.

Monna, A., S. Seitz, N. Greisel, T. Eichner, N. Drory, M. Postman, A. Zitrin, D. Coe, A. Halkola, S. H. Suyu, C. Grillo, P. Rosati, D. Lemze, I. Balestra, J. Snigula, L. Bradley, K. Umetsu, A. Koekemoer, U. Kuchner, L. Moustakas, M. Bartelmann, N. Benítez, R. Bouwens, T. Broadhurst, M. Donahue, H. Ford, O. Host, L. Infante, Y. Jimenez-Teja, S. Jouvel, D. Kelson, O. Lahav, E. Medezinski, P. Melchior, M. Meneghetti, J. Merten, A. Molino, J. Moustakas, M. Nonino, and W. Zheng (2014). CLASH: z ∼ 6 young galaxy candidate quintuply lensed by the frontier field cluster RXC J2248.7-4431. *MNRAS*, **438**, pp. 1417–1434. doi:10.1093/mnras/stt2284.

Moustakas, J., R. C. Kennicutt, Jr., C. A. Tremonti, D. A. Dale, J.-D. T. Smith, and D. Calzetti (2010). Optical Spectroscopy and Nebular Oxygen Abundances of the Spitzer/SINGS Galaxies. *ApJS*, **190**, 233. doi:10.1088/0067-0049/190/2/233.

Negrello, M., R. Hopwood, G. De Zotti, A. Cooray, A. Verma, J. Bock, D. T. Frayer, M. A. Gurwell, A. Omont, R. Neri, H. Dannerbauer, L. L. Leeuw, E. Barton, J. Cooke, S. Kim, E. da Cunha, G. Rodighiero, P. Cox, D. G. Bonfield, M. J. Jarvis, S. Serjeant, R. J. Ivison, S. Dye, I. Aretxaga, D. H. Hughes, E. Ibar, F. Bertoldi, I. Valtchanov, S. Eales, L. Dunne, S. P. Driver, R. Auld, S. Buttiglione, A. Cava, C. A. Grady, D. L. Clements, A. Dariush, J. Fritz, D. Hill, J. B. Hornbeck, L. Kelvin, G. Lagache, M. Lopez-Caniego, J. Gonzalez-Nuevo, S. Maddox, E. Pascale, M. Pohlen, E. E. Rigby, A. Robotham, C. Simpson, D. J. B. Smith, P. Temi, M. A. Thompson, B. E. Woodgate, D. G. York, J. E. Aguirre, A. Beelen, A. Blain, A. J. Baker, M. Birkinshaw, R. Blundell, C. M. Bradford, D. Burgarella, L. Danese, J. S. Dunlop, S. Fleuren, J. Glenn, A. I. Harris, J. Kamenetzky, R. E. Lupu, R. J. Maddalena, B. F. Madore, P. R. Maloney, H. Matsuhara, M. J. Michałowski, E. J. Murphy, B. J. Naylor, H. Nguyen, C. Popescu, S. Rawlings, D. Rigopoulou, D. Scott, K. S. Scott, M. Seibert, I. Smail, R. J. Tuffs, J. D. Vieira, P. P. van der Werf, and J. Zmuidzinas (2010). The Detection of a Population of Submillimeter-Bright, Strongly Lensed Galaxies. *Science*, **330**, pp. 800–. doi:10.1126/science.1193420.

Noeske, K. G., B. J. Weiner, S. M. Faber, C. Papovich, D. C. Koo, R. S. Somerville, K. Bundy, C. J. Conselice, J. A. Newman, D. Schiminovich, E. Le Floc'h, A. L. Coil, G. H. Rieke, J. M. Lotz, J. R. Primack, P. Barmby, M. C. Cooper, M. Davis, R. S. Ellis, G. G. Fazio, P. Guhathakurta, J. Huang, S. A. Kassin, D. C. Martin, A. C. Phillips, R. M. Rich, T. A. Small, C. N. A. Willmer, and G. Wilson (2007). Star Formation in AEGIS Field Galaxies since z=1.1: The Dominance of Gradually Declining Star Formation, and the Main Sequence of Star-forming Galaxies. *ApJ*, **660**, pp. L43–L46. doi:10.1086/517926.

Osterbrock, D. E. and G. J. Ferland (2006). *Astrophysics of gaseous nebulae and active galactic nuclei*. University Science Books.

Papadopoulos, P. P., H. J. A. Röttgering, P. P. van der Werf, S. Guilloteau, A. Omont, W. J. M. van Breugel, and R. P. J. Tilanus (2000). CO (4-3) and Dust Emission in Two Powerful High-Z Radio Galaxies, and CO Lines at High Redshifts. *ApJ*, **528**, pp. 626–636. doi:10.1086/308215.

Pérez-González, P. G., A. Cava, G. Barro, V. Villar, N. Cardiel, I. Ferreras, J. M. Rodríguez-Espinosa, A. Alonso-Herrero, M. Balcells, J. Cenarro, J. Cepa, S. Charlot, A. Cimatti, C. J. Conselice, E. Daddi, J. Donley, D. Elbaz, N. Espino, J. Gallego, R. Gobat, O. González-Martín, R. Guzmán, A. Hernán-Caballero, C. Muñoz-Tuñón, A. Renzini, J. Rodríguez-Zaurín, L. Tresse, I. Trujillo, and J. Zamorano

(2013). SHARDS: An Optical Spectro-photometric Survey of Distant Galaxies. *ApJ*, **762**, 46. doi:10.1088/0004-637X/762/1/46.

Pérez-González, P. G., G. H. Rieke, E. Egami, A. Alonso-Herrero, H. Dole, C. Papovich, M. Blaylock, J. Jones, M. Rieke, J. Rigby, P. Barmby, G. G. Fazio, J. Huang, and C. Martin (2005). Spitzer View on the Evolution of Star-forming Galaxies from z = 0 to z ~ 3. *ApJ*, **630**, pp. 82–107. doi:10.1086/431894.

Pettini, M. and B. E. J. Pagel (2004). [OIII]/[NII] as an abundance indicator at high redshift. *MNRAS*, **348**, pp. L59–L63. doi:10.1111/j.1365-2966.2004.07591.x.

Piazzo, L. (2013). Subspace Least Square Approach for Drift Removal with Application to Herschel Data. *ArXiv e-prints*.

Pilbratt, G. L., J. R. Riedinger, T. Passvogel, G. Crone, D. Doyle, U. Gageur, A. M. Heras, C. Jewell, L. Metcalfe, S. Ott, and M. Schmidt (2010). Herschel Space Observatory. An ESA facility for far-infrared and submillimetre astronomy. *A&A*, **518**, L1. doi:10.1051/0004-6361/201014759.

Poglitsch, A., C. Waelkens, N. Geis, H. Feuchtgruber, B. Vandenbussche, L. Rodriguez, O. Krause, E. Renotte, C. van Hoof, P. Saraceno, J. Cepa, F. Kerschbaum, P. Agnèse, B. Ali, B. Altieri, P. Andreani, J.-L. Augueres, Z. Balog, L. Barl, O. H. Bauer, N. Belbachir, M. Benedettini, N. Billot, O. Boulade, H. Bischof, J. Blommaert, E. Callut, C. Cara, R. Cerulli, D. Cesarsky, A. Contursi, Y. Creten, W. De Meester, V. Doublier, E. Doumayrou, L. Duband, K. Exter, R. Genzel, J.-M. Gillis, U. Grözinger, T. Henning, J. Herreros, R. Huygen, M. Inguscio, G. Jakob, C. Jamar, C. Jean, J. de Jong, R. Katterloher, C. Kiss, U. Klaas, D. Lemke, D. Lutz, S. Madden, B. Marquet, J. Martignac, A. Mazy, P. Merken, F. Montfort, L. Morbidelli, T. Müller, M. Nielbock, K. Okumura, R. Orfei, R. Ottensamer, S. Pezzuto, P. Popesso, J. Putzeys, S. Regibo, V. Reveret, P. Royer, M. Sauvage, J. Schreiber, J. Stegmaier, D. Schmitt, J. Schubert, E. Sturm, M. Thiel, G. Tofani, R. Vavrek, M. Wetzstein, E. Wieprecht, and E. Wiezorrek (2010). The Photodetector Array Camera and Spectrometer (PACS) on the Herschel Space Observatory. *A&A*, **518**, L2. doi:10.1051/0004-6361/201014535.

Postman, M., D. Coe, N. Benítez, L. Bradley, T. Broadhurst, M. Donahue, H. Ford, O. Graur, G. Graves, S. Jouvel, A. Koekemoer, D. Lemze, E. Medezinski, A. Molino, L. Moustakas, S. Ogaz, A. Riess, S. Rodney, P. Rosati, K. Umetsu, W. Zheng, A. Zitrin, M. Bartelmann, R. Bouwens, N. Czakon, S. Golwala, O. Host, L. Infante, S. Jha, Y. Jimenez-Teja, D. Kelson, O. Lahav, R. Lazkoz, D. Maoz, C. McCully, P. Melchior, M. Meneghetti, J. Merten, J. Moustakas, M. Nonino, B. Patel, E. Regös, J. Sayers, S. Seitz, and A. Van der Wel (2012). The Cluster Lensing and Supernova Survey with Hubble: An Overview. *ApJS*, **199**, 25. doi:10.1088/0067-0049/199/2/25.

Rawle, T. D., A. C. Edge, E. Egami, M. Rex, G. P. Smith, B. Altieri, A. Fiedler, C. P. Haines, M. J. Pereira, P. G. Pérez-González, J. Portouw, I. Valtchanov, G. Walth, P. P. van der Werf, and M. Zemcov (2012). The Relation between Cool Cluster Cores and Herschel-detected Star Formation in Brightest Cluster Galaxies. *ApJ*, **747**, 29. doi:10.1088/0004-637X/747/1/29.

Rawle, T. D., E. Egami, R. S. Bussmann, M. Gurwell, R. J. Ivison, F. Boone, F. Combes, A. L. R. Danielson, M. Rex, J. Richard, I. Smail, A. M. Swinbank, B. Altieri, A. W. Blain, B. Clement, M. Dessauges-Zavadsky, A. C. Edge, G. G. Fazio, T. Jones, J.-P. Kneib, A. Omont, P. G. Pérez-González, D. Schaerer, I. Valtchanov, P. P. van der Werf, G. Walth, M. Zamojski, and M. Zemcov (2014). [C II] and ^{12}CO(1-0) Emission Maps in HLSJ091828.6+514223: A Strongly Lensed Interacting System at z = 5.24. *ApJ*, **783**, 59. doi:10.1088/0004-637X/783/1/59.

Rex, M., T. D. Rawle, E. Egami, P. G. Pérez-González, M. Zemcov, I. Aretxaga, S. M. Chung, D. Fadda, A. H. Gonzalez, D. H. Hughes, C. Horellou, D. Johansson, J.-P. Kneib, J. Richard, B. Altieri, A. K. Fiedler, M. J. Pereira, G. H. Rieke, I. Smail, I. Valtchanov, A. W. Blain, J. J. Bock, F. Boone, C. R. Bridge, B. Clement, F. Combes, C. D. Dowell, M. Dessauges-Zavadsky, O. Ilbert, R. J. Ivison, M. Jauzac, D. Lutz, A. Omont, R. Pelló, G. Rodighiero, D. Schaerer, G. P. Smith, G. L. Walth, P. van der Werf, M. W. Werner, J. E. Austermann, H. Ezawa, R. Kawabe, K. Kohno, T. A. Perera, K. S. Scott, G. W. Wilson, and M. S. Yun (2010). The far-infrared/submillimeter properties of galaxies located behind the Bullet cluster. *A&A*, **518**, L13. doi:10.1051/0004-6361/201014693.

Richard, J., M. Jauzac, M. Limousin, E. Jullo, B. Clément, H. Ebeling, J.-P. Kneib, H. Atek, P. Natarajan, E. Egami, R. Livermore, and R. Bower (2014). Mass and magnification maps for the Hubble Space Telescope Frontier Fields clusters: implications for high-redshift studies. *MNRAS*, **444**, pp. 268–289. doi:10.1093/mnras/stu1395.

Riechers, D. A., C. M. Bradford, D. L. Clements, C. D. Dowell, I. Pérez-Fournon, R. J. Ivison, C. Bridge, A. Conley, H. Fu, J. D. Vieira, J. Wardlow, J. Calanog, A. Cooray, P. Hurley, R. Neri, J. Kamenetzky, J. E. Aguirre, B. Altieri, V. Arumugam, D. J. Benford, M. Béthermin, J. Bock, D. Burgarella, A. Cabrera-Lavers, S. C. Chapman, P. Cox, J. S. Dunlop, L. Earle, D. Farrah, P. Ferrero, A. Franceschini, R. Gavazzi, J. Glenn, E. A. G. Solares, M. A. Gurwell, M. Halpern, E. Hatziminaoglou, A. Hyde, E. Ibar, A. Kovács, M. Krips, R. E. Lupu, P. R. Maloney, P. Martinez-Navajas, H. Matsuhara, E. J. Murphy, B. J. Naylor, H. T. Nguyen, S. J. Oliver, A. Omont, M. J. Page, G. Petitpas, N. Rangwala, I. G. Roseboom, D. Scott, A. J. Smith, J. G. Staguhn, A. Streblyanska, A. P. Thomson, I. Valtchanov, M. Viero, L. Wang, M. Zemcov, and J. Zmuidzinas (2013). A dust-obscured massive maximum-starburst galaxy at a redshift of 6.34. *Nature*, **496**, pp. 329–333. doi:10.1038/nature12050.

Rieke, G. H., A. Alonso-Herrero, B. J. Weiner, P. G. Pérez-González, M. Blaylock, J. L. Donley, and D. Marcillac (2009). Determining Star Formation Rates for Infrared Galaxies. *ApJ*, **692**, pp. 556–573. doi:10.1088/0004-637X/692/1/556.

Rieke, G. H., E. T. Young, C. W. Engelbracht, D. M. Kelly, F. J. Low, E. E. Haller, J. W. Beeman, K. D. Gordon, J. A. Stansberry, K. A. Misselt, J. Cadien, J. E. Morrison, G. Rivlis, W. B. Latter, A. Noriega-Crespo, D. L. Padgett, K. R. Stapelfeldt, D. C. Hines, E. Egami, J. Muzerolle, A. Alonso-Herrero, M. Blaylock, H. Dole, J. L. Hinz, E. Le Floc'h, C. Papovich, P. G. Pérez-González, P. S. Smith, K. Y. L. Su, L. Bennett, D. T. Frayer, D. Henderson, N. Lu, F. Masci, M. Pesenson, L. Rebull, J. Rho, J. Keene, S. Stolovy, S. Wachter, W. Wheaton, M. W. Werner, and P. L. Richards (2004). The Multiband Imaging Photometer for Spitzer (MIPS). *ApJS*, **154**, pp. 25–29. doi:10.1086/422717.

Rigby, J. R. and G. H. Rieke (2004). Missing Massive Stars in Starbursts: Stellar Temperature Diagnostics and the Initial Mass Function. *ApJ*, **606**, pp. 237–257. doi:10.1086/382776.

Rodighiero, G., A. Cimatti, C. Gruppioni, P. Popesso, P. Andreani, B. Altieri, H. Aussel, S. Berta, A. Bongiovanni, D. Brisbin, A. Cava, J. Cepa, E. Daddi, H. Dominguez-Sanchez, D. Elbaz, A. Fontana, N. Förster Schreiber, A. Franceschini, R. Genzel, A. Grazian, D. Lutz, G. Magdis, M. Magliocchetti, B. Magnelli, R. Maiolino, C. Mancini, R. Nordon, A. M. Perez Garcia, A. Poglitsch, P. Santini, M. Sanchez-Portal, F. Pozzi, L. Riguccini, A. Saintonge, L. Shao, E. Sturm, L. Tacconi, I. Valtchanov, M. Wetzstein, and E. Wieprecht (2010a). The first Herschel view of the mass-SFR link in high-z galaxies. *A&A*, **518**, L25. doi: 10.1051/0004-6361/201014624.

Rodighiero, G., E. Daddi, I. Baronchelli, A. Cimatti, A. Renzini, H. Aussel, P. Popesso, D. Lutz, P. Andreani, S. Berta, A. Cava, D. Elbaz, A. Feltre, A. Fontana, N. M. Förster Schreiber, A. Franceschini, R. Genzel, A. Grazian, C. Gruppioni, O. Ilbert, E. Le Floch, G. Magdis, M. Magliocchetti, B. Magnelli, R. Maiolino, H. McCracken, R. Nordon, A. Poglitsch, P. Santini, F. Pozzi, L. Riguccini, L. J. Tacconi, S. Wuyts, and G. Zamorani (2011). The Lesser Role of Starbursts in Star Formation at z = 2. *ApJ*, **739**, L40. doi:10.1088/2041-8205/739/2/L40.

Rodighiero, G., M. Vaccari, A. Franceschini, L. Tresse, O. Le Fevre, V. Le Brun, C. Mancini, I. Matute, A. Cimatti, L. Marchetti, O. Ilbert, S. Arnouts, M. Bolzonella, E. Zucca, S. Bardelli, C. J. Lonsdale, D. Shupe, J. Surace, M. Rowan-Robinson, B. Garilli, G. Zamorani, L. Pozzetti, M. Bondi, S. de la Torre, D. Vergani, P. Santini, A. Grazian, and A. Fontana (2010b). Mid- and far-infrared luminosity functions and galaxy evolution from multiwavelength Spitzer observations up to z ~ 2.5. *A&A*, **515**, A8. doi:10.1051/0004-6361/200912058.

Rujopakarn, W., G. H. Rieke, C. J. Papovich, B. J. Weiner, J. R. Rigby, M. Rex, F. Bian, O. P. Kuhn, and D. Thompson (2012). Large Binocular Telescope and Spitzer Spectroscopy of Star-forming Galaxies at $1 < z < 3$: Extinction and Star Formation Rate Indicators. *ApJ*, **755**, 168. doi:10.1088/0004-637X/755/2/168.

Rupke, D. S., S. Veilleux, and D. B. Sanders (2002). Keck Absorption-Line Spectroscopy of Galactic Winds in Ultraluminous Infrared Galaxies. *ApJ*, **570**, pp. 588–609. doi:10.1086/339789.

Rupke, D. S., S. Veilleux, and D. B. Sanders (2005). Outflows in Infrared-Luminous Starbursts at $z < 0.5$. II. Analysis and Discussion. *ApJS*, **160**, pp. 115–148. doi:10.1086/432889.

Sandstrom, K. M., A. K. Leroy, F. Walter, A. D. Bolatto, K. V. Croxall, B. T. Draine, C. D. Wilson, M. Wolfire, D. Calzetti, R. C. Kennicutt, G. Aniano, J. Donovan Meyer, A. Usero, F. Bigiel, E. Brinks, W. J. G. de Blok, A. Crocker, D. Dale, C. W. Engelbracht, M. Galametz, B. Groves, L. K. Hunt, J. Koda, K. Kreckel, H. Linz, S. Meidt, E. Pellegrini, H.-W. Rix, H. Roussel, E. Schinnerer, A. Schruba, K.-F. Schuster, R. Skibba, T. van der Laan, P. Appleton, L. Armus, B. Brandl, K. Gordon, J. Hinz, O. Krause, E. Montiel, M. Sauvage, A. Schmiedeke, J. D. T. Smith, and L. Vigroux (2013). The CO-to-H_2 Conversion Factor and Dust-to-gas Ratio on Kiloparsec Scales in Nearby Galaxies. *ApJ*, **777**, 5. doi:10.1088/0004-637X/777/1/5.

Sargsyan, L., V. Lebouteiller, D. Weedman, H. Spoon, J. Bernard-Salas, D. Engels, G. Stacey, J. Houck, D. Barry, J. Miles, and A. Samsonyan (2012). [C II] 158 μm Luminosities and Star Formation Rate in Dusty Starbursts and Active Galactic Nuclei. *ApJ*, **755**, 171. doi:10.1088/0004-637X/755/2/171.

Shapley, A. E., N. A. Reddy, M. Kriek, W. R. Freeman, R. L. Sanders, B. Siana, A. L. Coil, B. Mobasher, I. Shivaei, S. H. Price, and L. de Groot (2015). The MOSDEF Survey: Excitation Properties of $z \sim 2.3$ Star-forming Galaxies. *ApJ*, **801**, 88. doi:10.1088/0004-637X/801/2/88.

Shapley, A. E., C. C. Steidel, D. K. Erb, N. A. Reddy, K. L. Adelberger, M. Pettini, P. Barmby, and J. Huang (2005). Ultraviolet to Mid-Infrared Observations of Star-forming Galaxies at z~2: Stellar Masses and Stellar Populations. *ApJ*, **626**, pp. 698–722. doi:10.1086/429990.

Smith, J. D. T., B. T. Draine, D. A. Dale, J. Moustakas, R. C. Kennicutt, Jr., G. Helou, L. Armus, H. Roussel, K. Sheth, G. J. Bendo, B. A. Buckalew, D. Calzetti, C. W. Engelbracht, K. D. Gordon, D. J. Hollenbach, A. Li, S. Malhotra, E. J. Murphy, and F. Walter (2007). The Mid-Infrared Spectrum of Star-forming Galaxies: Global Properties of Polycyclic Aromatic Hydrocarbon Emission. *ApJ*, **656**, pp. 770–791. doi:10.1086/510549.

Sofue, Y., Y. Tutui, M. Honma, A. Tomita, T. Takamiya, J. Koda, and Y. Takeda (1999). Central Rotation Curves of Spiral Galaxies. *ApJ*, **523**, pp. 136–146. doi: 10.1086/307731.

Solomon, P. M. and P. A. Vanden Bout (2005). Molecular Gas at High Redshift. *ARA&A*, **43**, pp. 677–725. doi:10.1146/annurev.astro.43.051804.102221.

Spilker, J. S., M. Aravena, D. P. Marrone, M. Bethermin, M. S. Bothwell, J. E. Carlstrom, S. C. Chapman, J. D. Collier, C. de Breuck, C. D. Fassnacht, T. Galvin, A. H. Gonzalez, J. Gonzalez-Lopez, K. Grieve, Y. Hezaveh, J. Ma, M. Malkan, A. O'Brien, K. M. Rotermund, M. Strandet, J. D. Vieira, A. Weiss, and G. F. Wong (2015). Sub-kiloparsec Imaging of Cool Molecular Gas in Two Strongly Lensed Dusty, Star-Forming Galaxies. *ArXiv e-prints*.

Spilker, J. S., D. P. Marrone, J. E. Aguirre, M. Aravena, M. L. N. Ashby, M. Béthermin, C. M. Bradford, M. S. Bothwell, M. Brodwin, J. E. Carlstrom, S. C. Chapman, T. M. Crawford, C. de Breuck, C. D. Fassnacht, A. H. Gonzalez, T. R. Greve, B. Gullberg, Y. Hezaveh, W. L. Holzapfel, K. Husband, J. Ma, M. Malkan, E. J. Murphy, C. L. Reichardt, K. M. Rotermund, B. Stalder, A. A. Stark, M. Strandet, J. D. Vieira, A. Weiß, and N. Welikala (2014). The Rest-frame Submillimeter Spectrum of High-redshift, Dusty, Star-forming Galaxies. *ApJ*, **785**, 149. doi:10.1088/0004-637X/785/2/149.

Stacey, G. J., S. Hailey-Dunsheath, C. Ferkinhoff, T. Nikola, S. C. Parshley, D. J. Benford, J. G. Staguhn, and N. Fiolet (2010). A 158 μm [C II] Line Survey of Galaxies at z ˜ 1-2: An Indicator of Star Formation in the Early Universe. *ApJ*, **724**, pp. 957–974. doi:10.1088/0004-637X/724/2/957.

Stark, D. P., G. Walth, S. Charlot, B. Clément, A. Feltre, J. Gutkin, J. Richard, R. Mainali, B. Robertson, B. Siana, M. Tang, and M. Schenker (2015). Spectroscopic detection of C IV λ1548 in a galaxy at z = 7.045: implications for the ionizing spectra of reionization-era galaxies. *MNRAS*, **454**, pp. 1393–1403. doi: 10.1093/mnras/stv1907.

Steidel, C. C., G. C. Rudie, A. L. Strom, M. Pettini, N. A. Reddy, A. E. Shapley, R. F. Trainor, D. K. Erb, M. L. Turner, N. P. Konidaris, K. R. Kulas, G. Mace, K. Matthews, and I. S. McLean (2014). Strong Nebular Line Ratios in the Spectra of z ˜ 2-3 Star Forming Galaxies: First Results from KBSS-MOSFIRE. *ApJ*, **795**, 165. doi:10.1088/0004-637X/795/2/165.

Swinbank, A. M., A. Karim, I. Smail, J. Hodge, F. Walter, F. Bertoldi, A. D. Biggs, C. de Breuck, S. C. Chapman, K. E. K. Coppin, P. Cox, A. L. R. Danielson, H. Dannerbauer, R. J. Ivison, T. R. Greve, K. K. Knudsen, K. M. Menten, J. M. Simpson, E. Schinnerer, J. L. Wardlow, A. Weiß, and P. van der Werf (2012).

An ALMA survey of submillimetre galaxies in the Extended Chandra Deep Field-South: detection of [C II] at z = 4.4. *MNRAS*, **427**, pp. 1066–1074. doi:10.1111/j.1365-2966.2012.22048.x.

Swinbank, A. M., I. Smail, S. C. Chapman, A. W. Blain, R. J. Ivison, and W. C. Keel (2004). The Rest-Frame Optical Spectra of SCUBA Galaxies. *ApJ*, **617**, pp. 64–80. doi:10.1086/425171.

Swinbank, A. M., I. Smail, S. Longmore, A. I. Harris, A. J. Baker, C. De Breuck, J. Richard, A. C. Edge, R. J. Ivison, R. Blundell, K. E. K. Coppin, P. Cox, M. Gurwell, L. J. Hainline, M. Krips, A. Lundgren, R. Neri, B. Siana, G. Siringo, D. P. Stark, D. Wilner, and J. D. Younger (2010). Intense star formation within resolved compact regions in a galaxy at z = 2.3. *Nature*, **464**, pp. 733–736. doi:10.1038/nature08880.

Tacconi, L. J., R. Genzel, I. Smail, R. Neri, S. C. Chapman, R. J. Ivison, A. Blain, P. Cox, A. Omont, F. Bertoldi, T. Greve, N. M. Förster Schreiber, S. Genel, D. Lutz, A. M. Swinbank, A. E. Shapley, D. K. Erb, A. Cimatti, E. Daddi, and A. J. Baker (2008). Submillimeter Galaxies at z ˜ 2: Evidence for Major Mergers and Constraints on Lifetimes, IMF, and CO-H_2 Conversion Factor. *ApJ*, **680**, pp. 246–262. doi:10.1086/587168.

Tacconi, L. J., R. Neri, R. Genzel, F. Combes, A. Bolatto, M. C. Cooper, S. Wuyts, F. Bournaud, A. Burkert, J. Comerford, P. Cox, M. Davis, N. M. Förster Schreiber, S. García-Burillo, J. Gracia-Carpio, D. Lutz, T. Naab, S. Newman, A. Omont, A. Saintonge, K. Shapiro Griffin, A. Shapley, A. Sternberg, and B. Weiner (2013). Phibss: Molecular Gas Content and Scaling Relations in z ˜ 1-3 Massive, Main-sequence Star-forming Galaxies. *ApJ*, **768**, 74. doi:10.1088/0004-637X/768/1/74.

Thornley, M. D., N. M. F. Schreiber, D. Lutz, R. Genzel, H. W. W. Spoon, D. Kunze, and A. Sternberg (2000). Massive Star Formation and Evolution in Starburst Galaxies: Mid-infrared Spectroscopy with the ISO Short Wavelength Spectrometer. *ApJ*, **539**, pp. 641–657. doi:10.1086/309261.

Valtchanov, I., J. Virdee, R. J. Ivison, B. Swinyard, P. van der Werf, D. Rigopoulou, E. da Cunha, R. Lupu, D. J. Benford, D. Riechers, I. Smail, M. Jarvis, C. Pearson, H. Gomez, R. Hopwood, B. Altieri, M. Birkinshaw, D. Coia, L. Conversi, A. Cooray, G. de Zotti, L. Dunne, D. Frayer, L. Leeuw, A. Marston, M. Negrello, M. S. Portal, D. Scott, M. A. Thompson, M. Vaccari, M. Baes, D. Clements, M. J. Michałowski, H. Dannerbauer, S. Serjeant, R. Auld, S. Buttiglione, A. Cava, A. Dariush, S. Dye, S. Eales, J. Fritz, E. Ibar, S. Maddox, E. Pascale, M. Pohlen, E. Rigby, G. Rodighiero, D. J. B. Smith, P. Temi, J. Carpenter, A. Bolatto, M. Gurwell, and J. D. Vieira (2011). Physical conditions of the interstellar medium

of high-redshift, strongly lensed submillimetre galaxies from the Herschel-ATLAS. *MNRAS*, **415**, pp. 3473–3484. doi:10.1111/j.1365-2966.2011.18959.x.

Venemans, B. P., R. G. McMahon, F. Walter, R. Decarli, P. Cox, R. Neri, P. Hewett, D. J. Mortlock, C. Simpson, and S. J. Warren (2012). Detection of Atomic Carbon [C II] 158 μm and Dust Emission from a z = 7.1 Quasar Host Galaxy. *ApJ*, **751**, L25. doi:10.1088/2041-8205/751/2/L25.

Wagg, J., T. Wiklind, C. L. Carilli, D. Espada, A. Peck, D. Riechers, F. Walter, A. Wootten, M. Aravena, D. Barkats, J. R. Cortes, R. Hills, J. Hodge, C. M. V. Impellizzeri, D. Iono, A. Leroy, S. Martín, M. G. Rawlings, R. Maiolino, R. G. McMahon, K. S. Scott, E. Villard, and C. Vlahakis (2012). [C II] Line Emission in Massive Star-forming Galaxies at z = 4.7. *ApJ*, **752**, L30. doi:10.1088/2041-8205/752/2/L30.

Wardlow, J. L., A. Cooray, F. De Bernardis, A. Amblard, V. Arumugam, H. Aussel, A. J. Baker, M. Béthermin, R. Blundell, J. Bock, A. Boselli, C. Bridge, V. Buat, D. Burgarella, R. S. Bussmann, A. Cabrera-Lavers, J. Calanog, J. M. Carpenter, C. M. Casey, N. Castro-Rodríguez, A. Cava, P. Chanial, E. Chapin, S. C. Chapman, D. L. Clements, A. Conley, P. Cox, C. D. Dowell, S. Dye, S. Eales, D. Farrah, P. Ferrero, A. Franceschini, D. T. Frayer, C. Frazer, H. Fu, R. Gavazzi, J. Glenn, E. A. González Solares, M. Griffin, M. A. Gurwell, A. I. Harris, E. Hatziminaoglou, R. Hopwood, A. Hyde, E. Ibar, R. J. Ivison, S. Kim, G. Lagache, L. Levenson, L. Marchetti, G. Marsden, P. Martinez-Navajas, M. Negrello, R. Neri, H. T. Nguyen, B. O'Halloran, S. J. Oliver, A. Omont, M. J. Page, P. Panuzzo, A. Papageorgiou, C. P. Pearson, I. Pérez-Fournon, M. Pohlen, D. Riechers, D. Rigopoulou, I. G. Roseboom, M. Rowan-Robinson, B. Schulz, D. Scott, N. Scoville, N. Seymour, D. L. Shupe, A. J. Smith, A. Streblyanska, A. Strom, M. Symeonidis, M. Trichas, M. Vaccari, J. D. Vieira, M. Viero, L. Wang, C. K. Xu, L. Yan, and M. Zemcov (2013). HerMES: Candidate Gravitationally Lensed Galaxies and Lensing Statistics at Submillimeter Wavelengths. *ApJ*, **762**, 59. doi:10.1088/0004-637X/762/1/59.

Watson, D., L. Christensen, K. K. Knudsen, J. Richard, A. Gallazzi, and M. J. Michałowski (2015). A dusty, normal galaxy in the epoch of reionization. *Nature*, **519**, pp. 327–330. doi:10.1038/nature14164.

Weiß, A., C. De Breuck, D. P. Marrone, J. D. Vieira, J. E. Aguirre, K. A. Aird, M. Aravena, M. L. N. Ashby, M. Bayliss, B. A. Benson, M. Béthermin, A. D. Biggs, L. E. Bleem, J. J. Bock, M. Bothwell, C. M. Bradford, M. Brodwin, J. E. Carlstrom, C. L. Chang, S. C. Chapman, T. M. Crawford, A. T. Crites, T. de Haan, M. A. Dobbs, T. P. Downes, C. D. Fassnacht, E. M. George, M. D. Gladders, A. H. Gonzalez, T. R. Greve, N. W. Halverson, Y. D. Hezaveh, F. W. High, G. P. Holder, W. L. Holzapfel, S. Hoover, J. D. Hrubes, K. Husband, R. Keisler, A. T. Lee,

E. M. Leitch, M. Lueker, D. Luong-Van, M. Malkan, V. McIntyre, J. J. McMahon, J. Mehl, K. M. Menten, S. S. Meyer, E. J. Murphy, S. Padin, T. Plagge, C. L. Reichardt, A. Rest, M. Rosenman, J. Ruel, J. E. Ruhl, K. K. Schaffer, E. Shirokoff, J. S. Spilker, B. Stalder, Z. Staniszewski, A. A. Stark, K. Story, K. Vanderlinde, N. Welikala, and R. Williamson (2013). ALMA Redshifts of Millimeter-selected Galaxies from the SPT Survey: The Redshift Distribution of Dusty Star-forming Galaxies. *ApJ*, **767**, 88. doi:10.1088/0004-637X/767/1/88.

Werner, M. W., T. L. Roellig, F. J. Low, G. H. Rieke, M. Rieke, W. F. Hoffmann, E. Young, J. R. Houck, B. Brandl, G. G. Fazio, J. L. Hora, R. D. Gehrz, G. Helou, B. T. Soifer, J. Stauffer, J. Keene, P. Eisenhardt, D. Gallagher, T. N. Gautier, W. Irace, C. R. Lawrence, L. Simmons, J. E. Van Cleve, M. Jura, E. L. Wright, and D. P. Cruikshank (2004). The Spitzer Space Telescope Mission. *ApJS*, **154**, pp. 1–9. doi:10.1086/422992.

Whitaker, K. E., P. G. van Dokkum, G. Brammer, and M. Franx (2012). The Star Formation Mass Sequence Out to z = 2.5. *ApJ*, **754**, L29. doi:10.1088/2041-8205/754/2/L29.

Williamson, R., B. A. Benson, F. W. High, K. Vanderlinde, P. A. R. Ade, K. A. Aird, K. Andersson, R. Armstrong, M. L. N. Ashby, M. Bautz, G. Bazin, E. Bertin, L. E. Bleem, M. Bonamente, M. Brodwin, J. E. Carlstrom, C. L. Chang, S. C. Chapman, A. Clocchiatti, T. M. Crawford, A. T. Crites, T. de Haan, S. Desai, M. A. Dobbs, J. P. Dudley, G. G. Fazio, R. J. Foley, W. R. Forman, G. Garmire, E. M. George, M. D. Gladders, A. H. Gonzalez, N. W. Halverson, G. P. Holder, W. L. Holzapfel, S. Hoover, J. D. Hrubes, C. Jones, M. Joy, R. Keisler, L. Knox, A. T. Lee, E. M. Leitch, M. Lueker, D. Luong-Van, D. P. Marrone, J. J. McMahon, J. Mehl, S. S. Meyer, J. J. Mohr, T. E. Montroy, S. S. Murray, S. Padin, T. Plagge, C. Pryke, C. L. Reichardt, A. Rest, J. Ruel, J. E. Ruhl, B. R. Saliwanchik, A. Saro, K. K. Schaffer, L. Shaw, E. Shirokoff, J. Song, H. G. Spieler, B. Stalder, S. A. Stanford, Z. Staniszewski, A. A. Stark, K. Story, C. W. Stubbs, J. D. Vieira, A. Vikhlinin, and A. Zenteno (2011). A Sunyaev-Zel'dovich-selected Sample of the Most Massive Galaxy Clusters in the 2500 deg^2 South Pole Telescope Survey. *ApJ*, **738**, 139. doi:10.1088/0004-637X/738/2/139.

Wisnioski, E., K. Glazebrook, C. Blake, G. B. Poole, A. W. Green, T. Wyder, and C. Martin (2012). Scaling relations of star-forming regions: from kpc-sized clumps to H II regions. *MNRAS*, **422**, pp. 3339–3355. doi:10.1111/j.1365-2966.2012.20850.x.

Wisnioski, E., K. Glazebrook, C. Blake, and A. M. Swinbank (2013). Dust properties of clumpy disc galaxies at z ∼ 1.3 with Herschel-SPIRE. *MNRAS*, **436**, pp. 266–274. doi:10.1093/mnras/stt1570.

Wong, K. C., S. M. Ammons, C. R. Keeton, and A. I. Zabludoff (2012). Optimal Mass Configurations for Lensing High-redshift Galaxies. *ApJ*, **752**, 104. doi: 10.1088/0004-637X/752/2/104.

Wright, S. A., J. E. Larkin, J. R. Graham, and C.-P. Ma (2010). The Presence of Weak Active Galactic Nuclei in High Redshift Star-forming Galaxies. *ApJ*, **711**, pp. 1291–1296. doi:10.1088/0004-637X/711/2/1291.

Wuyts, E., J. R. Rigby, M. D. Gladders, and K. Sharon (2014). A Magnified View of the Kinematics and Morphology of RCSGA 032727-132609: Zooming in on a Merger at z = 1.7. *ApJ*, **781**, 61. doi:10.1088/0004-637X/781/2/61.